LAWRENCE
LIVERMORE
NATIONAL
LABORATORY

LLNL-TH-692443

Molecular Dynamics Modeling of PPTA Crystals in Aramid Fibers

B. S. Mercer

May 19, 2016

Disclaimer

This work performed under the auspices of the U.S. Department of Energy by Lawrence Livermore National Laboratory under Contract DE-AC52-07NA27344.

Molecular Dynamics Modeling of PPTA Crystals in Aramid Fibers

by

Brian Scott Mercer

A dissertation submitted in partial satisfaction of the

requirements for the degree of

Doctor of Philosophy

in

Engineering - Mechanical Engineering

in the

Graduate Division

of the

University of California, Berkeley

Committee in charge:

Professor Panayiotis Papadopoulos, Chair
Dr. Edward Zywicz
Professor Daryl Chrzan
Professor Tarek Zohdi

Spring 2016

Molecular Dynamics Modeling of PPTA Crystals in Aramid Fibers

Abstract

Molecular Dynamics Modeling of PPTA Crystals in Aramid Fibers

by

Brian Scott Mercer

Doctor of Philosophy in Engineering - Mechanical Engineering

University of California, Berkeley

Professor Panayiotis Papadopoulos, Chair

In this work, molecular dynamics modeling is used to study the mechanical properties of PPTA crystallites, which are the fundamental microstructural building blocks of polymer aramid fibers such as Kevlar. Particular focus is given to constant strain rate axial loading simulations of PPTA crystallites, which is motivated by the rate-dependent mechanical properties observed in some experiments with aramid fibers. In order to accommodate the covalent bond rupture that occurs in loading a crystallite to failure, the reactive bond order force field ReaxFF is employed to conduct the simulations.

Two major topics are addressed: The first is the general behavior of PPTA crystallites under strain rate loading. Constant strain rate loading simulations of crystalline PPTA reveal that the crystal failure strain increases with increasing strain rate, while the modulus is not affected by the strain rate. Increasing temperature lowers both the modulus and the failure strain. The simulations also identify the C–N bond connecting the aromatic rings as weakest primary bond along the backbone of the PPTA chain. The effect of chain-end defects on PPTA micromechanics is explored, and it is found that the presence of a chain-end defect transfers load to the adjacent chains in the hydrogen-bonded sheet in which the defect resides, but does not influence the behavior of any other chains in the crystal. Chain-end defects are found to lower the strength of the crystal when clustered together, inducing bond failure via stress concentrations arising from the load transfer to bonds in adjacent chains near the defect site. The second topic addressed is the nature of primary and secondary bond failure in crystalline PPTA. Failure of both types of bonds is found to be stochastic in nature and driven by thermal fluctuations of the bonds within the crystal. A model is proposed which uses reliability theory to model bonds under constant strain rate loading as components with time-dependent failure rate functions. The model is shown to work well for predicting the onset of primary backbone bond failure, as well as the onset of secondary bond failure via chain slippage for the case of isolated non-interacting chain-end defects.

To all my family and friends whose support made this dissertation possible.

Contents

Contents ii

List of Figures iv

List of Tables viii

1 Introduction 1

2 PPTA fiber morphology and mechanical properties 5
2.1 PPTA fiber morphology . . . 5
2.2 PPTA fiber properties . . . 8

3 Molecular dynamics modeling of PPTA crystals 12
3.1 Selection and description of interatomic potentials . . . 13
3.1.1 The PCFF potential . . . 13
3.1.2 The ReaxFF potential . . . 15
3.2 Molecular Dynamics Theory and Algorithmic Implementation . . . 16
3.2.1 Integration of the equations of motion . . . 17
3.2.2 Periodic boundary conditions . . . 17
3.2.3 Controlling temperature and pressure . . . 18
3.2.4 Accounting for atomic charge . . . 20
3.3 Validation of PCFF and ReaxFF potentials for PPTA modeling . . . 21
3.3.1 Simulation set-up in LAMMPS . . . 22
3.3.2 Unit cell geometry . . . 23
3.3.3 Calculation of elastic moduli . . . 26
3.3.4 Molecular geometry change with axial stretch . . . 29

4 Constant strain rate loading simulations of crystalline PPTA 32
4.1 Mechanical response of perfectly crystalline PPTA under constant strain rate loading . . . 32
4.1.1 Discussion of simulation results . . . 39
4.2 The influence of structural defects on the mechanical response of PPTA crystals 42
4.2.1 The zone of influence of chain-end defects . . . 43

4.2.2 Influence of defects on strain rate loading response 49
4.2.3 Influence of defects on axial stiffness 57

5 Analysis of failure in PPTA crystals **62**
5.1 Reliability theory 62
5.1.1 The special case of constant hazard rate 64
5.2 Primary bond failure in crystalline PPTA 65
5.2.1 Observations of primary bond failure behavior in MD simulations . . 65
5.2.2 Primary bond failure rate at constant strain and temperature conditions 67
5.2.3 A model for primary bond failure under constant strain rate loading . 74
5.3 Secondary bond failure in crystalline PPTA 79
5.3.1 Observations of secondary bond failure behavior in MD simulations . 79
5.3.2 Modeling secondary bond failure near isolated chain-end defects under strain rate loading 86

6 Conclusion **93**

Bibliography **95**

A Data files and force field parameters **102**
A.1 PCFF-parameterized data file for a single unit cell of crystalline PPTA . . . 102
A.2 ReaxFF parameter file 112

B LAMMPS input files **117**
B.1 LAMMPS input file for constant strain rate molecular dynamics 117

List of Figures

2.1 Diagram of a single PPTA monomer. 6
2.2 Crystalline unit cell for PPTA [52]. The x, y, and z Cartesian axes correspond to the a, b, and c crystalline unit cell dimensions, respectively. The z axis corresponds to the fiber axis. 7
2.3 Radial system of pleated lamella postulated in [15, 16]. 8
2.4 The model by Panar et al. [56] shows the periodic defect planes with long polymer chains extending through them, and also the tie points that were hypothesized to assist in holding parallel fibrils together. 9
2.5 Li et al. [40] highlight the skin-core difference, crystallite distribution, and repeating defect planes along the fiber axis, as well as the radial arrangement of hydrogen-bonded sheets. 10
2.6 The model proposed by Morgan et al. [48] is similar to the Li et al. [40] model, and focuses on the skin-core structural difference and the "Shish kebab" nature of the stacked lammelar structure. 11

3.1 An illustration of periodic boundary conditions and interaction cutoff radius r_c in an MD simulation. 18
3.2 Diagram of a single PPTA monomer. 23
3.3 Breakdown of a monomer into four major components, two aromatic rings and the three bonds consisting of the links between rings. C, H, O and N atoms are colored gray, white, red, and blue, respectively. 24
3.4 Normal and shear strain deformations applied to the unit cell to compute elastic moduli. Calculations of strains ϵ_{xx} and $2\epsilon_{xy}$ are shown as an example. 27
3.5 Bond length versus monomer strain 30
3.6 Bond strain versus monomer strain 30
3.7 Angle orientation as denoted by direction cosine θ_z 31
3.8 Strain in the two links and two rings consisting a single monomer, versus monomer strain. Component labels follow those in Figure 3.3. 31

4.1 Stress-strain curve and bond break history for the 4×4×8 unit cell system at $\dot{\epsilon}_{zz} = 1.0 \times 10^9$ s^{-1}. 33

4.2 Diagram of a hydrogen bond in PPTA, highlighting the bond length d_{hb} and bond angle θ_{hb}. 34
4.3 The stress-strain and bond break history plot from Figure 4.1 for the 4×4×8 unit cell system is reproduced, but bond breaks are organized by hydrogen-bonded sheet. There is a clear correlation between the drops in stress in the post-failure regime of the stress-strain curve and the rupture of each individual sheet. 35
4.4 Simulation at strain rate $\dot{\epsilon} = 1.0 \times 10^9$ s^{-1} for five different equilibrated starting points of the 4×4×8 unit cell system. The difference in failure strain between runs highlights the stochastic nature of the failure response. 36
4.5 Stress-strain curves for the 4×4×8 unit cell system at five different strain rates. Five different equilibrated starting points are used for each rate. 37
4.6 Stress-strain response and bond break history for two different strain rates of the 4×4×8 unit cell system. 37
4.7 Failure strain versus strain rate for the 4×4×8 unit cell system. 38
4.8 Stress-strain curves for the 4×4×8 and 8×8×64 unit cell systems, highlighting the lower failure strain for larger systems. 39
4.9 Stress-strain curves for the 4×4×8 perfect crystal model at a strain rate of $\dot{\epsilon} = 1.0 \times 10^9$ s^{-1} and temperatures of 300 K, 400 K, and 500 K. 40
4.10 Failure strain versus strain rate for the 4×4×8 perfect crystal model at temperatures of 300 K, 400 K, and 500 K. 41
4.11 A chain-end defect is introduced by removing the bonds linking two aromatic rings, and capping the rings with hydrogen atoms. 43
4.12 Response of links in PPTA chains for a system containing a single chain-end defect at monomer position 0 45
4.13 Response of hydrogen bonds in PPTA chains for a system containing a single chain-end defect located at monomer position 0. 45
4.14 Visualization of the molecular deformation near the site of the chain-end defect. Note the increased stretch in hydrogen bonds near the defect, which occurs due to relaxation (shortening) of the broken chain relative to the adjacent chains. . . 46
4.15 Response of links in PPTA chains for a system two chain-end defects at monomer position +4 and −4. 47
4.16 Visualization of introducing three chain-end defects in a row, a total of three eliminated links along the center chain backbone. 48
4.17 Response of links in PPTA chains for a system with three missing linkages in a row, as illustrated in Figure 4.16. 48
4.18 Response of links in PPTA chains for a system with a small crack, as illustrated in Figure 4.19a. 49
4.19 Visualization of the introduction of three defects at the same location in three adjacent chains, mimicking a crack. Figure (a) shows the crack at equilibrium (0% strain), and Figure (b) highlights the hydrogen bond failure that occurs for chains near the crack tip when the crystal is stretched to 6% strain. 50

4.20 Diagram of the chain-end locations for each of Variants I, II, and III (not to scale). Each diagram shows representative single sheet of 8 chains. The simulation cell for each variant consists of 8×8×64 unit cells. 51
4.21 Stress-strain response of Variants I, II, and III, as well as perfectly crystalline PPTA (8×8×64 unit cells), using ReaxFF. 52
4.22 Stress-strain and bond break histories for Variant I obtained from the PCFF and ReaxFF force fields. 53
4.23 Stress-strain and bond break histories for Variant II obtained from the PCFF and ReaxFF force fields. 54
4.24 Stress-strain and bond break histories for Variant III obtained from the PCFF and ReaxFF force fields. 54
4.25 Stress-strain and bond break histories for Variant IV obtained from the PCFF and ReaxFF force fields. The ReaxFF model does not predict any primary bond breakages in this case. 55
4.26 PCFF stress-strain response for Variant IV. 55
4.27 ReaxFF stress-strain response for Variant IV. 56
4.28 Failure strain versus strain rate for both PCFF and ReaxFF models of Variant IV. 56
4.29 The crack propagation path suggested by Morgan et al. [48], showing rupture of hydrogen bonds between adjacent PPTA chains in the fiber. 57
4.30 Modulus versus n_z for both PCFF and ReaxFF. 58
4.31 Normalized crystal modulus versus inverse of chain length for both PCFF and ReaxFF. The dotted lines represent a best fit of the parameter a of equation (4.11) to the data. Reasonable agreement is obtained. 61

5.1 Progression of bond ruptures in a crystalline sheet of PPTA. Figure (a) shows the sheet before bond failure. Figure (b) shows the initial bond failure site. In Figure (c), the broken chain "snaps" as the potential energy in the bond is released as kinetic energy; this results in broken hydrogen bonds between the broken chain and adjacent chains. In Figures (d)–(f), the remaining chains fail one by one in rapid succession. 66
5.2 An 8×8×64 perfect crystal system is strained at a rate of $\dot{\epsilon} = 1.0 \times 10^9$ s^{-1}. The zoomed-in view in (b) highlights that multiple bonds break before the stress reaches its maximum value and begins to drop. 67
5.3 An 8×8×64 perfect crystal system is strained at a rate of $\dot{\epsilon} = 2.0 \times 10^8$ s^{-1}. The zoomed-in view in (b) highlights that multiple bonds break before the stress reaches its maximum value and begins to drop. 68
5.4 The distribution of times to first failure for the 3×4×2 system. The red curve is the exponential distribution with $\lambda_N = \frac{1}{\mu_N}$, where μ is the average time to first failure among the 400 simulations. 72
5.5 The distribution of times to first failure for the 4×4×8 system. The red curve is the exponential distribution with $\lambda_N = \frac{1}{\mu_N}$, where μ is the average time to first failure among the 400 simulations. 73

5.6 Relation between failure rate λ_0 and strain obtained from ReaxFF MD simulations performed at a temperature of $T = 300$ K. 75
5.7 Relation between failure rate λ_0 and temperature obtained from ReaxFF MD simulations performed at a strain $\epsilon = 0.090$. 76
5.8 Strain at first failure for runs at several strain rates and temperatures using a simulation cell consisting of 4×4×8 unit cells of perfectly crystalline PPTA. . . 77
5.9 Model fit to first failure data at 300 K. 78
5.10 Model fit to first failure data at 400 K. 78
5.11 Model fit to first failure data at 500 K. 79
5.12 Failure of a single sheet in a model consisting of 4×4×8 unit cells with one chain end per cell positioned randomly within the sheet. Figure (a) presents the sheet at zero strain, and Figure (b) shows the sheet in its failed state. The failure path is highlighted in yellow. Surrounding periodic cell replications (due to periodic boundary conditions) are not shown. 80
5.13 Failure patterns tested in strain-to-failure simulations using the PCFF force field. The red dots represent chain-end locations. 82
5.14 Failure strain versus number of bonds along the shortest path to failure. Each failure strain value is an average over five PCFF simulations performed at a strain rate of 1.0×10^9 s^{-1}. 83
5.15 Stress-strain curves for Patterns D_5 and D_8 for $\dot{\epsilon} = 1.0 \times 10^9$ s^{-1} using the PCFF force field. 83
5.16 Failure of Pattern D_5 with PCFF. 84
5.17 Failure of Pattern D_8 with PCFF. 85
5.18 Failure of Pattern D_5 with ReaxFF. Primary bond breaks occur near the chain-end defects in the sheet. 87
5.19 Failure of Pattern D_3 with ReaxFF. Primary bonds remain intact, and failure occurs through chain sliding and hydrogen bond failure. 88
5.20 Pattern E 90
5.21 Strain at first hydrogen bond failure at several strain rates and temperatures for Pattern E simulated using PCFF. 91
5.22 Model fit to first hydrogen bond failure data at 300 K. 91
5.23 Model fit to first hydrogen bond failure data at 400 K. 92
5.24 Model fit to first hydrogen bond failure data at 500 K. 92

List of Tables

2.1 Mechanical properties of various grades of PPTA fiber, as reported in [2]. 10

3.1 Equilibrium molecular geometry computed with PCFF and ReaxFF, compared to the X-ray diffraction measurements by Northolt [52]. The uncertainty labels in the left column headings refer to the standard error in the time averages for the measurements taken here with PCFF and ReaxFF. 25

3.2 Elastic constants (units in GPa) computed using the PCFF and ReaxFF force fields in this thesis, alongside literature calculations. All values are computed at a temperature of 300 K, with the exception of the DREIDING force field values, which were computed at 0 K. The standard error in the time averaging of the elastic constants performed here is ± 1 GPa. 28

5.1 The failure rate of a single bond λ_0 is calculated based on the mean time to first failure μ_0 for the simulation data presented in Figures 5.4 and 5.5. The 95% confidence interval for the estimated value of λ_0 is shown in the final column. . . 72

Acknowledgments

I would like to thank both Professor Panayiotis Papadopoulos of U.C. Berkeley and Dr. Edward Zywicz at the Lawrence Livermore National Laboratory for all of their guidance and support during my graduate career. I would also like to thank Richard Gee and William Kuo at the Lawrence Livermore National Laboratory for their help in introducing me to LAMMPS and running molecular dynamics simulations in a high performance computing environment. This project would never have been started without their guidance and assistance at the outset. Finally, I am grateful to the Lawrence Graduate Scholar Program for providing the funding and computational resources which made this project possible.

This work was performed under the auspices of the U.S. Department of Energy by Lawrence Livermore National Laboratory under Contract DE-AC52-07NA27344.

Chapter 1

Introduction

Synthetic polymer fibers play a key role in many engineering applications including fiber-reinforced composites, ropes, cables, sporting equipment, and woven fabrics. Among the strongest of man-made polymer fibers are aromatic polyamides, or aramid fibers, the most well-known examples of which are the trademarked fibers Kevlar® and Twaron®. Aramid fibers exhibit an impressive strength-to-weight ratio five times that of steel, good abrasion and creep resistance, and maintain performance at temperatures as high as 170 °C [20]. These remarkable properties have led to aramid fibers being heavily used in projectile-resistant fabrics such as personal protective vests and helmets, jet engine enclosures, and flame-retardant clothing [2].

The properties of aramid fibers stem directly from their rather unique microstructure. The building block of aramid fibers is the monomer p-phenylene terephthalamide (PPTA). In aramid fibers, PPTA monomers link together to form very long-chain polymers, typically 150–200 monomers (about 200–250 nm) in length. During the fiber manufacturing process, PPTA polymer chains become highly aligned with the fiber axis and arranged into a highly crystalline structure. Chains are held together laterally through strong hydrogen bonding and van der Waals forces. The high degree of chain alignment and crystallinity, combined with strong intermolecular forces binding the chains together laterally, are the primary reasons for the exceptional strength and stiffness properties of aramid fibers.

However, like all materials, manufactured aramid fibers contain defects and imperfections in their microstructure which will lead variations in their material properties. For example, Kevlar fibers come in several grades, such as Kevlar 29, 49, and 149. Each grade has a different percentage crystallinity, polymer chain orientation distribution, and concentrations of impurities and defects, leading to different mechanical properties for each grade. Hence, the microstructural details of the fiber have a very strong effect on the overall mechanical properties of the fiber. Efforts have been made to construct models which are capable to predicting the various mechanical properties of aramid fibers given knowledge of their microstructural details. For example, Northolt et al. [53, 51, 54] use knowledge of the elastic properties of crystalline PPTA and the distribution of chain orientation angles relative to the fiber axis to predict the modulus of a fiber. Rao et al. [59] derived a model based on experimental

results which identifies the chain orientation distribution and the paracrystalline parameter (a measure of the crystallinity of the fiber microstructure) as the two main factors that influence the fiber modulus. These models work well for predicting the axial fiber modulus for most grades of Kevlar fibers, and demonstrate how knowledge of the microstructural details of the fiber can be used to obtain predictions of fiber mechanical behavior.

Models like those proposed by Northolt and Rao use averaged measurements of fiber microstructural properties, but they do not account for finer-scale details which are also important in understanding fiber behavior. Multiple studies [56, 48, 47, 40] have shown that the details of the atomic-level fiber microstructure are quite complex, including a distinct difference in polymer chain organization between the skin and core of the fiber, periodically repeating defect planes along the fiber axis, and chemical impurities that are introduced during the fiber manufacturing process. While these microstructural details clearly have an influence on the macroscopic fiber behavior, it is not well understood the extent to which each might contribute, since this cannot be easily measured experimentally.

One tool that can assist in studying the influence of microstructure on macroscopic fiber behavior is molecular dynamics. Molecular dynamics (MD) involves simulating the trajectory of a system of atoms, modeling each atom as a point mass interacting with surrounding atoms through an interatomic potential energy function. Combined with principles from statistical mechanics, MD can be used to predict a number of macroscopic material properties, and given its ability to model atomic structure explicitly, it can be used to construct a model of aramid fibers capable of including all types of structural defects, and the resulting influence of these defects on macroscopic behavior. It is important to recognize that due to the relatively large length scales involved in the hierarchy of fiber microstructural details, MD simulations are only capable of modeling relatively small crystalline regions of PPTA consisting of perhaps hundreds of thousands of atoms. However, gaining understanding of the fundamental behavior of PPTA crystals within the fiber is paramount to understanding the resulting macroscopic behavior of the fiber as a whole.

MD has been previously recognized as a useful tool for studying the behavior of crystalline PPTA, and as such there is a body of literature on molecular dynamics modeling simulations of crystalline PPTA. For example, studies have been performed to predict the ideal molecular geometry and chain conformations [13, 74], elastic moduli [38, 72], and compressive failure due to chain buckling [37]. The more recent work of Grujicic et al. [20, 21, 22, 24, 23, 25] represents the most comprehensive set of studies to date. These studies focused on modeling various defect patterns and impurities, as well as tensile, torsion, and compressional loading, and the resulting elastic moduli and axial strength of PPTA crystals.

One important topic that the literature neglects with regards to MD simulations of PPTA fibers is the dynamic axial strain rate loading of PPTA crystals. Some experimental results [66, 27] suggest that Kevlar fibers and fabric exhibit strain-rate dependent failure strain and/or elastic modulus. In applications such as bullet-proof vests, fibers are loaded at very high strain rates (100–10,000 s^{-1}), making the understanding of any strain rate dependent behavior crucial to constructing material models of fiber behavior. The source of this rate-dependent behavior is postulated to come from how primary and secondary bonds in the

fibers break as the fiber is loaded, with different strain rates leading to different breaking mechanisms and thus different mechanical behavior [66, 73]. However, it is interesting to note that several researchers [41, 9] have not found significant changes in modulus or other mechanical properties with strain rate. With conflicting reports and theories on the importance of strain rate loading on the behavior of aramid fibers, molecular dynamics emerges as an appropriate tool to analyze the details of the molecular response to dynamic strain rate loading and clarify how the rate of loading influences overall mechanical behavior.

Since the rate-dependent behavior of PPTA is hypothesized to depend on the rupture of both primary and secondary bonds, it is important to choose an MD modeling strategy that allows for the forming and breaking of primary bonds as the simulation progresses. Such a strategy also permits the study of the strength and failure behavior of PPTA under strain rate loading, a topic of great importance when considering applications such as life-saving personal protective armor. However, standard molecular dynamics potentials typically model chemical bonds as springs (linear or nonlinear) which are permanent features of the molecule topology during simulation. Simply breaking the springs using a distance criteria to represent bond rupture is problematic due to the inability to capture changes in partial atomic charges and bond strength with neighboring atoms (that is, chemical changes in the polymer) that would accompany such an event in a true PPTA molecule.

The problem of breaking chemical bonds dynamically during a simulation can be solved by turning to reactive bond order force fields such as ReaxFF (for "Reactive Force Field"). ReaxFF [17, 18, 67, 50] was originally developed to study chemical reactions involving hydrocarbons, but has had alternative parameterizations created to study a wide range of other materials as well. ReaxFF captures changes in bond topology as a simulation progresses, updating atomic charges and bond orders to reflect any chemical reactions that take place during the simulation. It represents somewhat of a hybrid methodology between quantum mechanical and molecular dynamics simulations – simulations with ReaxFF can simulate much larger systems than in quantum mechanical simulations, but are more costly to perform compared to simulations using classical MD potentials. While originally intended to model thermodynamically activated chemical reactions, ReaxFF has been successfully employed to model material fracture and failure through mechanical bond rupture, [35, 64, 36, 12, 11, 7], making it a good candidate for studying bond rupture events and the failure behavior of crystalline PPTA.

This dissertation seeks to contribute to the understanding of the mechanical behavior of crystalline PPTA by using molecular dynamics to model the response of PPTA molecules to dynamic strain rate loading. By using the reactive bond order potential ReaxFF, MD simulations can be used to predict both the strain rate dependent mechanical response of the crystals and the failure mechanisms involved in strain-to-failure loading, both of which are important to improving the current understanding of aramid fiber behavior. The studies presented here are unique compared to previous MD studies of PPTA behavior, and with the introduction of dynamic strain rate loading into the simulations, represent realistic loading conditions that emerge in standard applications of PPTA fibers as projectile-resistant woven fabrics.

The remainder of this dissertation is organized as follows: Chapter 2 presents a detailed summary of the known microstructural characteristics of PPTA in order to inform the implementation of molecular dynamics modeling of crystalline PPTA. Chapter 3 presents a review of the important aspects of molecular dynamics theory and implementation, and presents preliminary simulation results which show that the molecular dynamics methods used here are capable of accurately modeling the behavior of crystalline PPTA. Chapter 4 presents constant strain rate simulations of highly crystalline PPTA, exploring the influence of defects and temperature on the modulus and failure response of the crystals. Chapter 5 examines bond failure in crystalline PPTA in detail, and leverages the stochastic nature of bond failure to model the failure of both primary and secondary bonds using concepts from reliability theory. Finally, Chapter 6 summarizes the findings and contributions of this dissertation.

Chapter 2

PPTA fiber morphology and mechanical properties

PPTA fibers are characterized by highly crystalline arrangements of PPTA molecules aligned parallel to the fiber axis. However, the details of the underlying microstructure are far more complex than this basic idealization. The morphology of a typical aramid fiber actually comprises a hierarchy of microstructures, ranging from the nanoscale to the microscale, each with their own set of structural imperfections. The nature of these imperfections directly influences the mechanical properties of the fiber at the macroscale. A molecular-level model of the fiber has the potential to be used to understand the influence of some of these structural defects on macroscopic mechanical fiber properties; however, it is important to understand the details of the fiber microstructure in order to create such a model. Additionally, one must understand how these details influence overall macroscopic fiber behavior in order to understand what kinds of simulations to apply the molecular model to. As such, this chapter presents an overview of the literature on what is known about the microstructure of PPTA fibers, and how those microstructural features influence the overall macroscopic fiber behavior. It will be shown that while the overall structure is complex, the basic building block of fiber structure, the crystallite, is simple enough to be amenable to molecular dynamics modeling, which can be used to help improve understanding of of the overall fiber behavior.

2.1 PPTA fiber morphology

At the most fundamental level, PPTA fibers contain extended PPTA polymer chains packed into a highly crystalline arrangement. The PPTA monomer is pictured in Figure 2.1, and contains a total of 28 atoms. These monomers align end-to-end to form long polymer chains. The PPTA fiber manufacturing process aligns the chains nearly parallel along the fiber axis through a dry-jet wet spinning process, typically yielding fibers about 12 μm in diameter. The structure of the chains within crystalline regions of the fiber is described by the orthogonal crystalline unit cell pictured in Figure 2.2, with dimensions $a = 0.787$ nm,

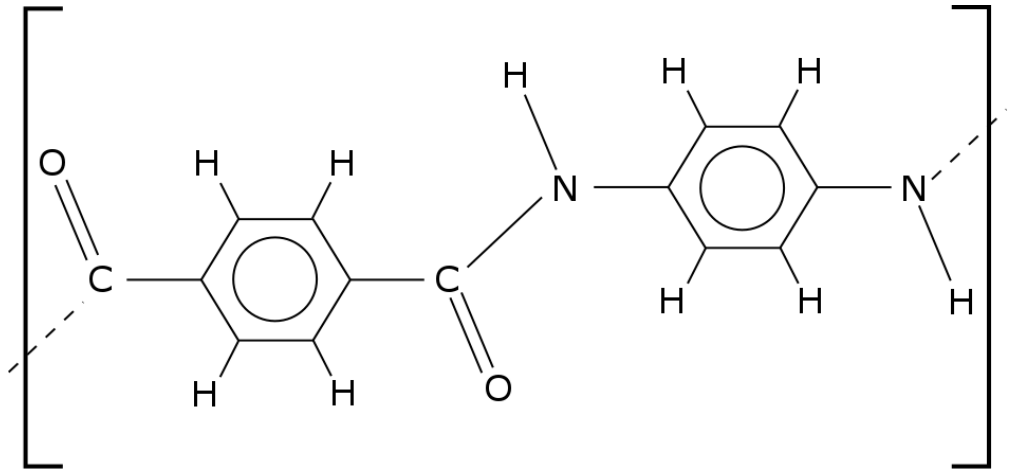

Figure 2.1: *Diagram of a single PPTA monomer.*

$b = 0.518$ nm, and $c = 1.29$ nm [52]. The chains are held together by hydrogen bonds in the b-direction, as well as van der Waals forces occurring in the a-direction. This arrangement of aligned chains held together by strong hydrogen bonds is responsible for the high stiffness and strength of PPTA fibers along the fiber axis direction; conversely, its transverse and shear stiffness and strength are significantly lower, typically by at least an order of magnitude.

Studies by Dobb et al. [14, 15, 16] showed that chains tend to organize themselves into hydrogen-bonded sheets, and that these sheets are arranged radially within the fiber. Furthermore, Dobb noted a periodicity in the structural pattern of the fibers of about 500 nm. He concluded that the periodicity was most likely explained by the existence of a pleated structure repeating along the fiber axis, as shown in Figure 2.3. The pleats are angled about 10° relative to the fiber axis, and within each pleat are long chains arranged in the highly crystalline organization described by the unit cell in Figure 2.2. This crystalline, pleated-sheet structure is the most basic representation of PPTA fiber macromolecular morphology and applies to all variants of Kevlar and Twaron fibers.

However, underlying this pleated-sheet description of the fiber morphology is an arrangement of polymer chains which, while highly crystalline, contains a number of different defects and imperfections which can strongly influence the overall fiber properties. Several studies using a variety of observation techniques [56, 48, 40] were conducted independently of one another in order to characterize the details of this microstructure. However, the complexity of the microstructure has led to disagreement on the exact microstructural details. Figures 2.4–2.6 show the different models that these studies have suggested to explain their experimental observations. While the details of each group's findings vary, there are several characteristics that each model agrees on:

- The primary building block of fiber microstructure is the *crystallite*. A crystallite is a region where the packing of polymer chains is highly crystalline. Researchers have disagreed on some of the details of their size, for example, Panar et al. [56] believe the

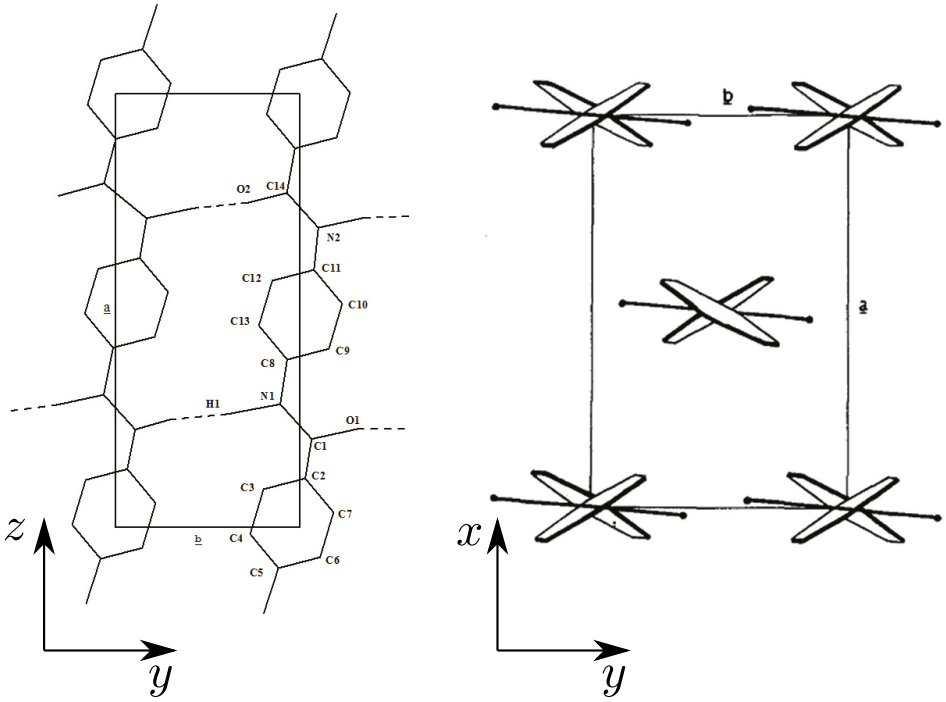

Figure 2.2: *Crystalline unit cell for PPTA [52]. The x, y, and z Cartesian axes correspond to the a, b, and c crystalline unit cell dimensions, respectively. The z axis corresponds to the fiber axis.*

crystallites are about 600 nm in diameter, while Morgan et al. [48] report a crystallite diameter of 60 nm. However, all sources agree that the crystallite length is in the neighborhood of 200 nm, about the same length as the PPTA polymer chains in the fiber. Within a crystallite, chains are highly parallel to one another, although the crystallite itself may not be perfectly aligned with the fiber axis, resulting in imperfect chain alignment with the fiber axis.

- Defect planes occur periodically along the fiber axis. The defect planes are essentially planes where crystallites end, and as such, the defects are believed to be concentrated collections of chain-ends. Panar et al. [56], for example, suggest that these planes contain 50% chain ends, relative to the number of chains passing through them, as depicted in Figure 2.4a. Despite these seemingly weak planes, PPTA fibers retain their strength largely due to the presence of extended chains passing through these defect bands. Panar et al. [56] observe a defect plane periodicity of about 35 nm. Li et al. [40] observe a similar periodicity, around 20–30 nm.

- A typical PPTA fiber contains a thin skin region about 0.1–1.0 μm in thickness, and a core region that makes up the rest of the interior of the fiber, as shown in Figures 2.5 and 2.6. The structural organization of the polymer chains in each region is different. The core contains the aforementioned defect planes of concentrated chain-ends, while

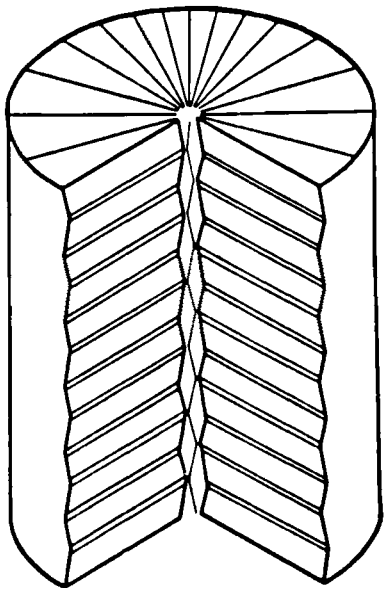

Figure 2.3: *Radial system of pleated lamella postulated in [15, 16].*

the chain-ends within the skin are believed to be randomly distributed along the fiber axis.

While these findings paint an overall complex picture of the fiber, one important takeaway is that the crystallite is the fundamental building block of the PPTA fiber. Understanding the mechanical behavior of a single crystallite is informative for making predictions about the macroscopic properties of the fiber as a whole. This motivates the molecular dynamics modeling of PPTA crystallites, where the effects of various types of defects at the molecular level can be simulated explicitly.

2.2 PPTA fiber properties

All PPTA fibers consist of the same crystallite-based microstructure as described in Section 2.1. However, the details of the arrangements of the polymer chains within those crystallites is highly dependent upon the manufacturing process. For example, Kevlar fibers exist in several different grades, such as Kevlar 29, 49, and 149, and each have different mechanical properties. PPTA fibers are typically used in applications where they are loaded in tension along the fiber direction (as opposed to transversely), and as such, the most important and oft-reported mechanical properties are the longitudinal stiffness and strength. Table 2.1 provides a summary of the tensile axial modulus and failure stress/strain of some different varieties of Kevlar and Twaron fibers, as reported in the review article by Ahmed et al. [2].

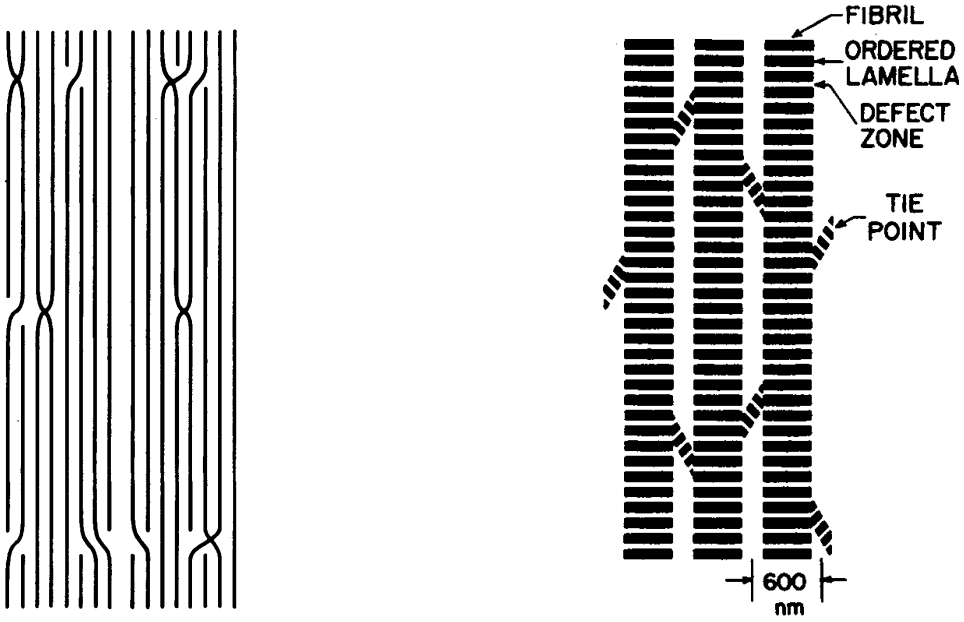

Figure 2.4: *The model by Panar et al. [56] shows the periodic defect planes with long polymer chains extending through them, and also the tie points that were hypothesized to assist in holding parallel fibrils together.*

The difference in mechanical properties between fiber grades and manufacturers is strongly linked to the microstructural details of the fibers. Rao et al. [59] performed a comprehensive study to determine the most important characteristics which determine the macroscopic fiber properties, and found that fiber properties could be determined with good accuracy by using the following empirically-determined relationship:

$$\frac{1}{E_f} = \left(\frac{1}{E_0} + D_1 g_{II}^2\right) + A < \sin^2 \phi > , \tag{2.1}$$

where E_0 represents the crystallite modulus, g_{II} is the paracrystalline parameter, ϕ is the chain orientation relative to the fiber axis, and D_1 and A represent material constants. Using this formula, Rao et al. were able to accurately predict the fiber modulus based on the paracrystalline parameter and chain orientation, and also deduced that the crystal

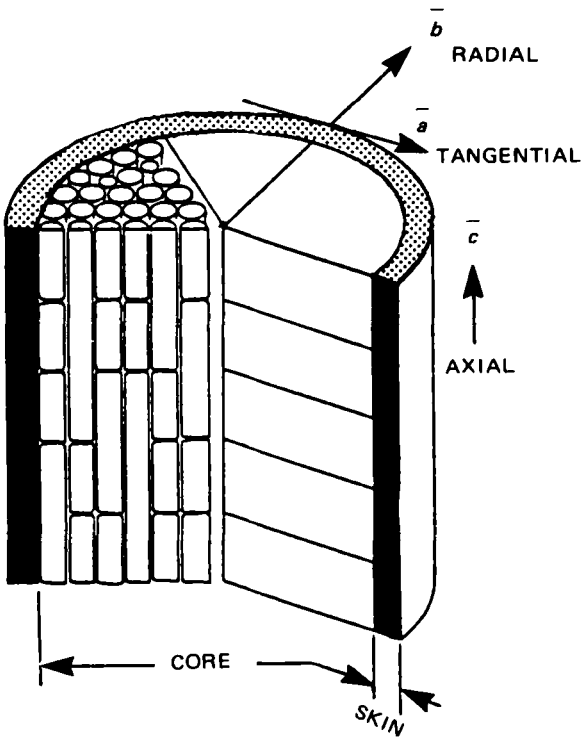

Figure 2.5: *Li et al. [40] highlight the skin-core difference, crystallite distribution, and repeating defect planes along the fiber axis, as well as the radial arrangement of hydrogen-bonded sheets.*

Product name	Kevlar 29	Kevlar 49	Kevlar 149	Twaron 2000
Tensile modulus (GPa)	70	135	143	90
Tensile strength (GPa)	2.9	2.9	2.3	3.8
Elongation at failure (%)	3.6	2.8	1.5	3.5

Table 2.1: *Mechanical properties of various grades of PPTA fiber, as reported in [2].*

modulus E_0 was approximately equal to 250 GPa for all Kevlar fiber grades tested, which is in reasonable agreement with theoretical predictions [74]. Such work highlights the strong dependance of overall fiber properties on the details of the fiber microstructure.

Another important aspect of PPTA fiber properties is the dependence of fiber modulus and failure strain on applied strain rate. The rate-dependence of the modulus has particularly been a subject of study, given the important role it would play in modeling high-velocity projectile impact on bullet-proof vests, one of the more popular applications for PPTA fibers. Several studies [66, 77, 81, 73, 27] found that strain rate has a significant effect on fiber (or fabric) modulus and/or strength, with the general trend being that both modulus and failure strain increase with increasing loading rate. The hypothesis for explaining this rate-

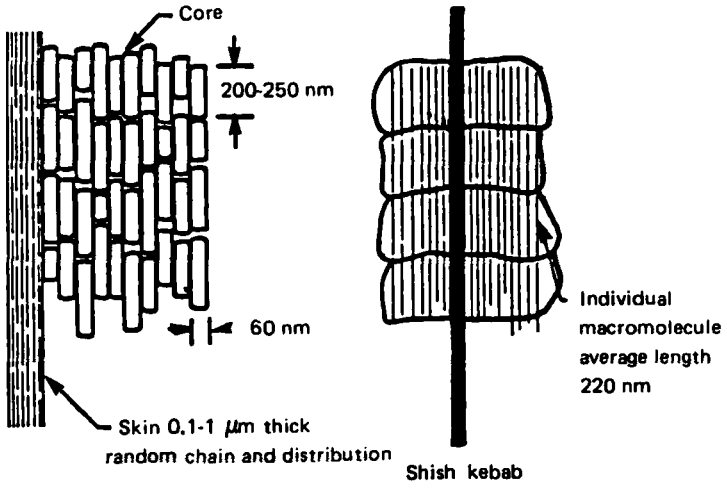

Figure 2.6: *The model proposed by Morgan et al. [48] is similar to the Li et al. [40] model, and focuses on the skin-core structural difference and the "Shish kebab" nature of the stacked lammelar structure.*

dependent modulus effect is that it results from the different ways that primary backbone bonds and secondary hydrogen bonds rupture at different strain rates [66]. At fast rates, is is theorized that there is no time for inter-chain slippage, resulting in a brittle fracture mechanism involving mostly primary bond failure, while at slower strain rates, there is more time for chains to slip by one another via secondary bond failure, resulting in a reduction in modulus before the onset of failure. However, other studies [41, 9, 39] have found that strain rate has a negligible effect on modulus and/or failure strain. These studies have focused on single fibers or bundles of fibers, while the studies that have reported strain rate effects have focused on single yarns or fabric patches, and often use Twaron fibers as their test material, which suggests that the strain rate effects depend explicitly on both micro- and macro-molecular fiber morphology.

Clearly, fiber properties including stiffness, strength, and strain rate dependent behavior are dependent on the details of the fiber microstructure, and while relevant microstructural features span several length scales, a significant portion of the important details lie at the crystallite level, where the arrangement and behavior of individual polymer chains governs the crystallite response. For this reason, molecular dynamics is a useful tool for exploring the crystallite behavior and providing a better understanding of how different types of structural features and defects can influence PPTA fiber mechanical properties. In particular, in the following chapters, molecular dynamics modeling will be used to explore the effects of different types of defect patterns on the overall macroscopic fiber behavior. It will also be used to perform strain rate loading simulations of crystalline PPTA in order to observe whether there are strain rate effects which can be attributed to the rupture of primary and secondary bonds, or any other molecular-level mechanisms.

Chapter 3

Molecular dynamics modeling of PPTA crystals

As discussed in Chapter 2, PPTA fibers have a complex microstructure whose characteristic length scale is on the order of hundreds of nanometers, and the macroscopic fiber properties depend crucially on the details of this microstructure. The fundamental building block of this microstructure is the PPTA crystallite, which contains highly crystalline arrangements of aligned polymer chains. Therefore, to begin to understand the properties of the macroscopic fiber, it is important to understand the properties of these crystallites. The key factors influencing the crystallite properties reside at the atomic level – for example, the exact arrangement of chains within the crystallite, and the presence of impurities or other structural defects within the chains and their overall crystal structure.

In situations like these, molecular dynamics (MD) is a useful tool which can be used to compute physical properties of a material based on its atomic structure. MD essentially allows one to perform computer experiments on an atomic system, and gives access to detailed information that could not be observed experimentally. MD simulations also give the ability to introduce defects or other changes into the model of a material's atomic structure and observe the effect they have on the overall macroscopic properties; such precise changes to material microstructure are often not possible in experiments.

The defining characteristic of an MD simulation is the interatomic potential used to model the force interactions between atoms, and this potential must be carefully chosen if the simulation is to represent the behavior of the true material. The work that follows utilizes two different force fields to model PPTA: PCFF and ReaxFF. PCFF (Polymer Consistent Force Field) is a classical potential appropriate for modeling polymers. It is capable of modeling PPTA crystallite behavior and reliably computing physical properties at low to moderate strains. ReaxFF (for "Reactive Force Field") is a reactive bond order potential, which has the ability to break and form bonds dynamically during a simulation; in contrast, the bonding topology in the PCFF force field is permanent. ReaxFF is much more computationally expensive, but the ability to update bonding topology over the course of a simulation will allow for the investigation of the properties of PPTA crystallites due to bond breakage, such

as crystallite failure behavior.

In this chapter, the details of the MD potentials and simulation methodologies used to model PPTA crystallites are discussed, and the MD potentials are validated against both known physical properties and MD simulation results from literature in order to justify their application to modeling crystalline PPTA.

3.1 Selection and description of interatomic potentials

In this work, two different interatomic potentials will be used. The first is the PCFF force field, a classical potential suitable for modeling organic polymers. It is applicable to situations in which the equilibrium molecular geometry (bonds, angles, etc.) does not undergo extensive deformations. The second potential that will be used is ReaxFF, a reactive bond order potential capable of breaking and forming atomic bonds dynamically as the simulation progresses. Since this work is interested exploring the behavior of PPTA crystallites under extreme loading conditions that are expected to cause primary bond rupture along the chain backbone, this force field will be used to study such cases.

3.1.1 The PCFF potential

The interatomic potential PCFF (Polymer Consistent Force Field) is a Class II force field [71] whose general form is:

$$E_{total} = E^b + E^a + E^o + E^t + E^{bb} + E^{ab} + E^{aa} + E^{at} + E^{bt} + E^{elec} + E^{VDW} \ , \qquad (3.1)$$

where

$$
\begin{aligned}
E^b &= \sum_{i=2}^{4} k_i^b (b - b_0)^i \ , \\
E^a &= \sum_{i=2}^{4} k_i^a (\theta - \theta_0)^i \ , \\
E^t &= \sum_{i=1}^{4} k_i^a (1 - \cos i\phi) \ , \\
E^o &= k^o (\chi - \chi_0)^2 \ , \\
E^{bb} &= k^{bb} (b - b_0)(b' - b'_0) \ , \\
E^{aa} &= k^{aa} (\theta - \theta_0)(\theta' - \theta'_0) \ , \\
E^{ab} &= k^{ab} (b - b_0)(\theta - \theta_0) \ , \\
E^{bt} &= (b - b_0) \sum_{i=1}^{3} k_i^{bt} (1 - \cos i\phi) \ , \\
E^{at} &= (\theta - \theta_0) \sum_{i=1}^{3} k_i^{bt} (1 - \cos i\phi) \ , \\
E^{elec} &= \sum_{i,j} \frac{q_i q_j}{r_{ij}} \ , \\
E^{VDW} &= \sum_{i,j} \epsilon_{ij} \left[2 \left(\frac{\sigma_{ij}}{r_{ij}} \right)^9 - 3 \left(\frac{\sigma_{ij}}{r_{ij}} \right)^6 \right] \ .
\end{aligned}
\tag{3.2}
$$

In equations (3.2), E^b, E^a, E^t and E^o represent the bond, angle, torsion, and out-of-plane interactions, respectively, with b indicating bond length, θ indicating three-body angle, ϕ indicating the torsion angle, and χ indicating the out-of-plane angle. The energies E^{bb}, E^{aa}, E^{ab}, E^{bt}, and E^{at} represent coupled energetic interactions with bond-bond, angle-angle, bond-angle, bond-torsion, and angle-torsion pairs, which help enforce additional molecular conformations. E^{elec} is the standard Coulomb interaction energy, dependent upon the charges of two atoms i and j denoted by q_i and q_j, and the interatomic distance $r_{ij} = |\mathbf{r}_i - \mathbf{r}_j|$, with $|\cdot|$ indicating the vector-norm. Finally, E^{VDW} represents a 9-6 type Lennard-Jones interaction.

The PCFF force field is parameterized from *ab initio* theoretical calculations, and is designed specifically to model polymers and organic compounds. The PCFF force field has been used in several MD studies of PPTA [62, 63, 38, 37] to calculate molecular geometry, possible chain conformations, physical properties like the crystalline elastic moduli and coefficient of thermal expansion, and buckling behavior under axially compressive loading. Grujicic et al. [20, 21, 22, 24, 23, 25] use a more recently parameterized Class II force field known as COMPASS [70] to conduct a variety of MD simulations of PPTA, including simulating the effects of various classifications of defects and the effect of different loading

conditions on the material response. Given that PCFF was parameterized to model organic compounds like PPTA, and that it has been successfully used (along with its similar counterpart COMPASS) to model PPTA in previous MD studies, it is deemed a reasonable choice for modeling PPTA in this work.

3.1.2 The ReaxFF potential

ReaxFF is a reactive bond order force field [17] capable of modeling the breakage and formation of covalent bonds dynamically during a simulation. Bond order is essentially a measure of the strength of a chemical covalent bond. It is roughly equivalent to the number of chemical bonds between two atoms, for example, a bond order of 2 typically signifies a double bond between atoms, but it need not only take integer values. The higher the bond order, the stronger the bond and the more difficult it is to separate the atoms; conversely, as bond order tends towards zero, so does the attractive force between two atoms.

In ReaxFF, it is assumed that the bond order between two atoms is dependent only upon interatomic distance. The fundamental equation which ReaxFF uses to determine the bond order between a pair of atoms i and j separated by distance r_{ij} is

$$\begin{aligned} BO'_{ij} &= BO'^{\sigma}_{ij} + BO'^{\pi}_{ij} + BO'^{\pi\pi}_{ij} \\ &= \exp\left[p_{bo,1}\left(\frac{r_{ij}}{r_0^{\sigma}}\right)^{p_{bo,2}}\right] + \exp\left[p_{bo,3}\left(\frac{r_{ij}}{r_0^{\pi}}\right)^{p_{bo,4}}\right] + \exp\left[p_{bo,5}\left(\frac{r_{ij}}{r_0^{\pi\pi}}\right)^{p_{bo,6}}\right] , \end{aligned} \tag{3.3}$$

where $p_{bo,1}$, $p_{bo,2}$, $p_{bo,3}$, $p_{bo,4}$, $p_{bo,5}$, $p_{bo,6}$, r_0^{σ}, r_0^{π}, and $r_0^{\pi\pi}$ are force field parameters assigned for interactions between atoms i and j. This essentially sums the bond order contribution of sigma, pi, and double-pi bonds, each of which can take a bond order value between 0 and 1, to give a total bond order which lies between 0 and 3. Bond orders BO'_{ij} are then multiplied by a correction factor which accounts for overcoordination (unphysical distributions of electrons) in order to obtain the true bond order BO_{ij}. From here, it is further assumed that all energy terms related to bonds, angles, and torsions are functions of bond order, and hence ultimately functions of atomic coordinates. The total energy of the system is calculated as

$$E_{total} = E_{bond} + E_{over} + E_{under} + E_{val} + E_{pen} + E_{tors} + E_{conj} + E_{vdWaals} + E_{Coul} , \tag{3.4}$$

which accounts for energies due to bonds, over- and under-coordination, valence angles and associated penalty terms, torsions, conjugations (e.g. repeated bond orders of 1.5 as in benzene rings), and standard van der Waals and Coulomb interactions. ReaxFF is designed to ensure that all of these energy terms smoothly transition to zero as bond order tends toward zero, allowing for a smooth transition between bonded and non-bonded energy states when chemical reactions (the breaking and forming of chemical bonds) take place. For example, the expression for the bond energy between atoms i and j is given as

$$E_{bond} = -D_e \cdot BO_{ij} \cdot \exp\left[p_{be,1}(1 - BO_{ij}^{p_{be,1}})\right] , \tag{3.5}$$

where D_e and $p_{be,1}$ are force field parameters assigned for interactions between atoms i and j. Expressions for the remaining terms are complex, and can be found in [17]. All terms are evaluated regardless of the presence of primary bonds between atoms. For example, van der Waals and Coulomb terms are always evaluated between pairs, but are negated through special shielding terms as the bond order between pairs increases. At every simulation time step, ReaxFF uses the atomic coordinates to determine the bond order between a given atom and all neighboring atoms, updates the bonding topology, and computes the resulting energies and forces on each atom.

The primary challenge with the ReaxFF potential is finding a suitable parameter set to model the material of interest. Originally parameterized for hydrocarbons [17], there exist many parameterizations of ReaxFF which extend its applicability to other materials, such as systems involving silicon-oxide reactions, [18], Fe/Al/Ni alloys [67], and transition metal catalyzed reactions involving carbon with Co, Ni, and Cu atoms [50]. However, there exists no parameter set that has been developed specifically for aromatic polyamides like PPTA, and using parameterizations for applications outside of their intended modeling situations requires careful validation of their performance in order to obtain trustworthy simulation results. For the simulations in this work, the ReaxFF parameterization of Liu et al. [42] is chosen. This parameter set was developed for applications to energetic materials composed of C, H, O, and N atoms, but was adapted from [69] to correct the London dispersion forces in order to more accurately replicate the crystal cell volume of several crystalline polymers, a good indication that it should be appropriate for modeling PPTA.

3.2 Molecular Dynamics Theory and Algorithmic Implementation

The objective of molecular dynamics is to numerically compute the the trajectory of a system of particles (represented by point masses) over a finite amount of time. The motion of each particle is assumed to be governed by Newton's equation

$$m_i \ddot{\mathbf{r}}_i = \mathbf{f}_i \ , \tag{3.6}$$

where the subscript i denotes the ith particle in the system of interest, and m is the mass, $\mathbf{r}$ is the position vector, $\mathbf{f}$ is the force, and $\ddot{(\cdot)}$ represents the second derivative of $(\cdot)$ with respect to time. The force $\mathbf{f}_i$ on atom i is assumed to be derivable from an interatomic potential $\mathcal{U}(\mathbf{r}^N)$, a function of all the atomic coordinates $\mathbf{r}^N = (\mathbf{r}_1, \mathbf{r}_2, ..., \mathbf{r}_N)$, and given by

$$\mathbf{f}_i = -\frac{\partial}{\partial \mathbf{r}_i} \mathcal{U}(\mathbf{r}^N) \ . \tag{3.7}$$

The potential $\mathcal{U}(\mathbf{r}^N)$ contains all of the energetic interactions present in the system, including energy contributions from bonds, angles, and dihedrals, and van der Waals and Coulomb interactions.

Equation (3.6) is an ordinary differential equation in time which can be solved approximately using numerical methods, making it amenable to solution via computer algorithms. In this work, the molecular dynamics simulation software LAMMPS [57] is used to conduct all MD simulations. LAMMPS employs efficient parallel algorithms capable of handling large-scale molecular simulations, and comes with a multitude of flexible simulation options and settings, making it appropriate for all of the simulations conducted in this work.

3.2.1 Integration of the equations of motion

In molecular dynamics, equation (3.6) is often represented as a system of two first-order ODE's written in terms of atomic coordinates $\mathbf{r}$ and momenta $\mathbf{p} = m\mathbf{v}$ as follows:

$$\begin{aligned} \dot{\mathbf{r}}_i &= \frac{\mathbf{p}_i}{m_i} \ , \\ \dot{\mathbf{p}}_i &= \mathbf{f}_i \ . \end{aligned} \tag{3.8}$$

Given initial atomic coordinates and velocities at time $t = t_0$, it is desired to compute the evolution of the system up to a final time t_f. There exist many numerical schemes which accomplish this. However, in molecular dynamics, it is often important to conserve the total system energy over time (to within numerical round-off error), and also important to minimize the number of force evaluations required in the scheme, since this is typically the most expensive operation during an MD simulation. Therefore, LAMMPS uses the symplectic velocity-Verlet algorithm for the numerical integration of (3.6). To implement the scheme, the time domain is broken into N_T segments of length Δt, allowing one to compute the solution at times $t = t_1, t_2, ...t_{N_T}$, where the time at the nth step is given by $t_n = t_0 + n\Delta t$. Given atomic coordinates $\mathbf{r}_i$ and velocity $\mathbf{v}_i$ for atom i at time t_n, the algorithm advances by a time step of length Δt and computes the atomic coordinates and velocity at time $t_{n+1} = t_n + \Delta t$ as follows:

$$\begin{aligned} \mathbf{r}_i(t_{n+1}) &= \mathbf{r}_i(t_n) + \mathbf{v}_i(t_n)\Delta t + \frac{1}{2}\mathbf{a}_i(t_n)\Delta t^2 \\ \rightarrow \mathbf{a}_i(t_{n+1}) &= -\frac{1}{m_i}\frac{\partial \mathcal{U}}{\partial \mathbf{r}_i}\left(\mathbf{r}^N(t_{n+1})\right) \\ \rightarrow \mathbf{v}_i(t_{n+1}) &= \mathbf{v}_i(t_n) + \frac{1}{2}\left[\mathbf{a}_i(t_n) + \mathbf{a}_i(t_{n+1})\right]\Delta t \end{aligned} \tag{3.9}$$

The method is second-order accurate , conserves energy to within numerical round-off error, and is efficient in its single force evaluation in computing the updated accelerations.

3.2.2 Periodic boundary conditions

Even with parallel computer algorithms to efficiently handle large numbers of interacting particles, molecular dynamics simulations are typically only viable for systems of thousands to millions of atoms. Simulating such a small quantity of atoms introduces surface effects at

the system boundaries, which is not a desirable if the goal of a simulation is to simulate the behavior of a bulk solid or liquid. To overcome this difficulty, periodic boundary conditions (PBCs) may be employed in the MD simulation. When periodic boundary conditions are applied, the simulation cell is assumed to be surrounded by an array of replications of the simulation cell, extending infinitely in each coordinate direction, as depicted in Figure 3.1. Since pairwise particle interactions (e.g. Coulomb or Lennard-Jones) become negligible with increasing distance, typically a cutoff radius r_c is introduced to the system, and the force interaction between any particles separated by a distance greater than r_c is omitted from the atomic force computations. It is important to choose a value of r_c that is less than twice the smallest dimension of the simulation cell or atoms will interact with images of themselves, which leads to unphysical atomic forces and motions. The introduction of the cutoff r_c is a reasonable approximation that keeps that cost of the simulation at a manageable size.

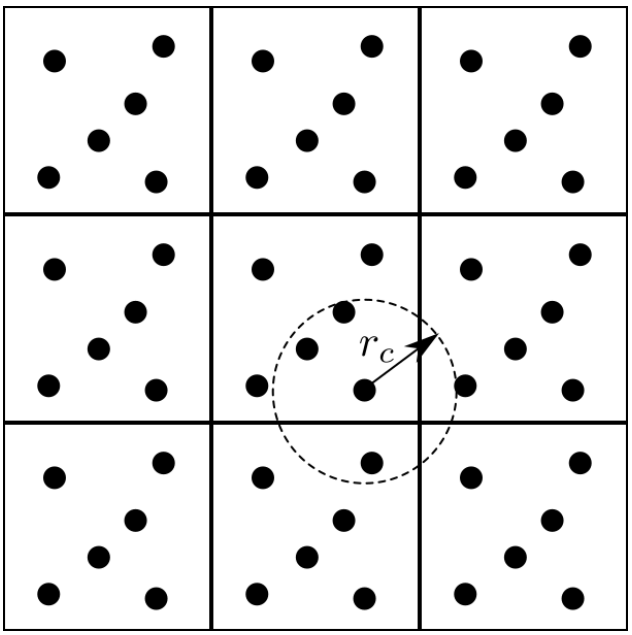

Figure 3.1: *An illustration of periodic boundary conditions and interaction cutoff radius r_c in an MD simulation.*

3.2.3 Controlling temperature and pressure

The simplest MD simulations hold the number of particles N and volume V of the simulation cell constant, while applying a symplectic integration scheme (e.g. velocity-Verlet (3.9)) to conserve total energy E. Such a simulation will yield the so-called NVE ensemble, named for the three quantities which are held constant in time, and is produced naturally from the equations of motion (3.8). However, it is often desired to perform simulations at constant temperature and/or pressure to model typical laboratory conditions, in which

case the NVE ensemble is not appropriate. To model such conditions, it is necessary to modify the equations of motion of the system to produce the NVT (constant number of particles, volume, and temperature) or NPT (constant number of particles, pressure, and temperature) ensembles. The augmented equations are constructed such that the specified temperature and/or pressure is held constant in a time-averaged sense. Algorithms which maintain a constant temperature over time are called *thermostats*, and algorithms which maintain constant temperature over time are called *barostats*. NVT and NPT algorithms are similar to one another and are often referred to collectively as thermostats, which will be the convention used in this work henceforth.

One of the most common thermostat/barostat algorithms is the Nosé-Hoover algorithm [55, 30], which essentially couple the dynamics of the system to an external temperature/pressure bath which maintains the desired time-averaged temperature/pressure. It has been shown that standard Nosé-Hoover does not work well except under special circumstances, but that coupling the motion to a chain of thermostats/barostats can overcome this deficiency [44]. Pressure control is governed by the fluctuation in the simulation cell dimensions, and in general, it is possible to control pressure components individually as described in [45] by controlling individual simulation cell dimensions rather than total volume. This decoupling of pressure components is particularly useful for modeling solid materials, which unlike liquids and gasses may undergo heterogeneous stress states. In LAMMPS, the implementation of the NPT ensemble (the most general case – the NVT case eliminates equations controlling pressure and the simulation cell fluctuations) is a M-chain Nosé-Hoover barostat with the equations of motion given in [68] as:

$$
\begin{aligned}
\dot{\mathbf{r}}_i &= \frac{\mathbf{p}_i}{m_i} + \frac{\mathbf{p}_g}{W_g}\mathbf{r}_i \ , \\
\dot{\mathbf{p}}_i &= \mathbf{f}_i - \frac{\mathbf{p}_g}{W_g}\mathbf{p}_i - \frac{1}{3N}\frac{\mathrm{Tr}[\mathbf{p}_g]}{W_g}\mathbf{p}_i - \frac{p_\xi}{Q}\mathbf{p}_i \ , \\
\dot{\mathbf{h}} &= \frac{\mathbf{p}_g}{W_g}\mathbf{h} \ , \\
\dot{\mathbf{p}}_g &= V(\boldsymbol{\sigma}^{MD} - \mathbf{I}P_{ext}) - \mathbf{h}\Sigma\mathbf{h}^T + \left(\frac{1}{3N}\sum_{i=1}^{N}\frac{\mathbf{p}_i^2}{m_i}\right)\mathbf{I} - \frac{p_{\xi_1}}{Q_1}\mathbf{p}_g \ , \\
\dot{\xi}_k &= \frac{p_{\xi_k}}{Q_k} \quad \text{for} \quad k = 1, ..., M \ , \\
\dot{p}_{\xi_1} &= \sum_{i=1}^{N}\frac{\mathbf{p}_i^2}{m_i} + \frac{1}{W_g}\mathrm{Tr}[\mathbf{p}_g^T\mathbf{p}_g] - (3N + d^2)kT_{ext} - p_{\xi_1}\frac{p_{\xi_2}}{Q_2} \ , \\
\dot{p}_{\xi_k} &= \left(\frac{p_{\xi_{k-1}}^2}{Q_{k-1}} - kT_{ext}\right) - p_{\xi_k}\frac{p_{\xi_{k+1}}}{Q_{k+1}} \quad \text{for} \quad k = 2, ..., M-1 \ , \\
\dot{p}_{\xi_M} &= \left(\frac{p_{\xi_{M-1}}^2}{Q_{M-1}} - kT_{ext}\right) \ .
\end{aligned}
\tag{3.10}
$$

In equations (3.10), $\mathbf{h}$ is the cell matrix, populated by the three vectors defining the simulation cell edges, $\mathbf{p}_g$ is the modularly invariant form of the cell momenta, and $\{\xi_k, p_{\xi_k}\}$ are the thermostat variable and its conjugated momenta of the kth thermostat of the chain. W_g and Q_k are the mass of the barostat and kth thermostat, respectively, and control the frequency of the fluctuations. In LAMMPS, rather than specifying these mass values explicitly, a time constant is prescribed which specifies the time to relax to the system to the desired temperature/pressure, and the thermostat/barostat masses are set internally. The quantity Σ is defined as

$$\Sigma = \mathbf{h}_0^{-1}(\mathbf{t} - \mathbf{I}P_{ext})\mathbf{h}_0^{T^{-1}} \ , \tag{3.11}$$

where $\mathbf{t}$ denotes the externally-specified pressure tensor. $P_{ext} = \mathrm{Tr}[\mathbf{t}]$ and T_{ext} represent the externally applied pressure and temperature, respectively. The internal pressure is denoted $\boldsymbol{\sigma}^{MD}$, which is computed as

$$\sigma_{ij}^{MD} = \frac{1}{V}\sum_{\alpha}^{N}\left[\sum_{\beta}^{N}(r_i^{\beta} - r_i^{\alpha})f_j^{\alpha\beta} - m^{\alpha}v_i^{\alpha}v_j^{\alpha}\right] \ , \tag{3.12}$$

where the superscripts α and β refer to atoms, subscripts denote Cartesian components, and the quantity $f_j^{\alpha\beta}$ is the jth component of force between atoms α and β. The numerical integration scheme for the equations of motion (3.10) that is used in LAMMPS closely follows the formulation proposed in [76].

3.2.4 Accounting for atomic charge

In the molecular dynamics simulations performed here, it is important to account for the partial charges on atoms and the resulting contributions to the forces between interacting pairs. The methods for handling atomic charge calculations in the PCFF and ReaxFF force fields are very different from one another. In PCFF, atomic charges are initially assigned and remain the same throughout the simulation, while the charges in ReaxFF update periodically in order to adjust to any changes in bonding topology during the simulation. This fundamental difference in behavior between force fields results in different algorithms being applied to compute charge interactions in each force field.

For PCFF, the particle-particle–particle-mesh (PPPM) method [29] is used to computed the forces due to atomic charges. This method explicitly accounts for short-range forces within the r_c, and computes forces from an interpolation of charges on an effectively infinite grid for particles outside the the cutoff distance. The method works by writing the standard Coulomb term as

$$\sum_{i=1}^{N}\sum_{j>i}^{N}\frac{q_i q_j}{r_{ij}}\mathrm{erfc}\left(\frac{Gr_{ij}}{\sqrt{2}}\right) + \frac{1}{2}\int\int\frac{\hat{\rho}(r)\hat{\rho}(r')}{|r-r'|}\,dr dr' - \frac{G}{\sqrt{2\pi}}\sum_{i=1}^{N}q_i^2 \ . \tag{3.13}$$

In equation (3.13), The first term multiplies the standard charge potential by the complementary error function $\mathrm{erfc}(x)$, which goes nearly to zero after the cutoff distance r_c. This

accounts for the short range Coulomb forces. The constant G is determined by the cutoff distance r_c and the accuracy criterion for the method. The last term in equation (3.13) is a constant. The integral term accounts for the charges beyond the cutoff distance for the potential. The term is evaluated by discretizing the charge density $\hat{\rho}$ on a 3-d spatial grid. The charge grid is transformed to Fourier space and Poisson's equation is solved for the charge density $\rho(r)$ on the grid. Finally, the electric field and resulting atomic forces are computed from the result. LAMMPS uses a parallel algorithm with fast Fourier transforms to implement this method efficiently with computational cost scaling with $N\sqrt{\log(N)}$ [58]. The result is an efficient method which approximately accounts for the influence of charge over an effectively infinite domain; as such, the method can only be used when periodic boundary conditions are used for the simulation.

For ReaxFF, atomic charges change over time as bonding topology changes. To account for this, the QEq charge equilibration algorithm is used [60, 49]. The method is based upon enforcing the atomic charge potential χ_i of each atom i to be equal across all atoms, where

$$\chi_i(q_1, ..., q_N) = \chi_i^0 + J_{ii}^0 + \sum_{j \neq i} J_{ij} q_j \ . \tag{3.14}$$

In equation (3.14), q_i represents the charge on atom i, χ_i^0 and J_{ii}^0 are tabulated element-specific data, and J_{ij} is the Coulomb potential between atoms i and j. Equating charge potentials leads to $N-1$ equations

$$\chi_1 = \chi_2 = ... = \chi_N \ . \tag{3.15}$$

The sum of the charges must also equal the total system charge, such that

$$q_{tot} = \sum_{i=1}^{N} q_i \ . \tag{3.16}$$

The combination of equations (3.15) and (3.16) yields a system of N equations for the N unknown charges q_i. In LAMMPS, this system is solved using a parallel conjugate gradient algorithm.

3.3 Validation of PCFF and ReaxFF potentials for PPTA modeling

Validation of the choice of force field representing a particular material or molecule is always the first step in conducting MD studies. In this case, it is desired to use two different force fields: PCFF for the purpose of computing material properties and behavior at low to moderate strain/deformation conditions, and ReaxFF to model PPTA properties under more extreme conditions where primary bonds are likely to rupture. Also, given that the PCFF force field was designed specifically for molecules like PPTA, while the ReaxFF parameterization of Liu et al. [42] was not, some results from simulations using PCFF will be used as a benchmark against which to validate the performance of ReaxFF.

3.3.1 Simulation set-up in LAMMPS

For LAMMPS to begin a simulation, it must have knowledge of the initial atomic coordinates, any bond, angle, dihedral, and improper molecular topology, and all force field parameters. All simulations performed in this work deal with perfectly crystalline or nearly-crystalline ensembles of aligned PPTA chains. Initial molecular configurations are generated using Materials Studio [1], which contains the crystalline unit cell geometry and bonding topology of PPTA based on the X-ray diffraction measurements of Northolt [52]. This single unit cell can be replicated as desired in the x, y, and z directions to produce a simulation cell of multiple crystalline unit cells. Materials Studio can also be used to alter the molecular topology to simulate defects and other deviations from perfect crystallinity, as will be seen in some simulations. Materials Studio assigns the appropriate PCFF force field parameters to the PPTA molecule, and by using the packaged LAMMPS tool `msi2lmp`, Materials Studio `.mdf` and `.car` data files can be converted to LAMMPS data files containing PCFF force field parameters and all bond, angle, dihedral, and improper molecular topology. Appendix A.1 contains a sample data file for one unit cell of perfectly crystalline PPTA, as well as all the force field coefficients for PPTA formatted for input into LAMMPS.

ReaxFF data files are simpler to create, as only the atomic coordinates must be exported from Materials Studio. ReaxFF bonding topology is fully determined by the potential during each time step of the simulation. The ReaxFF parameters are taken directly from the LAMMPS-compatible ReaxFF parameterization file from the supplementary material of the paper by Liu et al. [42], which is reproduced in the Appendix A.2.

Both PCFF and ReaxFF have additional settings that must be specified that lie outside the scope of their respective parameterizations, namely, how to treat the calculation of long-range forces. For PCFF, the PPPM method described in Section 3.2.4 is used with relative force error tolerance of 1.0×10^{-4} for the solver. The Lennard-Jones coefficients for interactions between atoms of type i and j are determined using a mixing rule as follows:

$$\begin{aligned} \epsilon_{ij} &= \frac{2\sigma_i^3\sigma_j^3\sqrt{\epsilon_i\epsilon_j}}{\sigma_i^6+\sigma_j^6} \\ \sigma_{ij} &= \left(\frac{\sigma_i^6+\sigma_j^6}{2}\right)^{1/6}, \end{aligned} \tag{3.17}$$

where ϵ_i and σ_i are the Lennard-Jones parameters for atom i. The Lennard-Jones cutoff is set to 10.0 Å. A time step of $\Delta t = 1.0$ fs is found to be sufficiently small to maintain stable time integration.

In the ReaxFF potential, the charge on each atom changes dynamically as the simulation progresses to reflect any changes in bonding topology, and the QEq algoithm described in Section 3.2.4 is used to update atomic charges at every time step. A cutoff distance of 10.0 Å is used in the simulations, and a tolerance of 1.0×10^{-6} C is used for the charge equilibration. The time step used for all ReaxFF calculations is $\Delta t = 0.25$ fs. The implementation of the ReaxFF force field in LAMMPS is described [3].

3.3.2 Unit cell geometry

The ability to replicate basic molecule and crystalline unit cell geometry is an essential characteristic of any potential chosen to model PPTA. As such, the crystalline unit cell dimensions and molecular geometry of each force field under an unloaded, equilibrated state are computed and compared to literature. The X-ray diffraction measurements of Northolt [52] yield the crystalline unit cell dimensions as well as the atomic coordinates, bond lengths, and angles in the system. For the purpose of discussing relevant geometric features, Figure 3.2 provides a sketch of the monomer geometry, and identifies seven distinct bonds. These bond labels coincide with the 7 bond types in the PCFF force field parameterization.

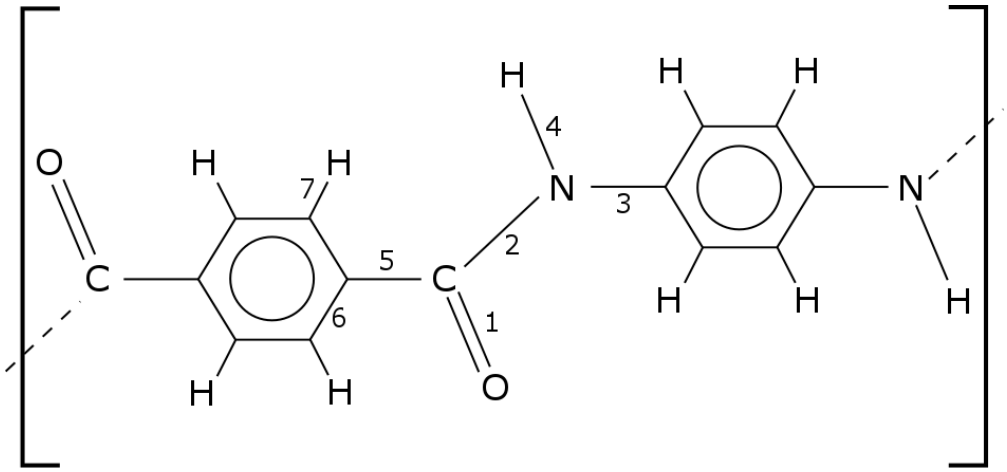

Figure 3.2: *Diagram of a single PPTA monomer.*

For both PCFF and ReaxFF, simulation cells consisting of 4x4x8 unit cells (in the x,y, and z directions, respectively) of perfectly crystalline PPTA were created. Periodic boundary conditions were used to represent bulk crystalline PPTA, and it should be noted that the use of PBCs in this case implies that the polymer chains are of infinite length. Before any measurements are taken, the system was first equilibrated. For each force field, the equilibration was carried out using a Nosé-Hoover barostat [55, 30] to create an NPT ensemble at a temperature of 300 K and zero pressure, representing unloaded PPTA at room temperature. A time constant of 100 fs was chosen for the temperature control, while a time constant of 1000 fs was chosen for the pressure control. The system was deemed equilibrated once the total system energy, temperature, pressure, and simulation cell dimensions ceased to change their values significantly in time.

After equilibrating the ensembles at 300 K, select geometric quantities of interest were time-averaged for 200 ps in each force field. Quantities measured include the simulation cell dimensions, bond lengths and angles, and aromatic ring orientations as represented by their time-averaged plane normal direction cosines. These time-averaged quantities are reported in Table 3.1, alongside the values measured by Northolt's X-ray diffraction experiments. The bond numbers reference the labeling in Figure 3.2, and the aromatic ring and link numbering

follows the diagram in Figure 3.3. As per convention, the hydrogen bond distance is given as the O–N distance between adjacent chains, where the atoms O–H–N form the hydrogen bond triplet. Angles 2–3 and 2–5 refer to the angles formed by bonds 2 and 3, and by bonds 2 and 5, respectively.

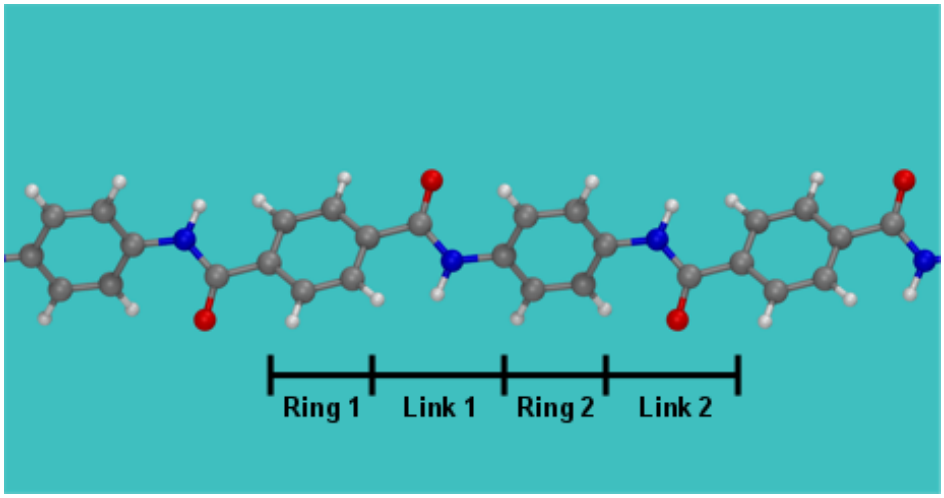

Figure 3.3: *Breakdown of a monomer into four major components, two aromatic rings and the three bonds consisting of the links between rings. C, H, O and N atoms are colored gray, white, red, and blue, respectively.*

Agreement between experiment and each potential is reasonable. PCFF is able to more closely replicate the experimentally measured crystalline unit cell dimensions. ReaxFF overestimates c while underestimating b. The smaller value of b in ReaxFF is consistent with the shorter hydrogen bond length computed with this force field, indicating that the hydrogen bonding forces are stronger in ReaxFF compared to PCFF. All covalent bond lengths in each force field are in good agreement with experimental results, with the exception of Bond 2 in ReaxFF, which is about 8% longer than the value in either PCFF or experiment. It is important to note that despite a few discrepancies in the details of molecule geometry, ReaxFF does predict the correct bonding topology for the molecule, a necessary condition for its use in modeling PPTA.

It is worth noting that a recently published MD study of PPTA [79] also employed the ReaxFF force field, but used the parameterization of Strachan et al. [69]. In the simulations conducted here, it was observed that running an equilibration simulation using the Strachan parameterization led to an inaccurate equilibrium crystal cell geometry. It was observed that the hydrogen bonds tended to engage with the chain diagonally adjacent in the unit cell, creating hydrogen bonds about 45° relative to the b direction of the unit cell, rather than rather than forming bonds between chains directly in the b direction. Hence, the hydrogen-bonded sheet geometry, a basic characteristic of crystalline PPTA molecular structure, could not be replicated with the Strachan parameterization. It was for this reason that the ReaxFF parameterization of Liu et al. [42] was chosen for for modeling PPTA in this work. The

	PCFF	ReaxFF	Northolt [52]
Unit cell dimensions (±0.01 Å)			
a	8.01	7.69	7.87
b	5.19	4.96	5.18
c	12.96	13.33	12.90
Bond length (±0.01 Å)			
Bond 1 length	1.21	1.30	1.23
Bond 2 length	1.37	1.44	1.34
Bond 3 length	1.44	1.44	1.42
Bond 4 length	1.00	1.10	1.00
Bond 5 length	1.50	1.50	1.47
Bond 6 length	1.40	1.39	1.39
Bond 7 length	1.10	1.12	1.00
Hydrogen bond (O–N)	3.10	2.78	3.30
Angles (±0.1 deg)			
Angle 2–3	124	124	125
Angle 2–5	111	123	117
Ring plane normal direction cosines ±0.001			
Ring 1 $\cos\theta_x$	0.839	0.819	0.819
Ring 1 $\cos\theta_y$	0.530	0.559	0.559
Ring 1 $\cos\theta_z$	0.139	0.122	0.122
Ring 2 $\cos\theta_x$	0.866	0.883	0.829
Ring 2 $\cos\theta_y$	0.438	0.469	0.530
Ring 2 $\cos\theta_z$	0.259	0.105	0.070
Cross-ring direction cosines ±0.001			
Ring 1 $\cos\theta_z$	0.956	0.974	0.966
Ring 2 $\cos\theta_z$	0.998	0.988	0.995

Table 3.1: *Equilibrium molecular geometry computed with PCFF and ReaxFF, compared to the X-ray diffraction measurements by Northolt [52]. The uncertainty labels in the left column headings refer to the standard error in the time averages for the measurements taken here with PCFF and ReaxFF.*

fact that the Liu parameterization was adapted from Strachan's and includes van der Waals correction terms to better predict crystalline polymer unit cells lends additional support to this choice of parameterization.

3.3.3 Calculation of elastic moduli

The ability of a potential to reproduce reasonable elastic moduli is a good indication that the force interactions between atoms are reasonably represented. Due to the symmetry of the PPTA unit cell, it is expected that the elastic moduli will have orthotropic symmetry, requiring nine independent constants to describe the elasticity of the material. For linear elasticity, the stress-strain relation is given by

$$\sigma_{ij} = C_{ijkl}\epsilon_{kl} \ , \tag{3.18}$$

where σ_{ij} represents the stress of linear elasticity theory, $\epsilon_{ij} = \frac{1}{2}\left(\frac{\partial u_i}{\partial x_j} + \frac{\partial u_j}{\partial x_i}\right)$ is the symmetric part of the deformation gradient, C_{ijkl} is the fourth-order elasticity tensor, and repeated indices imply summation. Due to the symmetry of the stress and strain tensors, this relation can be written more conveniently as

$$[\boldsymbol{\sigma}] = [\mathbf{C}][\boldsymbol{\epsilon}] \ , \tag{3.19}$$

where $[\boldsymbol{\sigma}] = [\sigma_{xx}\ \sigma_{yy}\ \sigma_{zz}\ \sigma_{xy}\ \sigma_{yz}\ \sigma_{xz}]^T$ and $[\boldsymbol{\epsilon}] = [\epsilon_{xx}\ \epsilon_{yy}\ \epsilon_{zz}\ 2\epsilon_{xy}\ 2\epsilon_{yz}\ 2\epsilon_{xz}]^T$, and $[\mathbf{C}]$ is represented as a symmetric 6x6 matrix.

It is desired to calculate the full set of elastic moduli for PPTA at room temperature, taken to be 300 K. A simulation cell of size 3×5×2 PPTA unit cells is used to perform the simulation for both PCFF and ReaxFF; these dimensions yield a roughly cube-shaped simulation cell. First, the cell is equilibrated at zero pressure with periodic boundary conditions, and the time-averaged cell dimensions at equilibrium are taken to be the reference configuration dimensions of the cell, denoted L_{x_0}, L_{y_0}, and L_{z_0}. The stress tensor in molecular dynamics is calculated according to equation (3.12), and the continuum-mechanical stress is computed by the time-average of this equation such that

$$\sigma_{ij} = \left\langle \sigma_{ij}^{MD} \right\rangle \ . \tag{3.20}$$

A reference stress $\boldsymbol{\sigma}^0$ is calculated by setting the simulation cell dimensions to L_{x_0}, L_{y_0}, and L_{z_0} and performing a time average of the stress in this unstrained state using an NVT time integration scheme. The components of the reference stress are found to be small and non-zero, which is attributed to small errors in the time-averaging of the equilibrium cell dimensions L_{x_0}, L_{y_0}, and L_{z_0}. When computing the elastic moduli components, the increase in stress relative to the equilibrium stress, $\Delta\boldsymbol{\sigma} = (\boldsymbol{\sigma} - \boldsymbol{\sigma}^0)$, is used.

Next, six separate simulations are performed, each of which applies one of the six possible strain deformations in $\boldsymbol{\epsilon}$ to the simulation cell. Figure 3.4 demonstrates how both normal

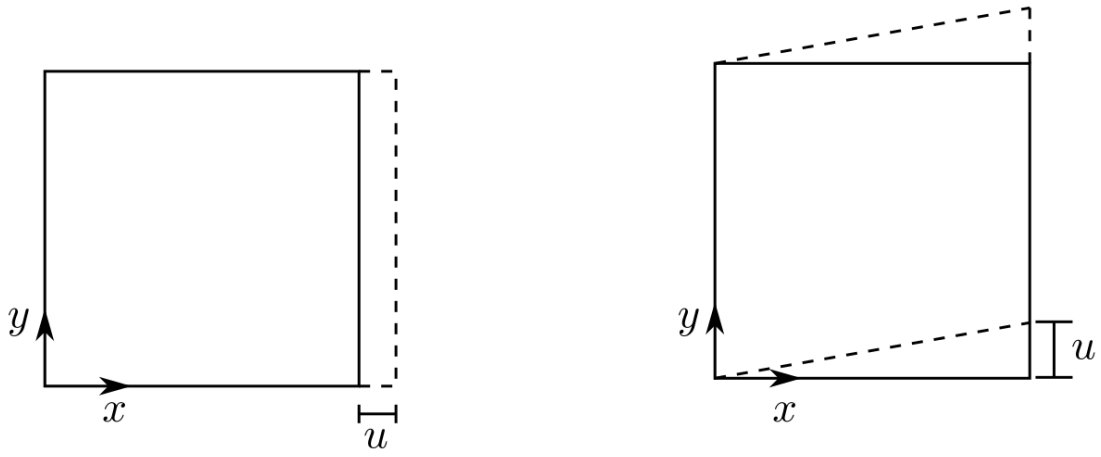

(a) *Normal strain* $\epsilon_{xx} = \dfrac{u}{L_{x_0}}$. **(b)** *Shear strain* $2\epsilon_{xy} = \dfrac{u}{L_{x_0}}$.

Figure 3.4: *Normal and shear strain deformations applied to the unit cell to compute elastic moduli. Calculations of strains* ϵ_{xx} *and* $2\epsilon_{xy}$ *are shown as an example.*

and shear strains are applied by deforming the simulation cell. Once the deformation is applied, the cell size is fixed, and an NVT thermostat is applied to maintain a temperature of 300 K. To compute the elastic moduli in each force field, each of the six deformation simulations was performed using a strain component value of $\epsilon = 0.004$ (in the case of shear strain, this would correspond to, for example, $2\epsilon_{xy} = \epsilon = 0.004$). This was deemed to be small enough to be within the infinitesimal strain approximation of linear elasticity theory, yet large enough that the fluctuations in stress deviated sufficiently from zero as to give meaningful time-averaged values. Time averaging was performed for a duration of 200 ps for both PCFF and ReaxFF. Each simulation at fixed applied strain yields one row of entries in the stiffness tensor $\mathbf{C}$, e.g. applying ϵ_{xx} gives $C_{11} = (\Delta\sigma_{xx})/\epsilon_{xx}$, $C_{12} = (\Delta\sigma_{yy})/\epsilon_{xx}$, etc. Therefore all six simulations combine to yield a 6×6 matrix of elastic constants. This matrix should be symmetric in theory, but due to the time averaging of the individual components, perfect symmetry is not achieved with the raw data. Similarly, components that ought to be zero due to orthotropic symmetry were computed to be close to zero, but not exactly zero. To remedy this, the entries that should be zero according to orthotropic symmetry were zeroed, and the symmetric part of the stiffness was taken as the true stiffness measure, that is,

$$[\mathbf{C}] = \frac{1}{2}\left([\mathbf{C}_{data}] + [\mathbf{C}_{data}^{T}]\right) \ . \tag{3.21}$$

An error estimate in the time averaged values was performed using a block averaging analysis [4] and it was determined that the error in each modulus component was approximately ±1 GPa.

The results of the simulations are presented in Table 3.2, alongside the results of two

previous MD studies of the elastic moduli of crystalline PPTA, one using the PCFF force field to compute the moduli at a temperature of 300 K [38], and the other using DREIDING to compute the moduli at 0 K [78]. The PCFF calculations performed here are comparable to the results obtained by [38], which serves as a sanity check that the simulation methodology used here is sound. There are some significant differences between values computed here using PCFF and ReaxFF, most notably in the C_{22} and C_{33} values, which are associated with the normal stiffness E_{yy} and E_{zz}, respectively. However, these stiffness values computed with DREIDING are actually quite comparable to ReaxFF, giving confidence that ReaxFF yields a reasonable model for PPTA. Experimental measurements for the crystalline elastic modulus E_{zz} have yielded estimates in the 200–260 GPa range [19, 5, 80], while theoretical estimates have placed this modulus in the 180–200 GPa range [74, 34]. It appears that all MD potentials list in Table 3.2 yield an overestimate of E_{zz} compared to theory and experiment. It is worth noting that both PCFF and ReaxFF are parameterized using data from quantum mechanical calculations, and such parameterizations are known to overestimate elastic moduli [6]. All of these points considered, the computed moduli here are deemed accurate enough to consider both PCFF and ReaxFF capable of reasonably representing the elasticity properties of crystalline PPTA.

Component	**PCFF (300 K)**	**ReaxFF (300 K)**	**Lit. PCFF [38] (300 K)**	**Lit. DREIDING [78] (0 K)**
C_{11}	11.9	15.9	11.9	15.3
C_{22}	23.6	91.9	32.2	82.3
C_{33}	293	324	284	338
C_{44}	3.9	2.7	6.1	5.2
C_{55}	9.1	8.4	14.3	15.4
C_{66}	0.2	0.9	0.5	0.7
C_{12}	11.3	15.6	11.1	5.6
C_{23}	7.0	32	14.2	9.6
C_{31}	9.3	10	10.5	4.4
E_{xx}	10.5	15.2	10.9	14.8
E_{yy}	20.9	87.5	29.5	80.1
E_{zz}	291	320	281	336

Table 3.2: *Elastic constants (units in GPa) computed using the PCFF and ReaxFF force fields in this thesis, alongside literature calculations. All values are computed at a temperature of 300 K, with the exception of the DREIDING force field values, which were computed at 0 K. The standard error in the time averaging of the elastic constants performed here is ±1 GPa.*

3.3.4 Molecular geometry change with axial stretch

Much of the work presented in this thesis concerns the simulation of tensile deformation of crystalline PPTA. There exists no experimental data on how bonds, angles, etc. within PPTA crystals change as the crystal is stretched, so a study was performed to compare how both PCFF and ReaxFF predict that deformation of the polymer chains will occur under tensile loading.

To perform the simulations, a series of equilibrations under different levels of strain are performed in order to track select geometric quantities of interest. Individual simulations are performed at unit cell strains between 0% and 7%, at increments of 1% strain. For each simulation, the unit cell is stretched to the desired strain value, and the select geometry features are time-averaged. Emphasis is placed on observing the mechanisms by which the PPTA chains accommodate stretching in each force field.

The deformation of the chain backbone bonds is plotted in Figures 3.5–3.7. Figure 3.5 shows how bond lengths change with monomer strain, and Figure 3.6 shows how bond strains change to highlight local bond stretch relative to their equilibrium lengths. One important takeaway from these figures is that Bond 2 is not subjected to significant stretching relative to the monomer stretch. This is particularly true for the ReaxFF potential, where Figure 3.6b highlights that Bond 2 essentially undergoes no change in length as the monomer is stretched. These observations can be explained by examining Figure 3.7, which shows the change in the direction cosine $\cos\theta_z$ in each bond versus monomer strain, where θ_z represents the bond's orientation relative to the fiber z axis. It can be seen that Bonds 3 and 5 begin relatively aligned with the z axis and remain so throughout as monomer strain is increased. However, $\cos\theta_z$ for Bond 2 increases with monomer strain, indicating that it becomes more closely aligned with the z axis as the monomer is stretched. As is evident from the monomer diagram in Figure 3.2, a rotation of Bond 2 to align with the z axis would increase the length of the monomer, though it need not induce a commensurate increase in the length of Bond 2. It is interesting to note that in PCFF, Bonds 3 and 5 stretch significantly more than in ReaxFF. However, both force fields accommodate a significant portion of the stretch through rotation (rather than stretching) of Bond 2.

In addition to looking at individual bonds, it is also of interest to look at the contributions of larger parts of the polymer chain to the monomer stretch. To study this, a single monomer is broken into four length segments as depicted in Figure 3.3. The segments consist of the span of the the two aromatic rings, as well as the span of the two "links" which connect the rings. Together, these four segments span the length of a single monomer, and the strain contributions of each as the monomer is stretched are plotted in Figure 3.8. From this figure, it is clear that the two potentials accommodate stretching of the monomer in different ways. In PCFF, Links 1 and 2 as well as Ring 1 make similar contributions to the total monomer strain, while Ring 2 stretches significantly less. In ReaxFF, the majority of the stretch is accommodated nearly equally by Rings 1 and 2, while Links 1 and 2 make a smaller contribution than in PCFF. Also, while not plotted here, the additional strain accommodated by the aromatic rings in ReaxFF is due to the bending of the angles within

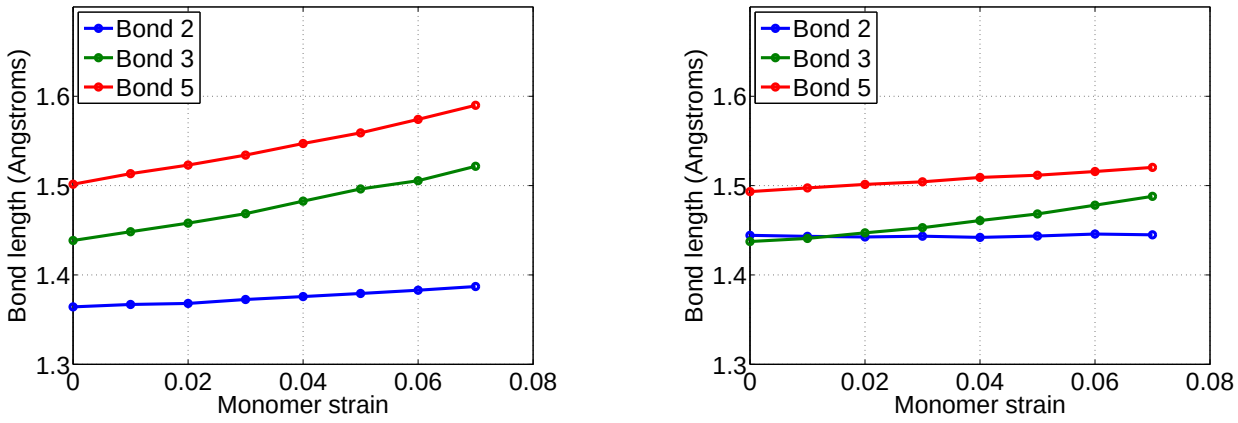

(a) *PCFF* **(b)** *ReaxFF*

Figure 3.5: *Bond length versus monomer strain*

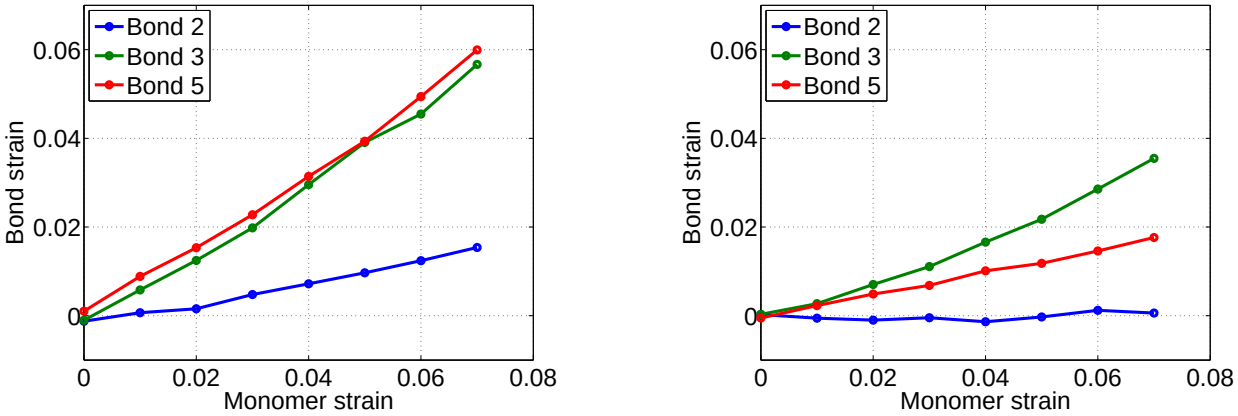

(a) *PCFF* **(b)** *ReaxFF*

Figure 3.6: *Bond strain versus monomer strain*

each ring, which allows the span of the rings to increase without significantly increasing the length of the bonds within the rings.

These results show both similarities and differences in the deformation of a PPTA chain when modeling with PCFF and ReaxFF. Both force fields predict that Bond 2 rotates rather than stretches to accommodate the monomer stretch. The major difference between force fields is in how bond angles change, with ReaxFF exhibiting more flexible angle changes as evidenced by Bond 2 essentially not changing its length, and by the aromatic ring span increasing more significantly than in PCFF. This is likely due to how ReaxFF works, as the forces contributed by the angle terms tend towards zero as the bond order decreases; PCFF, on the other hand, models the angles as nonlinear springs with finite stiffness at any level of deformation. Ultimately, the force fields behave reasonably, and ReaxFF behaves similar

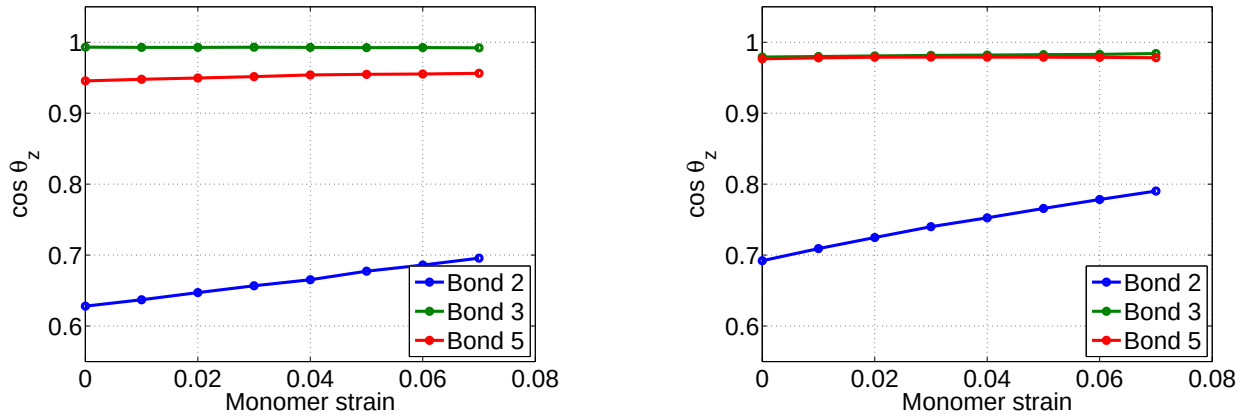

(a) *PCFF* (b) *ReaxFF*

Figure 3.7: *Angle orientation as denoted by direction cosine θ_z*

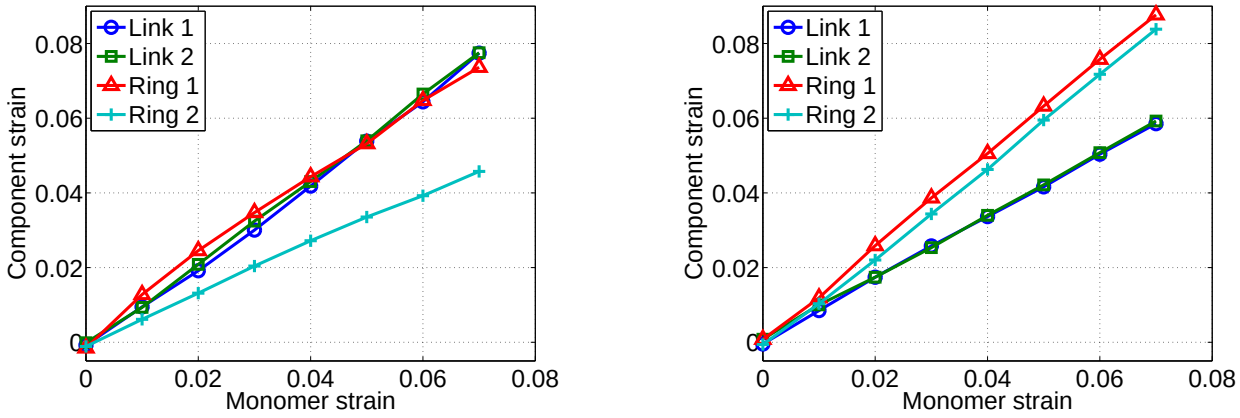

(a) *PCFF* (b) *ReaxFF*

Figure 3.8: *Strain in the two links and two rings consisting a single monomer, versus monomer strain. Component labels follow those in Figure 3.3.*

enough to PCFF during the deformation process that there is no alarm or lack of confidence in using it to model crystalline PPTA at moderate to high strains.

Chapter 4

Constant strain rate loading simulations of crystalline PPTA

PPTA fibers are most commonly used in applications involving tensile loading along the fiber axis. When used in ballistic fabrics, the fibers may be subjected to high rates of loading, and, as discussed in Chapter 2, some experimental results have suggested that fiber modulus and/or failure behavior depend on the rate of loading. As such, molecular dynamics simulations performed using constant strain rate loading elucidate the molecular-level response to strain rate loading, thus leading to improved understanding of the microstructural mechanisms driving the macroscopic fiber response.

In this chapter, the effects of strain rate and temperature on the mechanical behavior of both perfect and defective crystals are studied. The ReaxFF force field is used as the primary tool to model PPTA molecules in order to capture primary bond rupture that occurs during crystal failure. Simulations are also performed with PCFF to compare its response to ReaxFF. However, results obtained using PCFF are only applicable to cases in which primary bonds are not expected to break under the applied loading.

4.1 Mechanical response of perfectly crystalline PPTA under constant strain rate loading

To explore the influence of loading rate on the mechanical behavior of crystalline PPTA, constant strain rate molecular dynamics simulations are performed. All simulations begin by equilibrating the system at the desired temperature, resulting in equilibrated simulation cell lengths L_{x_0}, L_{y_0}, and L_{z_0}. Next, the simulation cell is stretched in the z direction by applying a constant velocity $v = \dot{\epsilon}_{zz} L_{z_0}$ to one end of the cell while holding the other end fixed, which is consistent with applying a constant engineering strain rate $\dot{\epsilon}_{zz}$ to the system. An NPT barostat as described by the equations of motion (3.10) is applied to the simulation box to maintain the desired temperature and zero time-averaged normal stresses on the lateral simulation cell faces. The method used here for applying constant strain rate in MD is very

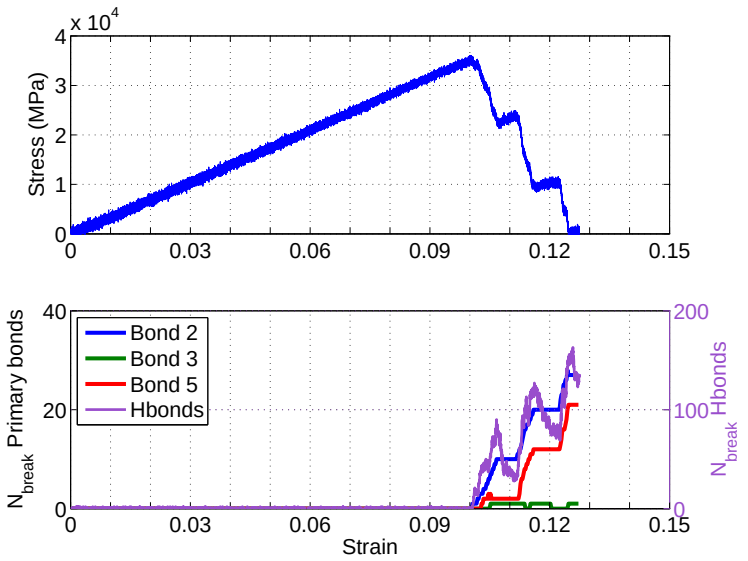

Figure 4.1: *Stress-strain curve and bond break history for the 4×4×8 unit cell system at* $\dot{\epsilon}_{zz} = 1.0 \times 10^9\ s^{-1}$.

similar to that employed by Hossain et al. [31] to conduct constant strain rate simulations of amorphous polyethylene in LAMMPS.

By way of introducing the simulations and the resulting crystal behavior, the result of applying a constant strain rate of 1.0×10^9 s^{-1} is presented in Figure 4.1. The simulation was performed with the ReaxFF force field on a perfectly crystalline system (infinitely long chains with no defects) of 4×4×8 unit cells using periodic boundary conditions. The use of ReaxFF allows for breakage of primary bonds. Figure 4.1 presents a plot of the stress σ_{zz} (calculated according to equation (3.12)) versus engineering strain ϵ_{zz} for the crystal, as well as a plot of the number of primary bond ruptures (bonds of types 2, 3, and 5 along the backbone of the polymer chain, as diagrammed in Figure 3.2) and secondary hydrogen bond ruptures versus strain. In ReaxFF, bonds never truly rupture, in the sense that there is always a non-zero bond order between atoms within the cutoff distance of the force field. However, a low bond order is a good indication that a bond is weak enough to be considered failed. For example, Chenoweth et al. indicate bond failure when the bond order reaches 0.2 [10]. Here, it was found that a bond order of 0.3 was a good indication of failure of the primary backbone bonds. Note that this value does not influence the system trajectory, but is used as a book-keeping tool to keep track of the number of bond failures in the system. Hydrogen bonds behave in a similar manner, with interactions present until the hydrogen-bonded atoms are separated by a distance greater than the force field cutoff distance. Hydrogen bond criteria often employ potential energy or geometry-based conditions to determine whether a hydrogen bond exists or not [46, 43, 8]. Here, a geometry-based criteria is used as diagrammed in Figure 4.2, and a hydrogen bond is taken to exist if the bond length $d_{hb} < 3.5$ Å and the bond angle $\theta_{hb} < 120°$.

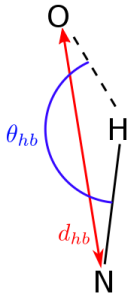

Figure 4.2: *Diagram of a hydrogen bond in PPTA, highlighting the bond length d_{hb} and bond angle θ_{hb}.*

In Figure 4.1, the stress-strain curve undergoes a slight non-linearity after exceeding about 0.6–0.7% strain, transitioning from a modulus E_{zz} of 320 GPa to 355 GPa. The slight nonlinearity in stress-strain response can be attributed to the nonlinear change in molecular bond length and other geometrical features of the crystal cell as discussed in Section 3.3.4. After the initial increase in modulus, the modulus remains constant up until primary bonds begin to break, at which point the stress begins to drop. In the strain-to-failure simulations performed in this work, system failure is defined as the point at which the maximum stress is attained, and the strain commensurate with this stress level is called the failure strain, denoted ϵ_f. After the onset of failure, the stress response undergoes a "stair-step" pattern, until it reaches a zero stress value, indicating complete failure of the system. By examining the plot of bond breaks versus strain, it can be seen that the rises in stress in the post-failure regime correspond to portions of the loading in which no primary backbone bonds rupture; hydrogen bonds also appear to heal and re-engage during these periods. This phenomenon can be better explained by examining Figure 4.3, which displays the same stress-strain plot as Figure 4.1, but replaces the bond break plot with a plot of broken backbone bonds organized by *sheet*. Here, a sheet refers to a collection of hydrogen-bonded chains that reside in a common y–z plane of the crystal. There are two monomers per unit cell, so in the 4×4×8 unit cell system, there are a total of 8 sheets present in the simulation cell. Upon examining Figure 4.3, it is clear that each of the three drops in stress in the post-failure regime correspond to a group of sheets failing at roughly the same time: the first group of failures consists of Sheets 2, 6, and 8, the second group of Sheets 3, 4, and 5, and the third group of sheets 7 and 1. After all sheets have failed, the system stress drops to zero, and the system can no longer support any load.

An important aspect of these simulations is the stochastic nature of the failure strain. Figure 4.4 displays the stress-strain curves of five different strain rate runs of the same 4×4×8 unit cell system. Each of the five runs is performed at a strain rate of 1.0×10^9 s^{-1}, but begins from a slightly different equilibrium configuration, representing a slight perturbation in initial conditions. As Figure 4.4 shows, the failure strain for each run is different, an

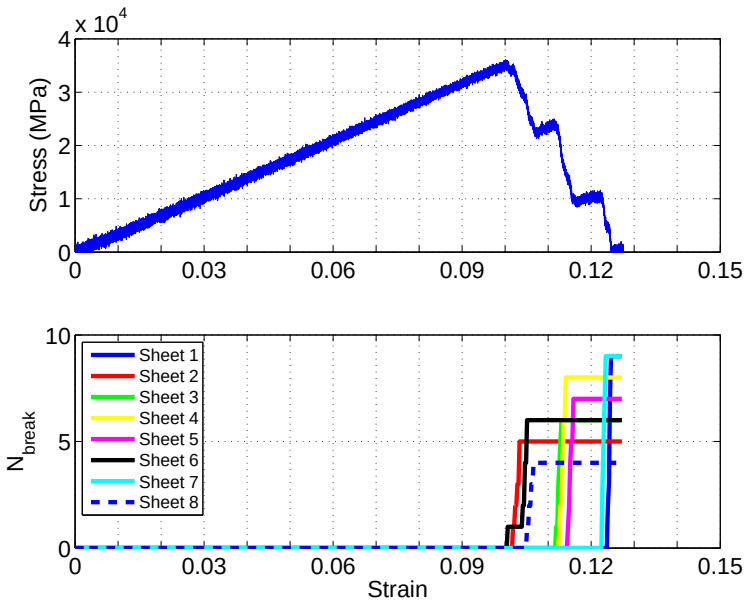

Figure 4.3: *The stress-strain and bond break history plot from Figure 4.1 for the 4×4×8 unit cell system is reproduced, but bond breaks are organized by hydrogen-bonded sheet. There is a clear correlation between the drops in stress in the post-failure regime of the stress-strain curve and the rupture of each individual sheet.*

indication that the onset of failure is stochastic in nature.

With the fundamental stress-strain response of perfectly crystalline PPTA at a single strain rate presented, it is now of interest to explore the effect that that changing the strain rate has on the system response. Using the same 4×4×8 unit cell system from five different equilibrated states, simulations applying strain rates of 5.0×10^9 s^{-1}, 1.0×10^9 s^{-1}, 2.0×10^8 s^{-1}, 4.0×10^7 s^{-1}, and 8.0×10^6 s^{-1} are performed, a total of 25 independent simulations. Figure 4.5 displays the results, from which several important observations are made. First is that the behavior before the onset of failure is identical for each strain rate: the behavior is nearly linearly elastic before failure, and the modulus of the system is independent of the applied strain rate. However, the failure strain does depend on the strain rate. The apparent trend is that an increase in strain rate leads to an increase in failure strain, which is clearly demonstrated in Figure 4.7. The plot suggests that failure strain increases roughly linearly with log strain rate.

The bond rupture behavior of the simulations is key to understanding failure of the crystal. In addition to the introductory simulation results presented in Figure 4.1, Figure 4.6 presents the stress-strain and accompanying bond rupture behavior at slower strain rates of 2.0×10^8 s^{-1} and4.0×10^7 s^{-1}. In all of these simulations, a substantial number of Type 2 bonds rupture before any other primary bonds, with all other primary bond ruptures occurring well after the onset of failure in the crystal. Hydrogen bond breaks occur nearly simultaneously with the Type 2 bond breaks, and are the result of newly broken chains being

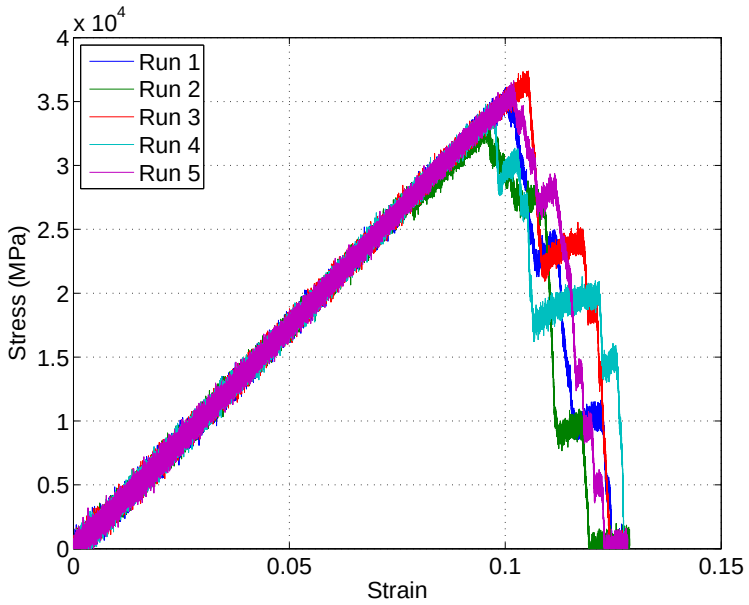

Figure 4.4: *Simulation at strain rate* $\dot{\epsilon} = 1.0 \times 10^9\ s^{-1}$ *for five different equilibrated starting points of the 4×4×8 unit cell system. The difference in failure strain between runs highlights the stochastic nature of the failure response.*

able to slide past and separate from one another due to the rupture of the Type 2 bonds along the chain backbone. From these results, it can be concluded that Type 2 bonds are weakest of the primary bonds along the chain backbone, and therefore govern the failure of the chains and subsequent failure of the crystal. It is interesting to note that the results of Section 3.3.4 show that Type 2 bonds in the ReaxFF force field undergo hardly any stretch with increasing crystal strain, and instead rotate in the direction of the fiber axis in order to accommodate stretching within the polymer chains. Despite a tendency to rotate rather than stretch as the crystal strain is increased, these bonds still represent the weakest link in the PPTA chain backbone, and govern the failure behavior of the system.

At this point it is important to emphasize that these constant strain rate simulations become prohibitively costly to perform at "slow" strain rates. This is particularly problematic for ReaxFF, which is known to be much more expensive than standard classical MD potentials, and which performed about 10 times slower (in terms of wall-clock time per simulation time step) than PCFF in the simulations performed in this work. This difference is further exacerbated due to ReaxFF requiring a smaller time step of 0.25 fs (as opposed to 1.0 fs for PCFF) to maintain stable time integration. Constant strain rate simulations are required to run for sufficient time to reach the relatively high strains at which system failure occurs, and the number of time steps required to advance a simulation to a given strain is inversely proportional to the applied strain rate. As a point of reference, performing a strain-to-failure simulation on the 4×4×8 unit cell system (7,168 atoms) using 64 processors (peak speed of each processor rated at 431 TFLOPS/sec) at a strain rate of $1.0 \times 10^9\ s^{-1}$ requires

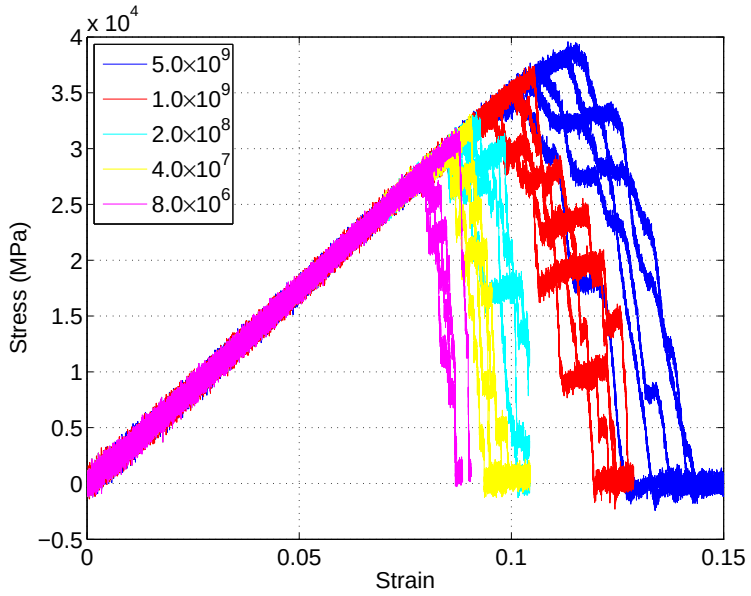

Figure 4.5: *Stress-strain curves for the 4×4×8 unit cell system at five different strain rates. Five different equilibrated starting points are used for each rate.*

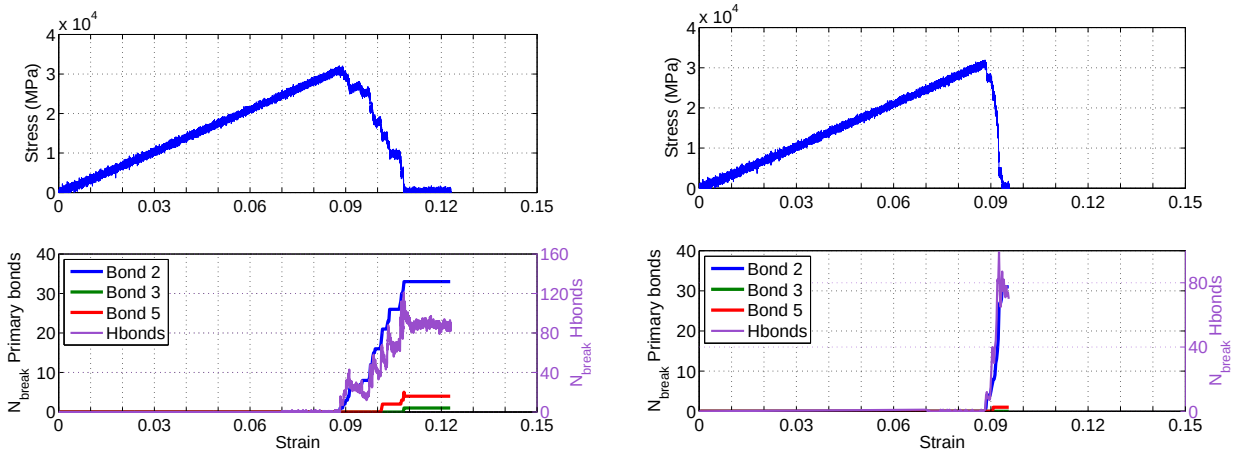

(a) $\dot{\epsilon} = 2.0 \times 10^8\ s^{-1}$ **(b)** $\dot{\epsilon} = 4.0 \times 10^7\ s^{-1}$

Figure 4.6: *Stress-strain response and bond break history for two different strain rates of the 4×4×8 unit cell system.*

a wall-clock time of about 16 hours. Hence, a simulation at a rate of 1.0×10^8 s^{-1} would take 160 hours, and it becomes evident that simulating rates much lower than this becomes prohibitively expensive. Simulating strain rates observed in typical engineering applications of aramid fibers, such as ballistic impact events where strain rates are in the neighborhood of 100–1,000 s^{-1} [26] is, therefore, wholly impractical.

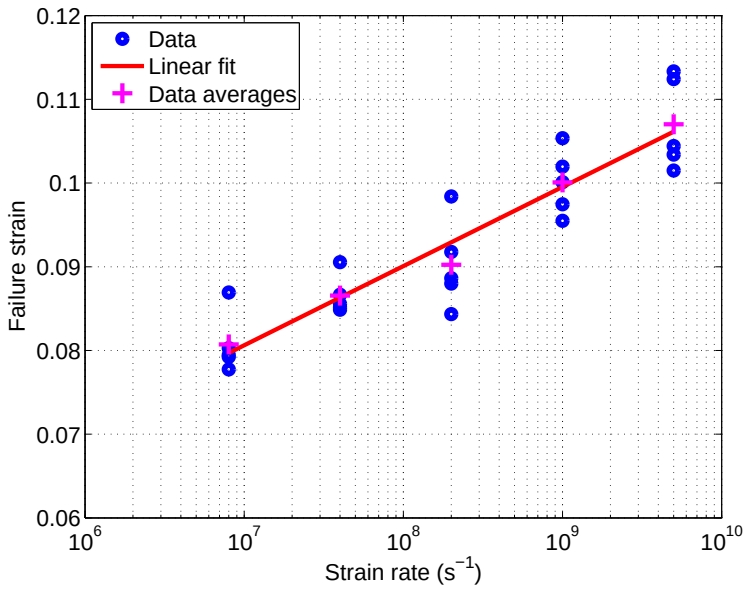

Figure 4.7: *Failure strain versus strain rate for the 4×4×8 unit cell system.*

After performing simulations at several different strain rates, it became evident that the response of the crystal is history-independent and reversible up until the moment the first primary bond fails, as the system does not undergo any chemical or fundamental geometry changes (e.g. inter-chain slippage) until this moment. Additionally, the only strain rate dependent property of the system is the failure strain. Due to this very specific behavior, it is possible to begin a strain rate simulation from a non-zero strain and obtain the same system behavior as beginning from zero strain, as long as bonds do not rupture at the starting strain during the process of loading at the desired rate. Leveraging this fact, all strain rate simulations were performed by first pre-straining the system to a level of 7%, which was deemed a sufficiently low strain such that bond ruptures would never be observed for the strain rates simulated in this work. The system was equilibrated at this starting point, and then the desired strain rate was applied to compute the constant strain rate response. Using this method, it was possible to perform a strain-to-failure simulation of a 4×4×8 unit cell system with about 160 hours of wall-clock simulation time.

In addition to strain rate, it was observed that the size of the simulation cell was another factor which influenced the failure strain. By way of example, a large system of 8×8×64 unit cells is strained using strain rates of 5.0×10^9 s^{-1} and 1.0×10^9 s^{-1}. The results are plotted in Figure 4.8 together with simulations at the same rate but using the 4×4×8 unit cell system. In each case, the larger system fails earlier than the smaller system. This size effect can be rationalized by considering that the onset of failure is essentially the onset of a flaw in the material, in this case, the rupture of a primary bond in the system. When modeling a larger system, there is a greater number of uniquely-represented bonds that may fail, and as such, the larger system will on average fail more quickly than a corresponding smaller system with

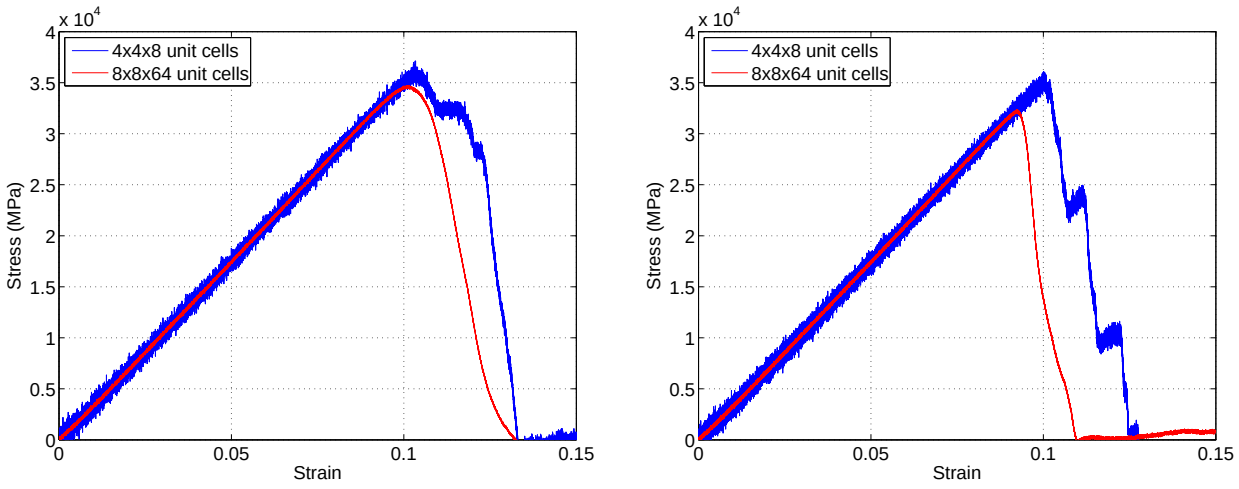

(a) $\dot{\epsilon} = 5.0 \times 10^9\ s^{-1}$ **(b)** $\dot{\epsilon} = 1.0 \times 10^9\ s^{-1}$

Figure 4.8: *Stress-strain curves for the 4×4×8 and 8×8×64 unit cell systems, highlighting the lower failure strain for larger systems.*

fewer potential sites for failure. Such a size effect is seen in many engineering materials, where a larger sample of material increases the probability of the existence of some critical flaw or defect, and as such, a larger sample of material is likely to exhibit decreased strength compared to a smaller sample of the same material.

Finally, another important aspect to consider is the influence of temperature on the mechanical behavior. So far, all simulations have been performed at a temperature of 300 K. In Figure 4.9, the stress-strain curves of simulations performed at a strain rate of 1.0×10^9 s^{-1} and temperatures of 300 K, 400 K, and 500K are presented. In each case, the stress response is nearly linearly elastic up until failure, with the failure strain decreasing substantially with an increase in temperature. The modulus of the material also decreases with an increase in temperature, taking values of 320, 309, and 293 GPa (at strains below 1%) at temperatures of 300 K, 400 K, and 500 K, respectively. The same set of strain rate simulations as depicted in Figure 4.5 (with the exception of $\dot{\epsilon} = 8.0 \times 10^6$ s^{-1}, due to its high computational cost) was performed at temperatures of 400 K and 500 K, and Figure 4.10 shows that the roughly linear relationship between failure strain and log strain rate holds across all temperatures examined. The figure also highlights the decrease in failure strain with an increase in temperature. As in the case of constant strain rate loading at 300 K, the mechanical response is nearly linearly elastic up to failure, and the strain rate does not influence the stiffness response for any temperature studied here.

4.1.1 Discussion of simulation results

The simulations conducted so far have shown that system failure is governed by the failure of individual Type 2 primary bonds along the backbone of PPTA chains in the crystal,

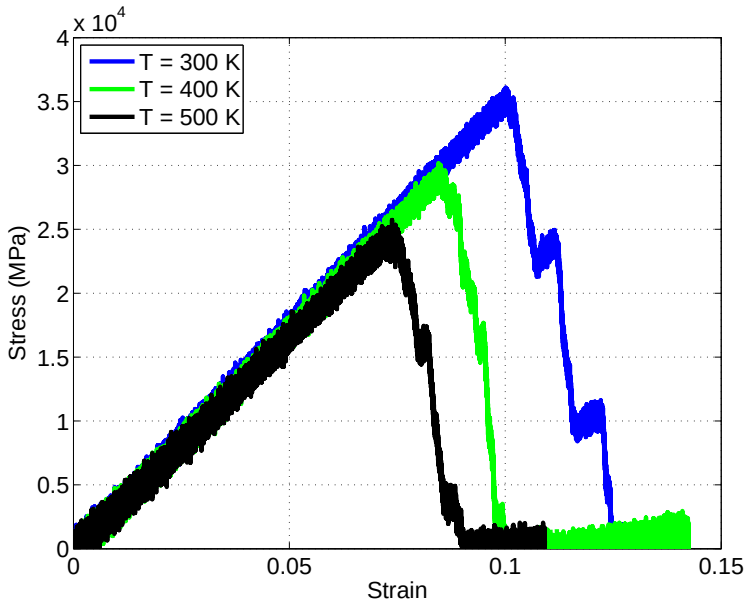

Figure 4.9: *Stress-strain curves for the 4×4×8 perfect crystal model at a strain rate of* $\dot{\epsilon} = 1.0 \times 10^9\ s^{-1}$ *and temperatures of 300 K, 400 K, and 500 K.*

and that the system failure strain has a strong dependence on strain rate, temperature, and system size. Specifically, it is observed that failure strain increases with increasing strain rate, decreases with increasing temperature, and decreases with increasing system size. These observations are remarkably consistent with the fundamental tenets of the the kinetic theory of fracture [75], which examines material failure by thermally activated bond ruptures accumulated over time. The theory has been shown to be applicable to predicting creep lifetimes of a variety of metallic and polymeric solids [82, 33]. According to the theory, thermal fluctuations in atomic bond oscillations act as instigators of fracture events – as bonds oscillate about their mean value at a finite temperature, each oscillation is an opportunity for the bond to rupture, and the probability of rupture is determined by the temperature and loading conditions of the solid. The relationship found experimentally by Zhurkhov et al. [82] is

$$t_f = t_0 \exp\left[\frac{U_0 - \gamma\sigma}{k_b T}\right] , \tag{4.1}$$

where t_f is the mean time to failure of a sample of material, σ is the stress on the sample, T is the temperature, k_b is the Boltzmann constant, and t_0, U_0, and γ are material constants. The material constants are typically given physical interpretations as follows: t_0 represents the period of oscillation of atomic bonds in the system, U_0 represents the activation energy required for fracture, and γ is a material-dependent parameter which is adjusted to fit data

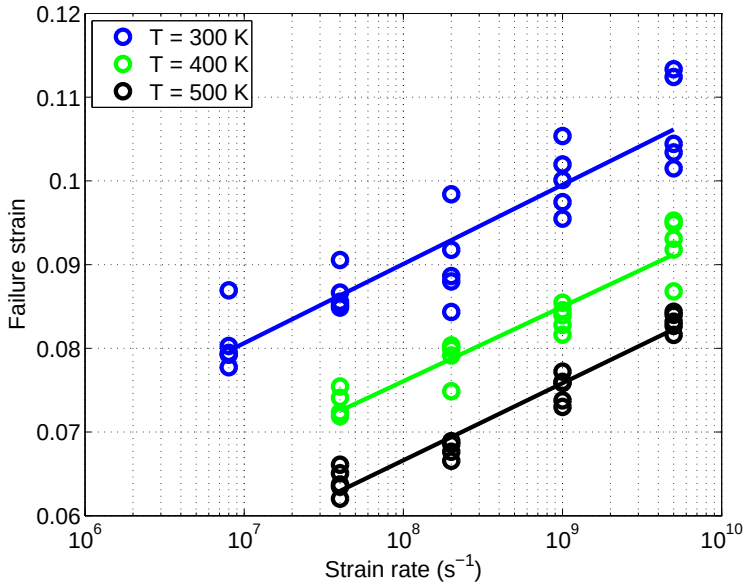

Figure 4.10: *Failure strain versus strain rate for the 4×4×8 perfect crystal model at temperatures of 300 K, 400 K, and 500 K.*

for a particular sample. The equation can also be inverted and expressed as [83]

$$\lambda = \omega_0 \exp\left[\frac{-U_0 + \gamma\sigma}{k_b T}\right] , \tag{4.2}$$

where $\lambda = \dfrac{1}{t_f}$ is the rate of failure of chemical bonds in the solid, and ω_0 represents their frequency of oscillation. It should be noted that equations (4.1) and (4.2) are often applied to experimental data for a solid (e.g. mean time to failure of a stressed sample), in which case the activation energy U_0 is that of the entire solid. However, t_f, λ, and U_0 can also apply to the individual bonds themselves. From equation (4.2), it can be seen that increasing the stress on the system lowers the effective activation energy, leading to a higher failure rate. Similarly, increasing the temperature of the system also leads to an increase in failure rate. An increase in temperature can be attributed as an increase in the magnitude of the thermal fluctuations of atomic bonds, and hence leads to an increase in the probability of a bond rupture occurring per oscillation.

As originally developed, the kinetic theory of fracture pertains to materials under constant load which fail via creep. However, it can also be extended to materials under time-dependent loading. Hansen and Baker-Jarvis [28] developed a rate-dependent kinetic theory of fracture based on sub-microcrack formation, and were able to derive the following expression for the failure stress under constant stress rate loading:

$$\sigma_f = \frac{k_b T}{\gamma}\left[\ln\dot{\sigma} + \ln\left(\frac{t_0\gamma}{k_b T}\right) + \frac{U_0}{k_b T}\right] . \tag{4.3}$$

For the special case where the behavior is linearly elastic until failure, which closely approximates the behavior of PPTA crystals studied in this work, the stress can be written as $\sigma = E\epsilon$. If the rate of loading is constant, then $\epsilon = \dot{\epsilon}t$, $\dot{\sigma} = E\dot{\epsilon}$, and equation (4.3) can be written as

$$\epsilon_f = \frac{1}{E}\frac{k_bT}{\gamma}\left[\ln\dot{\epsilon} + \ln\left(\frac{t_0\gamma E}{k_bT}\right) + \frac{U_0}{k_bT}\right] . \tag{4.4}$$

Based on equation (4.4), if temperature is fixed, then for a given material, the failure strain ϵ_f can be thought of as a function of strain rate, such that

$$\epsilon_f = A\ln\dot{\epsilon} + B , \tag{4.5}$$

that is, the failure strain has a linear relation with log-strain rate, where the constants A and B would change with temperature or material properties. This is essentially the relationship found in the MD simulations performed here, as exhibited by Figure 4.10. It is noted that care should be taken in relating these theoretical results to the MD simulation data, since the derivation of equation (4.3) involves assumptions regarding continuum-level material failure via crack development, while the MD results pertain to failure strain (as defined by peak stress) in a polymer crystal. However, the relationship does offer further evidence that the failure mechanism in the MD simulation of PPTA crystals is governed by thermally activated bond failures, as postulated in the kinetic theory of fracture.

4.2 The influence of structural defects on the mechanical response of PPTA crystals

As discussed in Chapter 2, it is well known that the microstructure of PPTA fibers like Kevlar and Twaron exhibit a number of structural defects. Grujicic et al. [20, 21, 22, 24, 23, 25] performed an extensive MD study on the influence of defects of varying complexity on the mechanical properties of PPTA. For the sake of simplicity, the only type of defects considered in this study are chain-end defects in otherwise perfectly crystalline PPTA. This, of course, is a much more realistic model than the infinite-chain models considered thus far. While chain-end defects are relatively simple in nature compared to the types of defects considered in the work of Grujicic et al., they are one of the most fundamental and prominent types of defects present in true PPTA fibers. As discussed in 2, chain-end defects are believed to be randomly distributed in the fiber skin, but clustered in periodic defect bands within the fiber core. In this work, MD models are created which attempt to mimic these types of defect patterns, with the goal of using MD simulations to predict and understand the resulting mechanical behavior of the defective PPTA crystal. In all models considered here, chain-ends are introduced into a perfectly crystalline system by eliminating the backbone bonds linking two aromatic rings together (the "link" as diagrammed in Figure 3.3), and capping the aromatic rings with hydrogen atoms, as demonstrated in Figure 4.11.

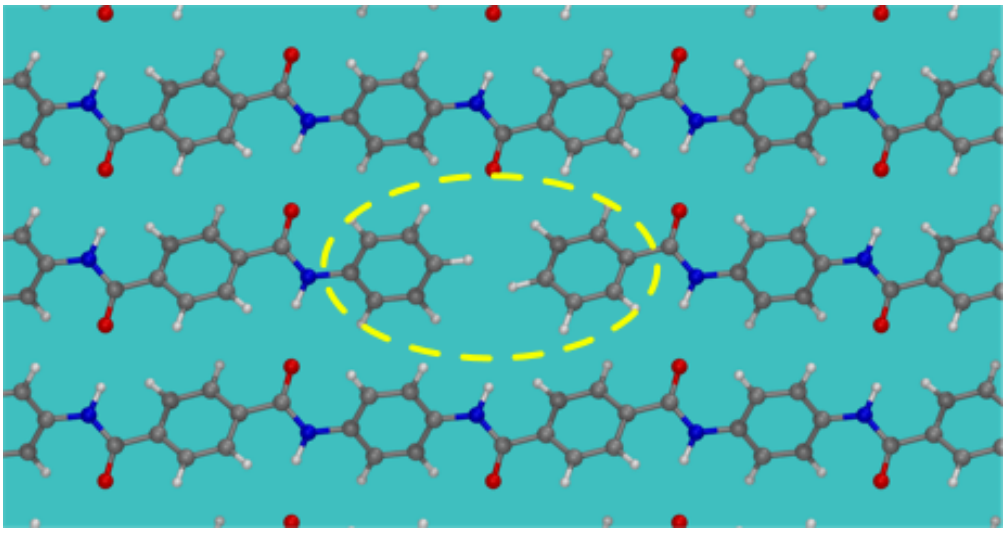

Figure 4.11: *A chain-end defect is introduced by removing the bonds linking two aromatic rings, and capping the rings with hydrogen atoms.*

4.2.1 The zone of influence of chain-end defects

In order to better understand how defects affect the behavior of PPTA crystals a as a whole, a study is conducted to understand how defects affect the local behavior of the nearby chains. It is expected that a single defect will cause some load transfer from the broken chain to adjacent surrounding chains, resulting in stress relaxation in the broken chain and stress concentration in adjacent chains near the defect site. The geometric region in which chains will deviate from nominal behavior will be of finite size, and the volume covered by this region will be referred to as the "zone of influence" of a single defect. The goal of the study is to determine the size of this zone of influence, and how it affects the behavior of neighboring chains.

To perform the study, a model of 4×8×32 unit cells is used. (The reason for choosing this system size will become evident as the results of the study are presented). A single chain break is introduced into the center of this system, while all other chains remain intact, and of effective infinite length due to the use of periodic boundary conditions. To observe the zone of influence, a strain ϵ_{zz} is applied to the system, and while the system is held fixed at this constant strain, an NPT barostat is used to maintain zero pressure on the lateral sides of the simulation cell, and a constant temperature of 300 K. Under these conditions, the geometric configuration is averaged in time, and the resulting time-averaged structural features are analyzed.

The structural feature that is chosen as the indicator of local chain deformation is the "link" portion of the chains in the system, with a link referring to the linkage of Bonds 2, 3, and 5 in between aromatic rings, as diagrammed in Figure 3.3. As shown in Figure 3.8, this quantity changes roughly linearly with an increase in monomer strain, and any deviations

from the relationship in Figure 3.8 are indicative of local stress concentrations or relaxations along the chain backbone. In order to determine if these deviations change with the amount of applied strain, this study is performed on systems strained to 2%, 4%, and 6%, and both the PCFF and ReaxFF force fields are examined to see how they behave relative to one another.

Through a trial-and-error procedure, it was determined that the zone of influence of a single defect is constrained to no more than ±8 monomers away from the defect along the broken chain, and the in-sheet chains directly adjacent to the broken chain. Chains within adjacent sheets are completely unaffected by the defect. These observations led to a choice of a 4×8×32 unit cell system to perform the full suite of simulations. The 8 and 32 cells in the y and z directions, respectively, ensure that there are unaffected links within the system, outside of the zone of influence of the defect. The 4 unit cells used for the x direction ensures a simulation box length $L_x > 2r_c = 20$ Å, where r_c is the cutoff interaction length for non-bonded interactions, as discussed in Section 3.2.

The results of the study for both the PCFF and ReaxFF force fields are summarized in Figure 4.12. It was found that only the broken chain and two nearest adjacent chains were affected by the chain-end defect, with all other links in the system remaining at the nominal strain – as such, only the response of the three chains influenced by the defect are displayed in Figure 4.12. Both the PCFF and ReaxFF force fields predict very similar chain behavior. The broken chain experiences a region of relaxation along the chain, roughly ±8 monomers away from the defect site in both PCFF and ReaxFF, after which the link strain returns to the nominal strain. In the adjacent chains, there is an increase in the link strain near the defect, with the strained region spanning approximately ±4 monomers for both force fields. The response of the two adjacent chains differ from one another in each force field. This asymmetry can be explained by observing the details of the geometry as depicted in Figure 4.11. In the chain above the defect, the oxygen atom extending from the link is the atom closest to the defect, whereas in the chain below the defect, the hydrogen atom extending from the link is nearest the defect. Hence, there is a geometrical asymmetry that is responsible for the difference in the response in the two adjacent chains.

In addition the the change in link strain, the change in hydrogen bond stretch near the defect site is also examined, and the results are displayed in Figure 4.13. For the case of hydrogen bonds, it was found that only hydrogen bonds attached to the broken chain experienced detectable deviations from the nominal hydrogen bond stretch in the crystal. There are therefore two rows of bonds whose response is displayed, which are bonds between the broken chain and the chains located ±1 y-monomer adjacent to the broken chain. The hydrogen bonds take on additional stretch in a region about ±8 monomers along the length of the chain, which is commensurate with the size of the relaxed region of the broken chain. It is also observed that the hydrogen bonds increase their stretch relative to the other hydrogen bonds in the system as the crystal strain increases. The change in length of the hydrogen bonds near the defect can be explained by examining Figure 4.14, which displays the molecular configuration near the defect site at 2%, 4%, and 6% crystal strain. From the figure, it can be observed that the hydrogen bonds near the broken chain

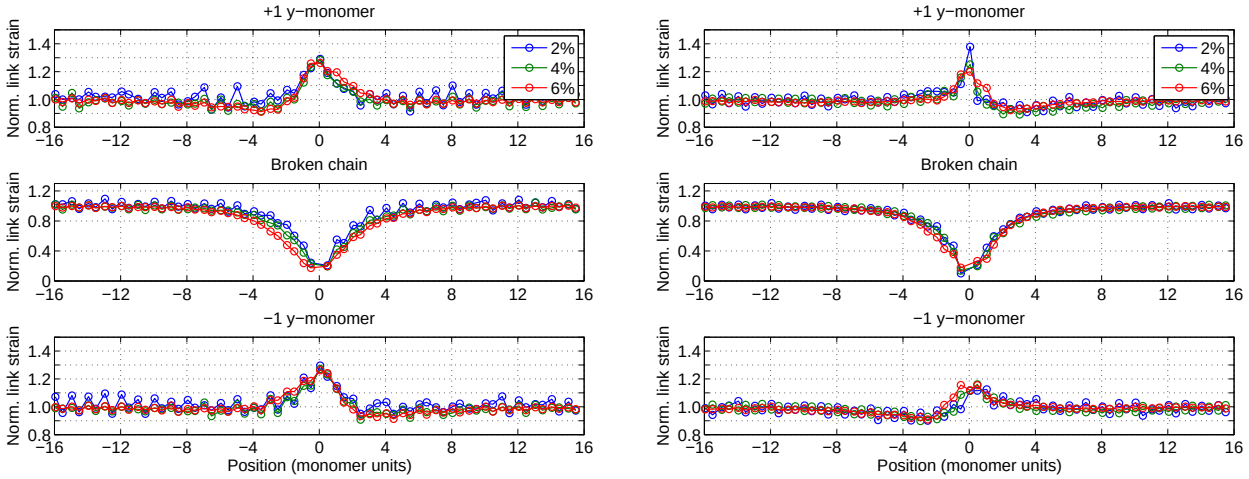

(a) *PCFF* **(b)** *ReaxFF*

Figure 4.12: *Response of links in PPTA chains for a system containing a single chain-end defect at monomer position 0*

.

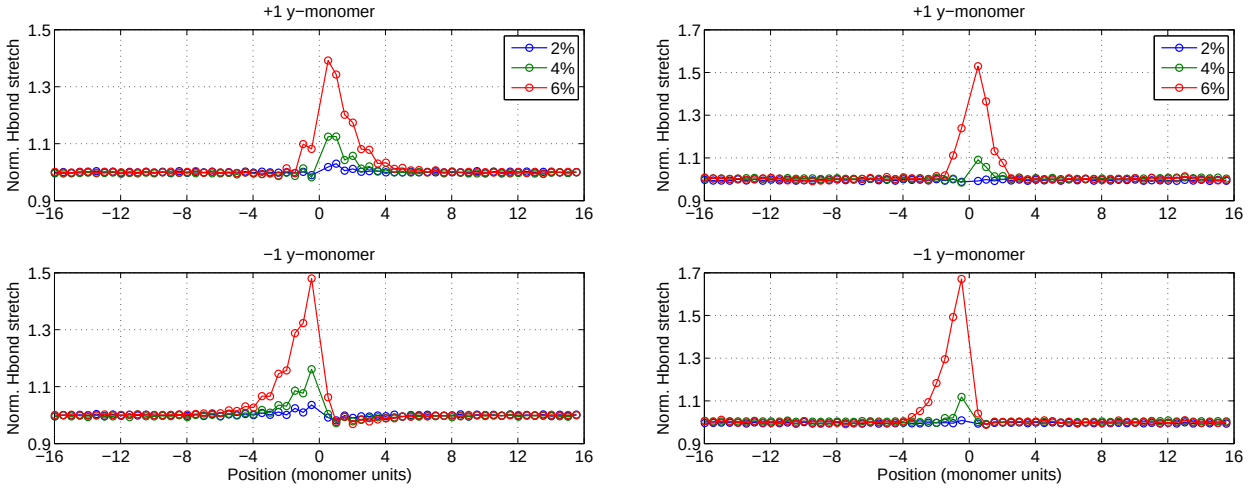

(a) *PCFF* **(b)** *ReaxFF*

Figure 4.13: *Response of hydrogen bonds in PPTA chains for a system containing a single chain-end defect located at monomer position 0.*

undergo slip which becomes exacerbated as the crystal strain is increased. This is due to the relaxation of the chain links in this region, and subsequent shortening of the chain. Since the size of the region of stretched hydrogen bonds coincides with the size of the region of relaxed link strain along the broken chain, it is clear that the relaxing of the links is the cause of the increased hydrogen bond stretch in this region.

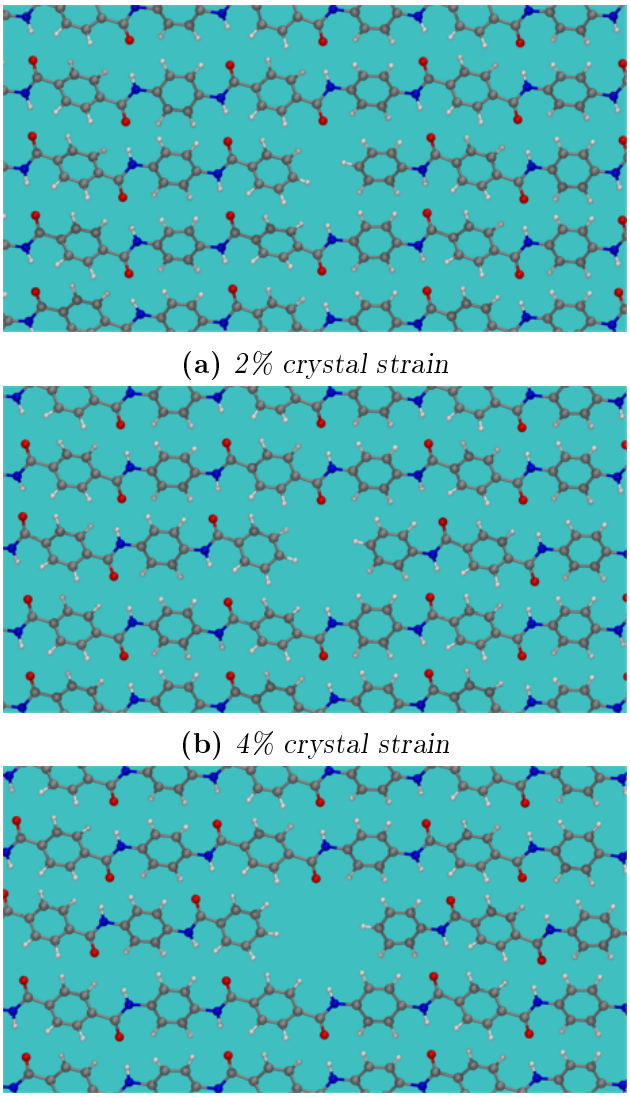

(a) *2% crystal strain*

(b) *4% crystal strain*

(c) *6% crystal strain*

Figure 4.14: *Visualization of the molecular deformation near the site of the chain-end defect. Note the increased stretch in hydrogen bonds near the defect, which occurs due to relaxation (shortening) of the broken chain relative to the adjacent chains.*

To assess the effect of multiple interacting defects in the crystal, the same procedure is repeated but with two chain-end defects introduced into the center chain. The defects are introduced at the -4 and $+4$ monomer positions in a single hydrogen-bonded sheet, segmenting the broken chain into two chains of 8 and 24 monomers in length. The portion of the broken chains and two adjacent chains lying between monomer position -4 and $+4$ are therefore within the zone of influence of both of the defects in the system. The resulting chain behavior is plotted in in Figure 4.15. As with the case of the single chain-end defect displayed

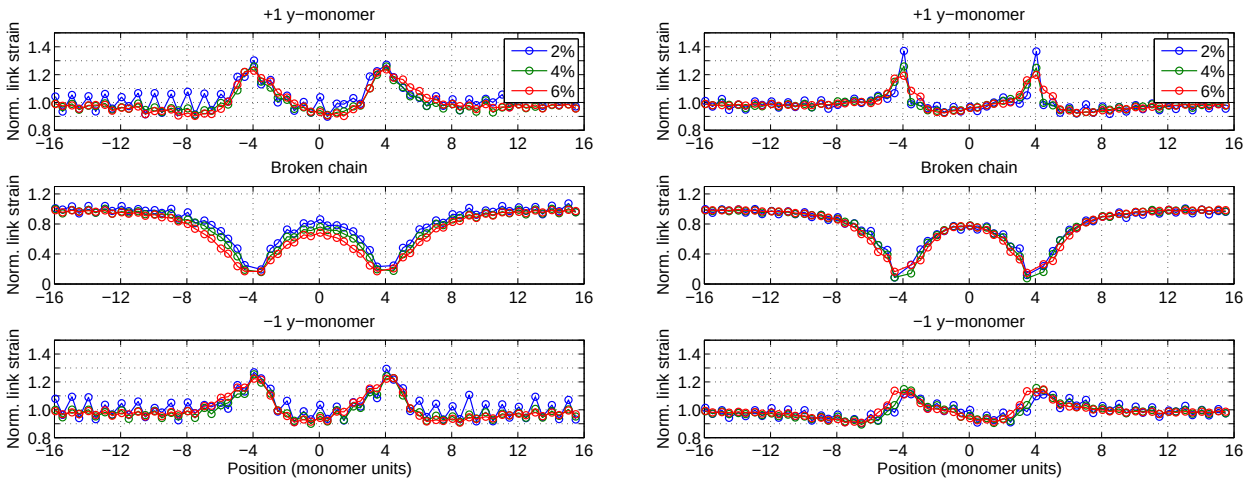

(a) *PCFF* **(b)** *ReaxFF*

Figure 4.15: *Response of links in PPTA chains for a system two chain-end defects at monomer position* +4 *and* −4.

in Figure 4.12, the only chains whose behavior is affected by the defect are the broken chain and the two in-sheet chains immediately adjacent to the broken chain. Between the −4 and +4 monomer positions, links in the short broken chain do not have an opportunity to return to the nominal link strain. Outside the ±4 monomer range, a return to nominal link strain can be seen to occur at about the ±12 monomer positions, indicating that the size of the relaxed region along the larger broken chain is within 8 monomers of the two defects, which is consistent with the size of the relaxed region observed in Figure 4.12. In the adjacent chains, the increase in link strain closely follows the behavior observed for the single chain-end case in Figure 4.12. Therefore, the presence of two interacting defects does not seem to exacerbate the stretch or relaxation of the links in nearby chains. The hydrogen bond behavior is also essentially identical to that displayed in Figure 4.13 – the only hydrogen bonds that undergo any change in length compared to the nominal hydrogen bond length in the crystal are those near the chain-end defect and along the broken chain, in the regions where the broken chain is relaxed.

Two more extreme cases of interacting defects are also presented. The first is that of three missing linkages in a row, creating a larger gap between chain-ends along the broken chain, as displayed in Figure 4.16. Figure 4.17 presents the results for this case for both the PCFF and ReaxFF force fields. It is observed that there is not a substantial difference in behavior between this case and the case of a single missing link (Figure 4.12) – the zone of influence of the defect is approximately the same, and the extent of the chain relaxation/stretching compared to the single missing link case is also approximately the same. Once again, the affected chains are constrained to the broken chain and two immediately adjacent chains in the same hydrogen-bonded sheet. The hydrogen bond response is essentially identical to that displayed in Figure 4.13.

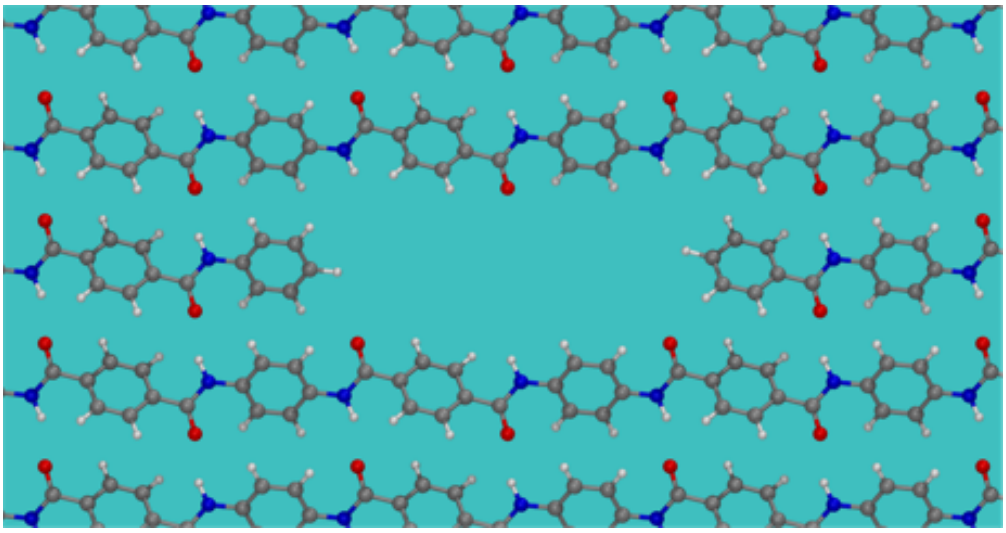

Figure 4.16: *Visualization of introducing three chain-end defects in a row, a total of three eliminated links along the center chain backbone.*

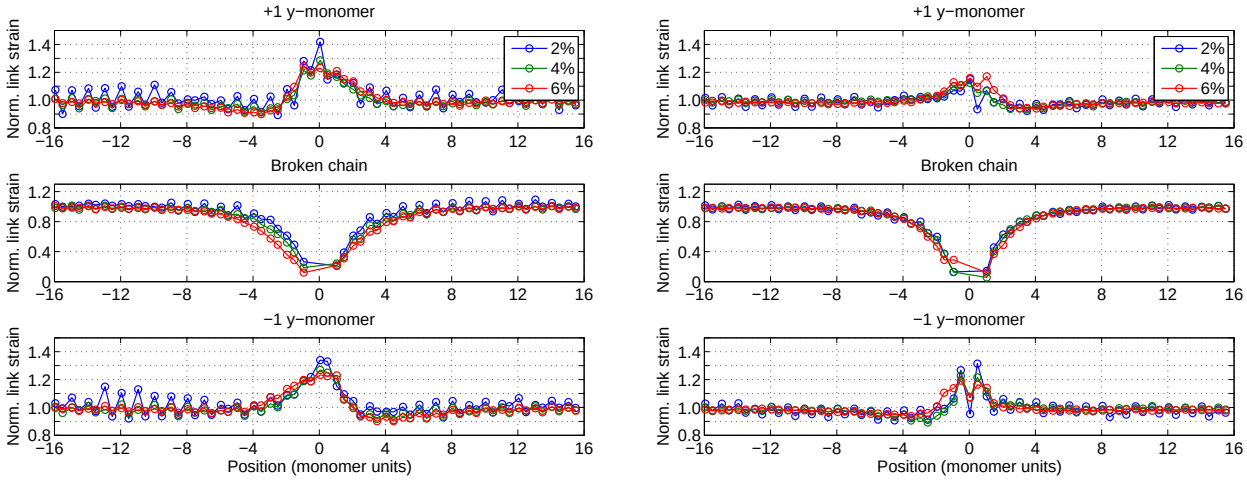

(a) *PCFF* **(b)** *ReaxFF*

Figure 4.17: *Response of links in PPTA chains for a system with three missing linkages in a row, as illustrated in Figure 4.16.*

The second case is that of a "crack", where three chain-ends are introduced at the same location in three consecutive adjacent chains, as illustrated in Figure 4.19a. The chain behavior is presented in Figure 4.18, and here it is seen that the chain behavior deviates substantially from the previous cases, particularly for crystal strains of 4% and higher. The stark difference in behavior occurs due to hydrogen bond breakage and subsequent chain slippage that occurs for chains near the crack tip, which is visualized in Figure 4.19b. The extent of the slippage is much less severe at lower strains, so the zone of influence is restricted

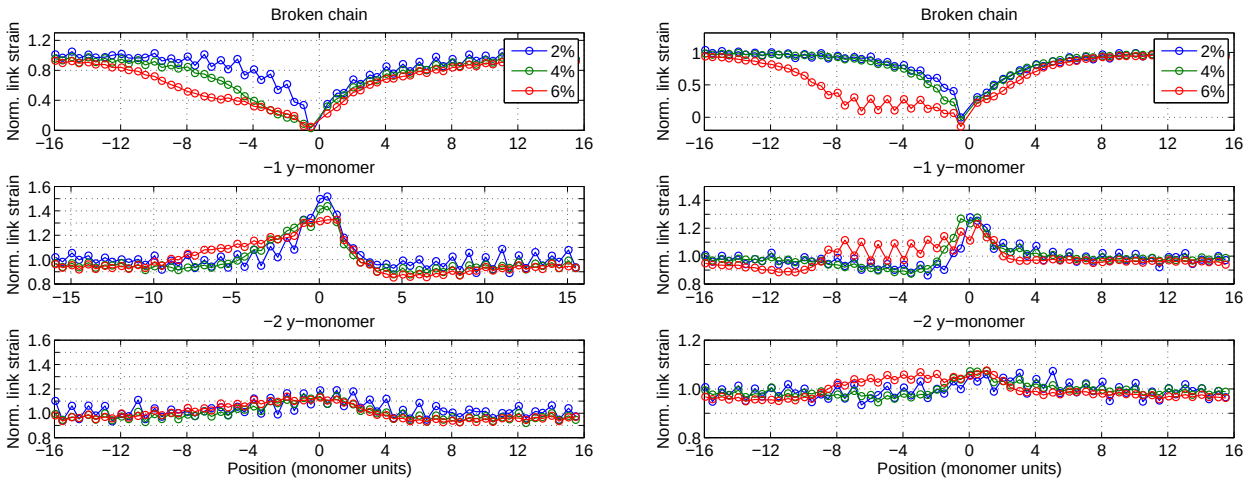

(a) *PCFF* **(b)** *ReaxFF*

Figure 4.18: *Response of links in PPTA chains for a system with a small crack, as illustrated in Figure 4.19a.*

to a smaller length of the broken chain for these cases. At all strain levels, the zone of influence extends to the two nearest adjacent monomers, rather than just the single nearest adjacent monomer as observed in the previous cases. Hence, defects have a much stronger influence on the behavior of neighboring chains when they are closely grouped between adjacent lateral chains than when they are stacked together on a single chain.

4.2.2 Influence of defects on strain rate loading response

With the local effects of individual defects now understood, attention is turned to the mechanical response of PPTA crystals consisting of finite-length chains, which are created by introducing various patterns of chain-end defects into an initially perfectly crystalline model of PPTA. Unless otherwise noted, chain-ends are introduced by creating a perfect crystal consisting of n_x, n_y, and n_z unit cells in the x, y, and z directions, respectively. Then, one chain-end defect is introduced into each chain in the system. With the application of periodic boundary conditions, this yields a system of chains of identical length. For example, a system with $n_z = 8$, with one eliminated link per chain, is a system where all chains are approximately 8 full PPTA monomers in length. The locations of the chain-ends are controlled to follow particular patterns in each model studied, in order to understand how different distributions of chain-end locations influences the mechanical response of the crystal.

To begin, a system of 8×8×64 unit cells, consisting of chains 64 monomers in length, is considered. Three variants of this system are studied. Variant I has its chain-ends distributed randomly throughout the simulation cell. In Variant II, all of the chain-ends are clustered in a region ±10 monomers about a plane bisecting the center of the simulation cell, whose

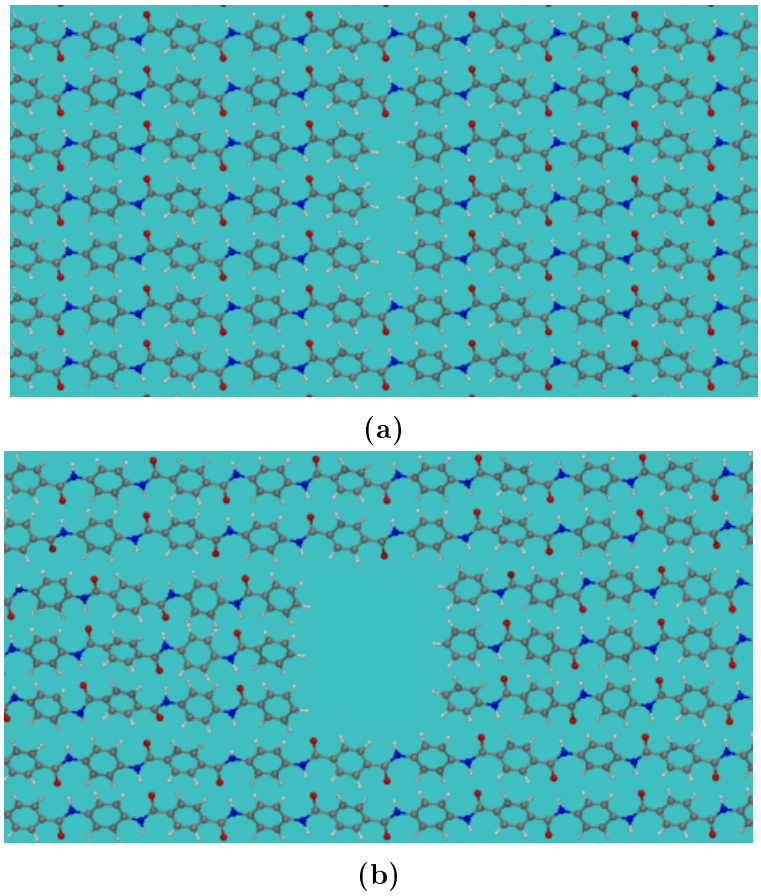

(a)

(b)

Figure 4.19: *Visualization of the introduction of three defects at the same location in three adjacent chains, mimicking a crack. Figure (a) shows the crack at equilibrium (0% strain), and Figure (b) highlights the hydrogen bond failure that occurs for chains near the crack tip when the crystal is stretched to 6% strain.*

normal vector is parallel to the z-axis. Variant III is similar to Variant II, but the clustering is constrained to an even smaller region of ± 4 monomers about the bisecting plane. Figure 4.20 offers a schematic diagram of the chain-end locations for each variant. These distribution patterns are chosen to represent the different descriptions of chain-end distributions observed experimentally per the discussions in Chapter 2. Variant I is representative of the skin region of fibers, where chain-ends are thought to be distributed randomly, and Variants II and III are more representative of the fiber core, where chain ends are thought to be concentrated in periodic defect planes. For the purpose of comparison, the response of each system is simulated using both the ReaxFF and PCFF potentials. Unlike in the case of perfect crystals, PCFF is capable of modeling failure in these models, since it is possible for the system to fail via chain-sliding and secondary bond rupture when the chains are not of infinite length. However, it should be noted that the PCFF response is not representative of true PPTA crystal behavior for the cases where ReaxFF predicts primary bond ruptures (in addition to

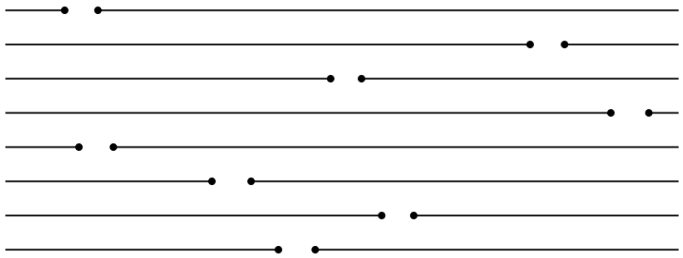

(a) *Variant I: chain-ends distributed randomly.*

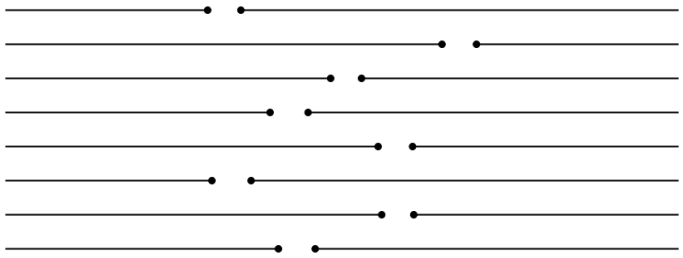

(b) *Variant II: chain-ends lie within* ± 10 *monomers of the center plane.*

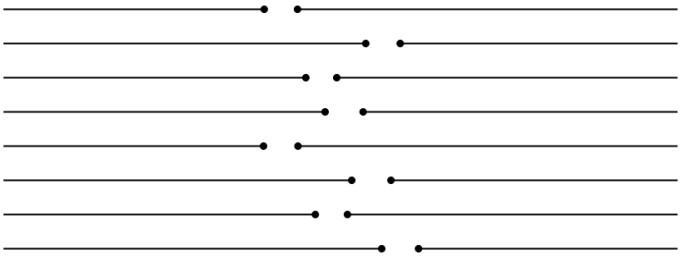

(c) *Variant III: chain-ends lie within* ± 4 *monomers of the center plane.*

Figure 4.20: *Diagram of the chain-end locations for each of Variants I, II, and III (not to scale). Each diagram shows representative single sheet of 8 chains. The simulation cell for each variant consists of* $8 \times 8 \times 64$ *unit cells.*

secondary bond ruptures) as part of the failure process.

Figure 4.21 shows the stress-train response of Variants I, II, and III, as well as that of the perfectly crystalline response for ReaxFF at a strain rates of 5.0×10^9 s^{-1} and 1.0×10^9 s^{-1}. From these plots, it is clear that the biggest difference between the responses of the different variants is the failure strain of the system. Among the variants including defects, Variant I is the strongest, and Variant III is the weakest. This is reasonable, since while each system

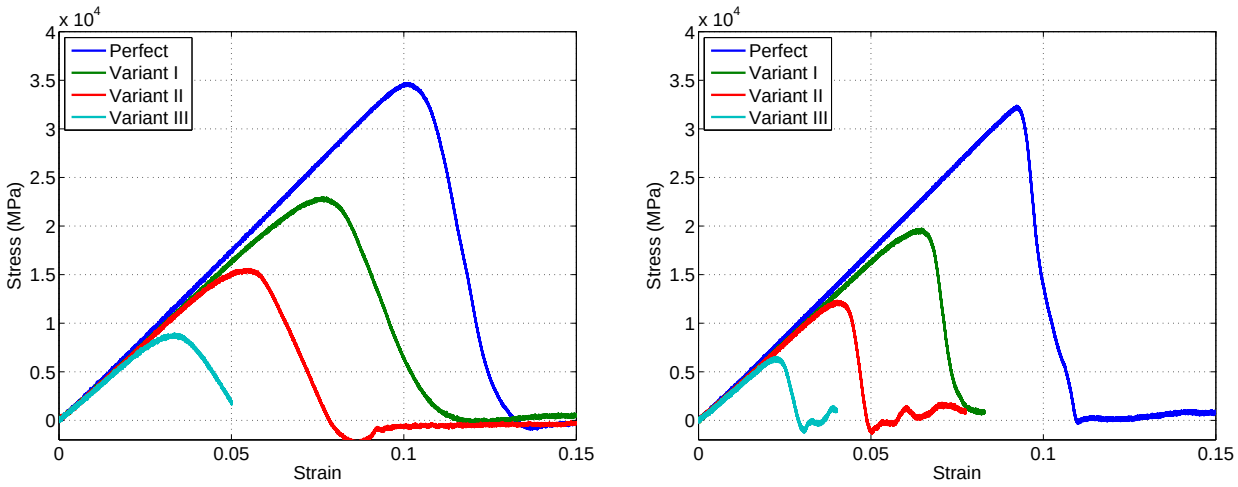

(a) $\dot{\epsilon} = 5.0 \times 10^9\ s^{-1}$ **(b)** $\dot{\epsilon} = 1.0 \times 10^9\ s^{-1}$

Figure 4.21: *Stress-strain response of Variants I, II, and III, as well as perfectly crystalline PPTA (8×8×64 unit cells), using ReaxFF.*

has chains of the same length, the chain ends in Variant I are scattered randomly throughout the system, while those in Variant III are grouped the closest together. Hence, Variant III exhibits a weak region with a high concentration of structural defects, and failure of the system becomes governed by the failure of this weak region. As in the case of perfectly crystalline PPTA, the failure strain of these systems increases with increasing strain rate, and the modulus of each system is not affected by the strain rate. Variants I, II, and III each have an elastic modulus of 306 GPa, a slight decrease relative to the 320 GPa modulus of the perfectly crystalline system; this is a direct result of the introduction of structural defects into the system.

Figures 4.22–4.24 show the stress-strain curves and primary and hydrogen bond break history for Variants I, II, and III at a strain rate of $1.0 \times 10^9\ s^{-1}$, for both PCFF and ReaxFF. In the ReaxFF model, Variants I and II experience some initial hydrogen bond ruptures before the onset of primary bond ruptures. Variant III features hydrogen bond ruptures almost exclusively, with the sole primary bond rupture coming well after failure of the system. The number of primary bond ruptures is highest in Variant I, followed by Variant II and then Variant III, indicating that primary bonds are more likely to rupture when the chain-end defects are spread out further apart. The influence of defects on local chain behavior as studied in Section 4.2.1 can assist in explaining this behavior. Variant III has a defect band width of 8 (± 4) monomers, which means the links within the defect band are all influenced by the presence of the defects. In particular, they all undergo relaxation relative to the other links outside the defect band, and the Type 2 primary bonds within these relaxed links are therefore less likely to fail. In contrast, the hydrogen bonds in this defect band undergo additional stretching, making them more susceptible to failure. The result is hydrogen bond-dominated failure of this system. In Variant II, defects are clustered

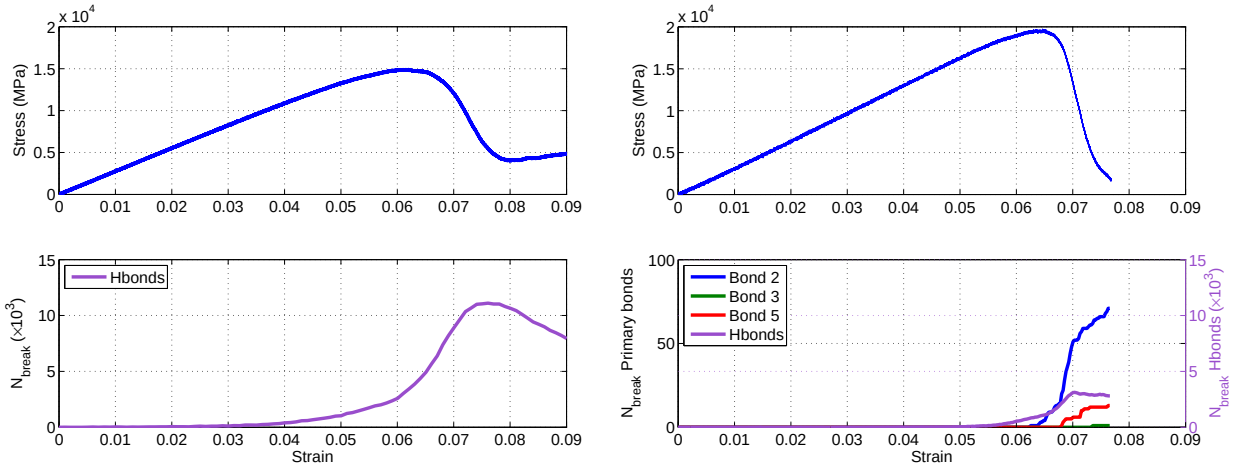

(a) *PCFF with* $\dot{\epsilon} = 1.0 \times 10^9\ s^{-1}$ **(b)** *ReaxFF with* $\dot{\epsilon} = 1.0 \times 10^9\ s^{-1}$

Figure 4.22: *Stress-strain and bond break histories for Variant I obtained from the PCFF and ReaxFF force fields.*

far enough apart that some links in the defect band retain their full level of stretch, which leads to primary bond failure. The clustering of the defects leads to a weak plane and system failure occurs earlier than in Variant I. In Variant I, the defects are spread far apart, and failure must occur primarily through primary bond rupture rather than chain sliding and secondary bond rupture. Spreading out the defects in this system leads to a larger failure strain than in Variants II and III. Since Variants I and II experience significant primary bond failures, the PCFF response for these systems is likely not representative of true crystalline PPTA behavior. However, PCFF is capable of capturing the response of Variant III, where primary bond rupture does not play a significant role in the failure process.

Variants I–III represent systems of long polymer chains, and by way of completeness, the other extreme is now considered by introducing Variant IV, which is a system of 4×4×8 unit cells consisting of one break per chain with chain-ends randomly distributed. With this smaller system, comprised of 7,104 atoms compared to the 229,120 atoms comprising Variants I–III, studying the stress-strain response for lower strain rates is more tractable due to the decreased computational expense. The stress-strain curves and bond break histories at a strain rate of 1.0×10^9 s^{-1} using both the PCFF and ReaxFF force fields are plotted in Figure 4.25. The ReaxFF response does not exhibit any primary bond ruptures, and failure of the system is by hydrogen bond rupture only. This renders PCFF perfectly capable of capturing the failure response as well. However, Figure 4.25 highlights some notable differences in the response between the PCFF and ReaxFF models, which is indicative of the different parameterizations of the hydrogen bond terms in each force field. The PCFF response appears to show a healing of hydrogen bonds post failure, after about 6% strain, whereas the hydrogen bonds in ReaxFF do not heal. PCFF also predicts a failure strain of about 3%, while ReaxFF predicts a failure strain just over 4%.

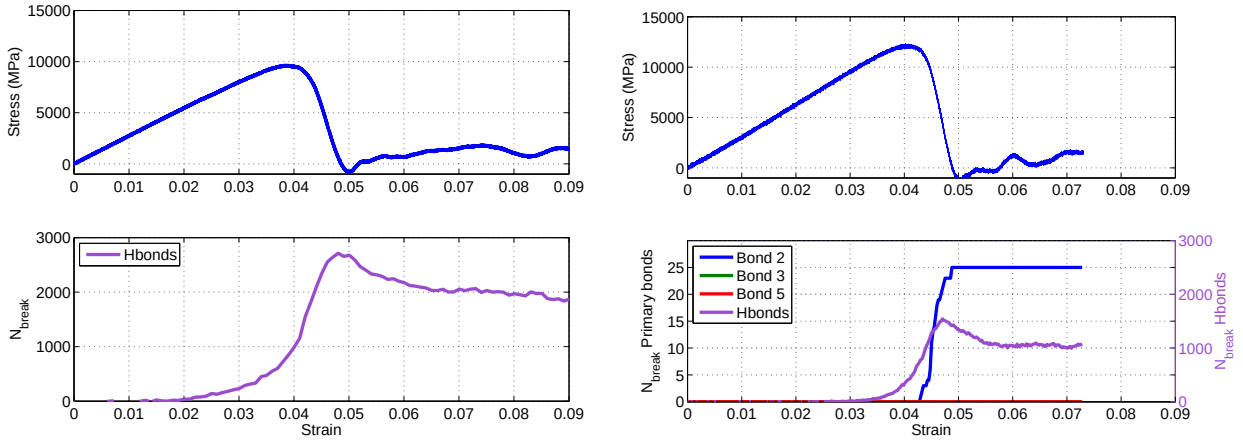

(a) *PCFF with* $\dot{\epsilon} = 1.0 \times 10^9\ s^{-1}$ **(b)** *ReaxFF with* $\dot{\epsilon} = 1.0 \times 10^9\ s^{-1}$

Figure 4.23: *Stress-strain and bond break histories for Variant II obtained from the PCFF and ReaxFF force fields.*

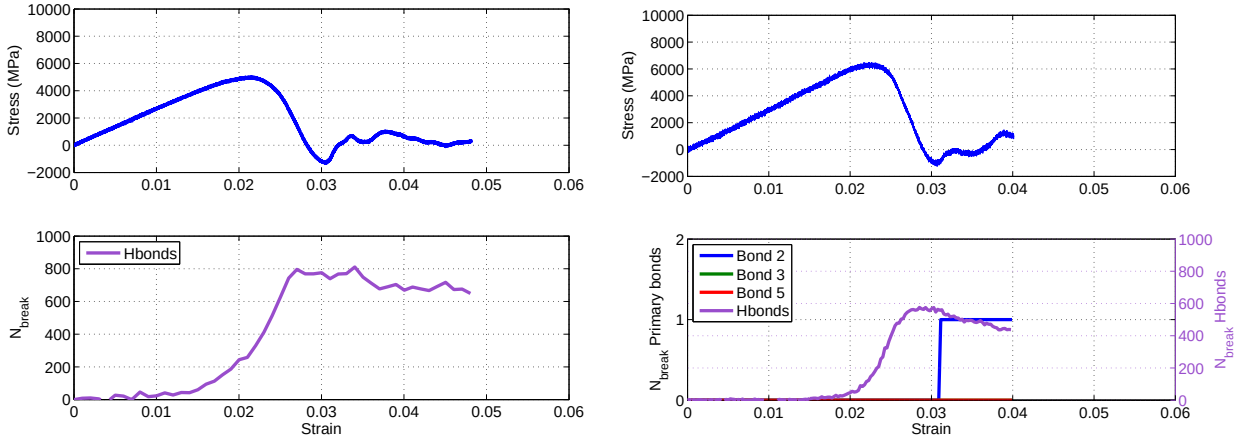

(a) *PCFF with* $\dot{\epsilon} = 1.0 \times 10^9\ s^{-1}$ **(b)** *ReaxFF with* $\dot{\epsilon} = 1.0 \times 10^9\ s^{-1}$

Figure 4.24: *Stress-strain and bond break histories for Variant III obtained from the PCFF and ReaxFF force fields.*

As with the case of perfectly crystalline PPTA, the influence of strain rate on the response of Variant IV is studied by running strain-to-failure simulations at strain rates of 5.0×10^9 s^{-1}, 1.0×10^9 s^{-1}, 2.0×10^8 s^{-1}, and 4.0×10^7 s^{-1} in both PCFF and ReaxFF. Five equilibrated starting points are chosen for each rate in order to capture to stochastic nature of the failure strain. Figures 4.26 and 4.27 plot one stress-strain curve per strain rate studied for PCFF and ReaxFF, and consistent with all results obtained so far, the stress response is approximately linear until failure, and the initial modulus E_{zz} is unchanged by the strain rate. The modulus of the PCFF and ReaxFF systems is equal to 172 GPa and 173 GPa, respectively, with

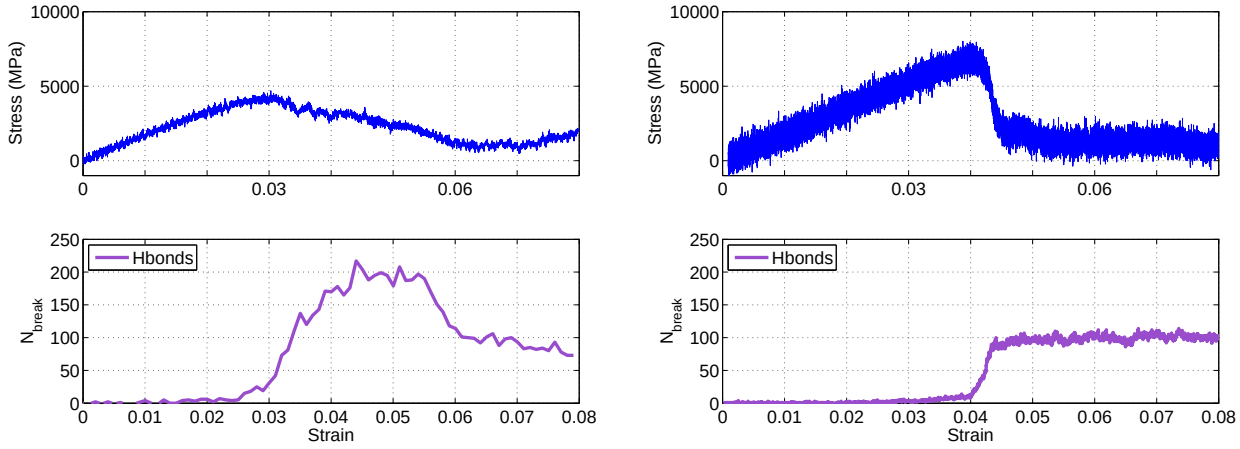

(a) *PCFF with* $\dot{\epsilon} = 1.0 \times 10^9\ s^{-1}$ **(b)** *ReaxFF with* $\dot{\epsilon} = 1.0 \times 10^9\ s^{-1}$

Figure 4.25: *Stress-strain and bond break histories for Variant IV obtained from the PCFF and ReaxFF force fields. The ReaxFF model does not predict any primary bond breakages in this case.*

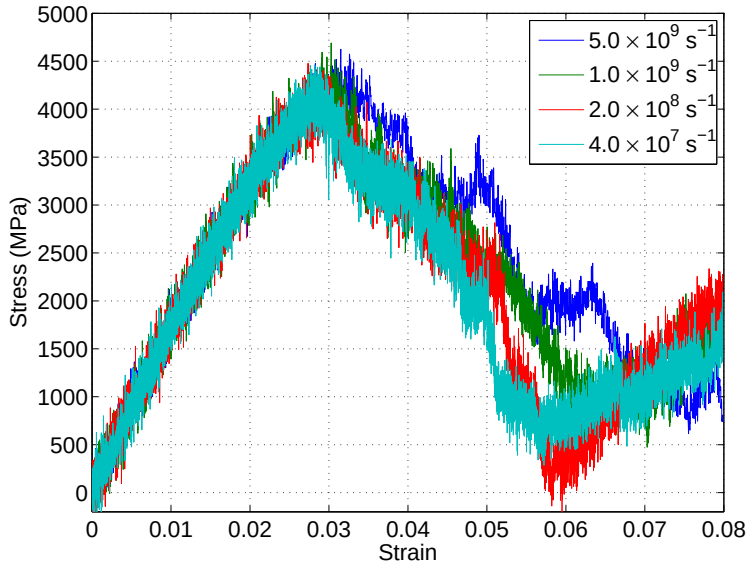

Figure 4.26: *PCFF stress-strain response for Variant IV.*

the significant decrease relative to the perfectly crystalline modulus attributed to the high concentration of chain-end defects in the system. The relationship between failure strain and strain rate for both force fields is plotted in Figure 4.28, and once again, a nearly linear relationship between failure strain and log strain rate is obtained for this regime of strain rates. This suggests that failure by hydrogen bond rupture is also governed by thermally activated failure events, just as in the case of primary bond rupture.

Experimental evidence suggests that in true PPTA fibers, the crack that develops through

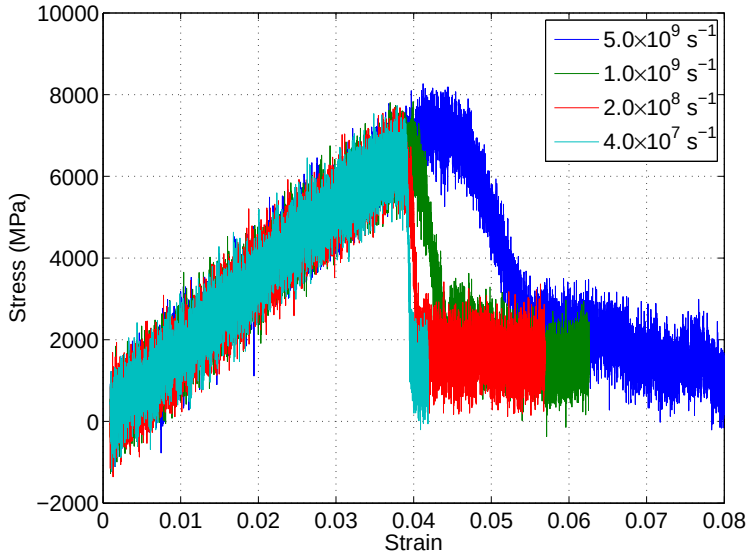

Figure 4.27: *ReaxFF stress-strain response for Variant IV.*

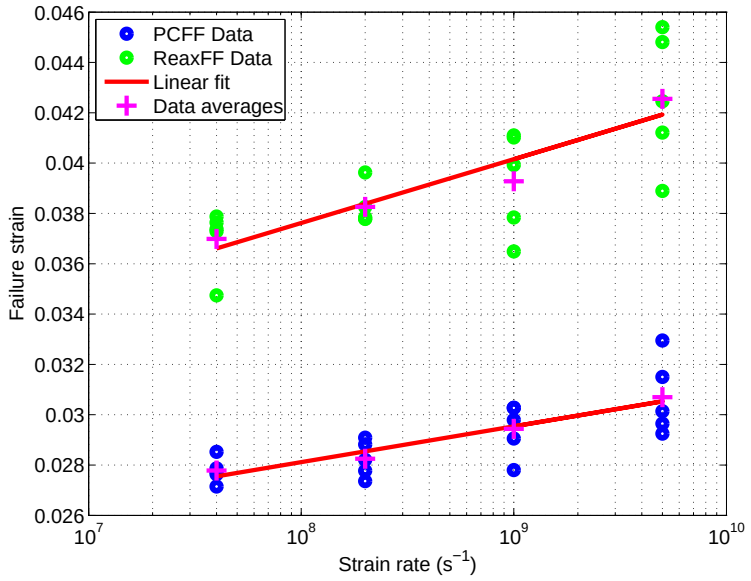

Figure 4.28: *Failure strain versus strain rate for both PCFF and ReaxFF models of Variant IV.*

the cross section of a fiber during failure travels along the hydrogen bond interface between adjacent PPTA chains, rather than rupturing primary bonds along the chain backbone. Figure 4.29 provides a schematic of this hypothesized crack path. In the MD simulations performed here of Variants I–IV, both primary bond and hydrogen bond rupture were observed, depending on the chain-end defect concentration and the length of the chains. The MD results suggest that when chains are long and defects are not locally concentrated in

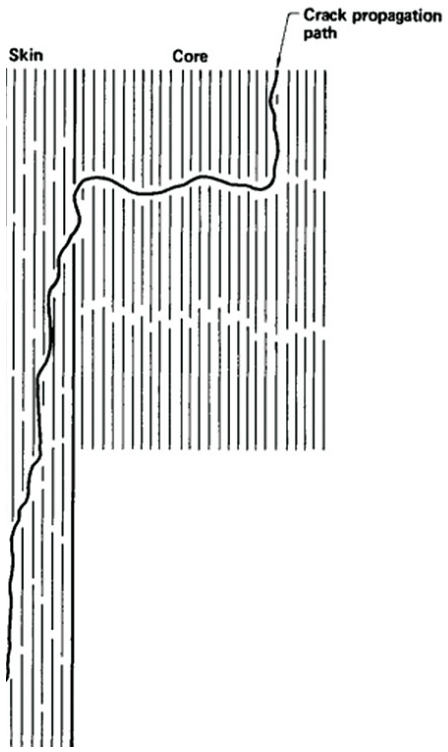

Figure 4.29: *The crack propagation path suggested by Morgan et al. [48], showing rupture of hydrogen bonds between adjacent PPTA chains in the fiber.*

defect planes, as in Variant I, primary bond rupture plays a major role in the failure process. As the defect concentration becomes either high (Variant IV) or locally concentrated (Variants II and III), hydrogen bond ruptures become more prominent. This suggests that the core of a PPTA fiber containing chain-end defect planes likely may fail through a combination of primary and hydrogen bond ruptures, whereas the skin of the fiber (where chain-ends are randomly distributed) is more likely to fail via primary bond rupture.

4.2.3 Influence of defects on axial stiffness

The influence of defect concentration and distribution on the modulus of the system is the final topic considered here. It has already been discussed that the observed modulus of each of Variants I, II, and III is 306 GPa in ReaxFF. The modulus for the PCFF model of each of those variants is 275 GPa, indicating that the modulus of each variant in either force field is independent of the defect location once the number of defects and chain length are fixed. The drop to a modulus of 173 GPa in ReaxFF and 172 GPa in PCFF for Variant IV suggests that the global chain-end concentration and/or the length of the PPTA chains has a strong

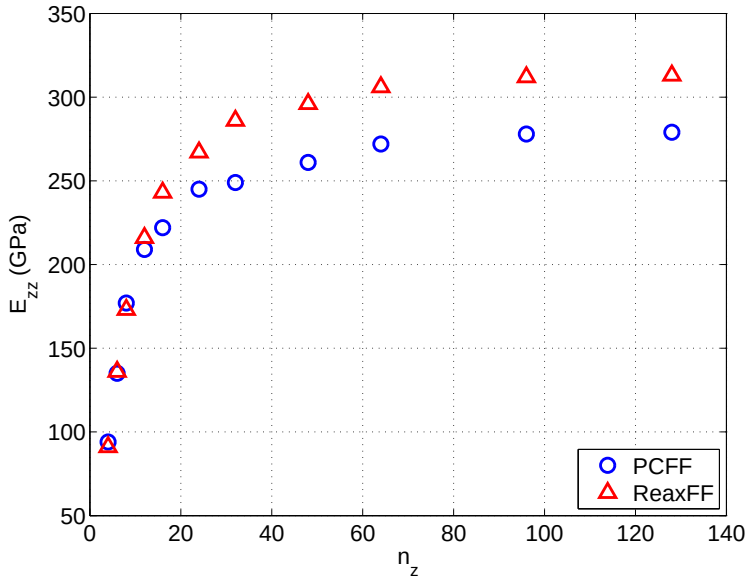

Figure 4.30: *Modulus versus n_z for both PCFF and ReaxFF.*

effect on the modulus. In an attempt to quantify the influence of defect concentration and chain length on modulus, a number of different models with varying defect concentrations and chain lengths are now studied.

Since the strain rate simulations of Variants I–III showed no change in modulus with defect location, the set of models used to study the influence of defect concentration on modulus follow that of Variant I or IV: starting from a perfect crystal cell n_z monomers in length, a single defect is introduced at a random location in each chain of the cell, effectively creating a model of chains n_z monomers in length with the chain-end locations distributed randomly. Chain lengths of n_z = 4, 6, 8, 12, 16, 24, 32, 48, 64, 96, and 128 were tested, and the resulting modulus values are plotted in Figure 4.30. The figure shows increasing the chain length has a very strong effect on the increase in modulus initially, but this effect plateaus once a chain length of about 64 monomers is reached.

In order to better understand how the modulus depends on chain length, an analysis was conducted to determine what parts of the crystal are responsible for bearing the load in the cell. This was done through a post-processing technique whereby select modifications were made to the interatomic potential, and the original molecular dynamics trajectory from the simulations measuring elastic moduli is read while applying the modified force field. In particular, one analysis re-processed the original trajectory with all primary bond interactions turned off, such that only pairwise interactions contributed to atomic forces. A second analysis re-processed the trajectory with the O–H interaction omitted, essentially eliminating hydrogen bonds from contributing to the stress. In this setup, the first analysis reports a stress which neglects contributions from the load carried by the molecular chain backbone of primary bonds, and the second analysis reports the stress neglecting the load

carried by the secondary bonds.

Remarkably, the analysis showed that the modulus for the case of omitting secondary bond interactions was nearly unchanged compared to the true modulus, while the modulus was computed to be nearly zero when primary backbone bond contributions were omitted. These results were observed for both the PCFF and ReaxFF potentials. This offers strong evidence that the load in the crystal is borne almost entirely by the PPTA chain backbones, rather than by the surrounding secondary bonds. The surrounding bonds serve to keep the chains bound together in the lateral direction, essentially allowing the chains to act as a collection of parallel springs which determine the stiffness of the crystal.

The zone of influence results show that a broken chain experiences a region of relaxation near the defect site, while adjacent chains undergo additional stretching due to load transfer. In all cases, the extent of relaxation appears more severe than the extent of stretching in adjacent chains, and if the chains bear all of the load in the crystal, then this relaxation explains the drop in modulus with the introduction of higher concentrations of chain-ends. A simple model is now proposed to explain this. Consider a crystal containing chains of n_z monomers in length. If the chains are long enough such that the end-to-end distance is greater than the zone of influence of a chain-end defect, then there is a part of the chain which returns to its nominal strained state under an axial load. Let L_1 be the length of the chain that is at nominal stiffness, and L_2 be the length of the chain that is at some lower value of stiffness. L_2 consists of any regions not at the nominal strain, which includes relaxed regions near the defects, and strained regions which occur due to proximity to defects in neighboring chains. Each region has an associated spring constant k_1 and k_2, and the total length of the chain is $L_c = cn_z$, where c is the length of a single monomer in the crystal. The effective stiffness k_c of this series of two chains is given by

$$k_c = \frac{1}{\frac{1}{k_1} + \frac{1}{k_2}} = \frac{k_1 k_2}{k_1 + k_2} \ . \tag{4.6}$$

Assuming each chain covers the same cross-sectional area, an effective Young's modulus can be computed as

$$\frac{E}{L_c} = \frac{\frac{E_1 E_2}{L_1 L_2}}{\frac{E_1}{L_1} + \frac{E_2}{L_2}} \ . \tag{4.7}$$

The ratio of chain stiffness to the stiffness in a perfect crystal can then be expressed as

$$\frac{E}{E_1} = \frac{L_c E_2}{L_2 E_1 + L_1 E_2} \ . \tag{4.8}$$

Using volume fractions $f_i = \frac{L_i}{L_c}$, equation (4.8) can be rewritten as

$$\frac{E}{E_1} = \frac{1}{f_1 + f_2 \frac{E_1}{E_2}} \ . \tag{4.9}$$

Using the fact that volume fractions sum to 1 and $f_2 = \dfrac{L_2}{L_c}$, equation (4.9) is rewritten as

$$\frac{E}{E_1} = \frac{1}{1 + \dfrac{1}{L_c}\left[L_2\left(\dfrac{E_1}{E_2} - 1\right)\right]} \ . \tag{4.10}$$

The ratio of the perfect crystal modulus E_1 to the modulus of the region weakened region E_2 is a constant, as is the length L_2, which represents the size of the zone of influence of the defects in the system. Operating under these assumptions, the ratio of crystal modulus to perfect crystal modulus can be expressed as

$$\frac{E}{E_1} = \frac{1}{1 + \dfrac{a}{L_c}} \ , \tag{4.11}$$

where a is a constant. To test whether the model is suitable, a least-squares fit is performed on the PCFF and ReaxFF modulus versus chain length data to determine a suitable value for the constant a. The model assumes that chain-ends are placed far enough from one another such that there is no interaction between defects, and for this reason, the model is fit only to modulus data for systems containing chains of 16 monomers in length or longer, such that defects are likely to be spaced far apart from one another. The resulting fits are displayed in Figure 4.31, and suggest that the model is indeed capable of capturing the modulus behavior of the chains by considering the volume fraction of chain relaxation that occurs due to the presence of chain-end defects.

The analysis performed here shows that the PPTA chains themselves, rather than adjacent hydrogen bonds, bear nearly all of the load when PPTA crystals loaded along the fiber axis. As a result, the modulus depends on the stiffness and load bearing capacity of these chains, and the model proposed by equation (4.11) describes this behavior adequately by considering chains as a series connection of perfect and reduced load-bearing capacity chains. The data shows that the crystal stiffness plateaus once chains are about 64 monomers in length. Aramid fibers typically contain chains of about 150 monomers in length, which essentially achieves the maximum stiffness possible. The simulation results therefore suggest that aramid fiber stiffness gains are best pursued through methods other than lengthening the polymer chains, for example, by improving the chain alignment with the fiber axis.

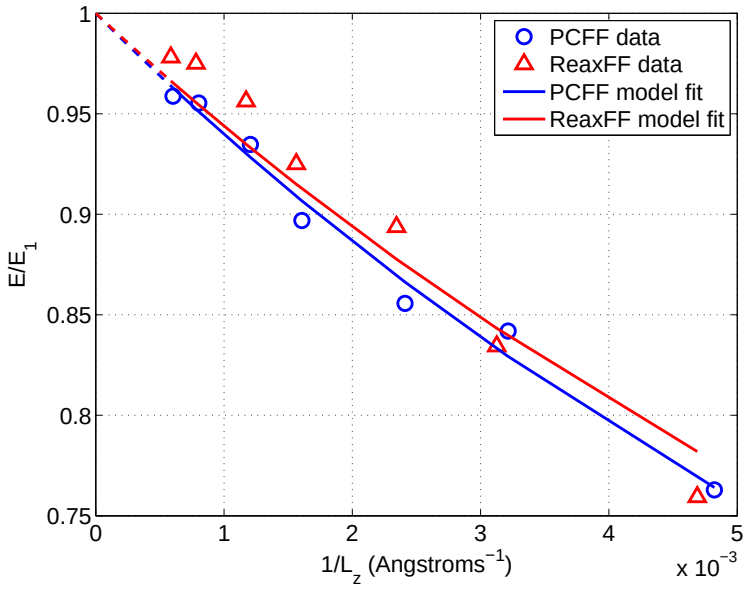

Figure 4.31: *Normalized crystal modulus versus inverse of chain length for both PCFF and ReaxFF. The dotted lines represent a best fit of the parameter a of equation (4.11) to the data. Reasonable agreement is obtained.*

Chapter 5

Analysis of failure in PPTA crystals

In Chapter 4, it was observed that the failure of crystalline PPTA is governed by the failure of individual primary and secondary bonds within the crystal, and that the failure strain of PPTA crystallites depends on the applied strain rate and temperature. In this chapter, the mechanisms of crystallite failure are studied in further detail, with particular focus on how individual bonds contribute to the failure process. Both primary and secondary bond failure is addressed, including how bond failure is influenced by the presence of defects in the crystal. Based on the observations made with respect to bond failure behavior, a model based on reliability theory is proposed which models bonds as having time-dependent failure rates which depend on the rate of loading and crystallite temperature. This model can be used to consider the failure of bonds at slow strain rates and large crystals that are prohibitively costly to simulate using standard molecular dynamics methods.

5.1 Reliability theory

Reliability theory is often used to predict the lifetime of engineering systems or components based on the observed distribution of lifetimes of tested components. It can be used to assess the likelihood of failure at a particular point in time, given a system whose probability of failure may change over time. The following is a summary of the important results of the theory as presented in [32]. Reliability theory will be used in this work in the context of modeling the failure of primary and secondary bonds in crystalline PPTA as stochastic processes with a failure rate that depends on the loading conditions in the crystal.

It is assumed that the time to failure T of the component of interest is a continuous random variable with probability density function (PDF) $f(t)$. The lifetime of the component begins at $t = 0$, and the cumulative distribution function (CDF) $F(t)$ for T is

$$F(t) = \Pr(T \leq t) = \int_0^t f(t')\, dt' \ , \tag{5.1}$$

which gives the probability $\Pr\,(T \leq t)$ that failure occurs before time t. Often, it is of interest to compute the probability that the component of interest survives until time t (or

equivalently, that failure occurs after time t), which is given by the survival function

$$S(t) = \Pr(T \geq t) = 1 - F(t) = \int_t^\infty f(t')\,dt' \ . \tag{5.2}$$

The distribution of failure times T may also be characterized by the hazard function (also known as the failure rate function), which is the instantaneous rate of occurrence of the failure event, conditional on failure not having occurred before time t. The hazard rate function is defined by

$$\begin{aligned} \lambda(t) &= \lim_{dt\to 0} \frac{\Pr(t \leq T < t + dt \,|\, T \geq t)}{dt} \\ &= \frac{1}{S(t)} \lim_{dt\to 0} \frac{F(t+dt) - F(t)}{dt} \\ &= \frac{F'(t)}{S(t)} \\ &= \frac{f(t)}{S(t)} \ , \end{aligned} \tag{5.3}$$

where the notation $\Pr(A \,|\, B)$ is used to denote the the conditional probability of A given B. Noting from equation (5.2) that $S'(t) = (1 - F(t))' = -f(t)$, it is also possible to write equation (5.3) as

$$\lambda(t) = \frac{-S'(t)}{S(t)} = -\frac{d}{dt} \ln S(t) \ . \tag{5.4}$$

Using a boundary condition of $S(0) = 1$, since the component is assumed to begin from an unfailed state at $t = 0$, equation (5.4) may be integrated in time to yield $S(t)$ as

$$S(t) = \exp\left[-\int_0^t \lambda(t')\,dt' \right] \ . \tag{5.5}$$

To obtain the mean time to failure μ, the expectation of the variable T is computed using the PDF $f(t)$ as

$$\mu = \mathrm{E}(T) = \int_0^\infty t f(t)\,dt \ = -\int_0^\infty t S'(t)\,dt \ . \tag{5.6}$$

Using integration by parts, (5.6) may be written as

$$\mu = -tS(t)\Big|_0^\infty + \int_0^\infty S(t)\,dt \ . \tag{5.7}$$

If $\mu < \infty$ it can be shown that $-tS(t)\Big|_0^\infty = 0$, and equation (5.7) can be simplified to

$$\mu = \int_0^\infty S(t)\,dt \ . \tag{5.8}$$

The variance in the mean time to failure is defined as

$$\sigma^2 = \mathrm{E}(T^2) - [\mathrm{E}(T)]^2 = \int_0^\infty t^2 f(t)\,dt - \mu^2 \;= -\int_0^\infty t^2 S'(t)\,dt - \mu^2 \;, \tag{5.9}$$

with μ defined in equation (5.8). Using a similar integration by parts procedure as with equations (5.6–5.8), equation (5.9) can be simplified to

$$\sigma^2 = \int_0^\infty 2tS(t)\,dt - \mu^2 \tag{5.10}$$

5.1.1 The special case of constant hazard rate

The theory presented so far is applicable to the general case of a time-varying rate of failure $\lambda(t)$. A simple special case (which will be shown to be applicable in the failure model for crystalline PPTA) is that of a failure rate λ which is constant in time. Following equation (5.5), the survival function for this case is

$$S(t) = \exp\left[-\int_0^t \lambda\,dx\right] \;= e^{-\lambda t} \;. \tag{5.11}$$

Using equation (5.2), the probability of failure before time t can be written as

$$F(t) = 1 - S(t) = 1 - e^{-\lambda t} \;. \tag{5.12}$$

Therefore, the PDF function for the distribution of failure times becomes

$$f(t) = F'(t) = \lambda e^{-\lambda t} \;, \tag{5.13}$$

which is simply the exponential distribution. Consider the probability of survival of a component until time $t + \Delta t$ given it has survived until time t:

$$\Pr(T > t + \Delta t \,|\, T > t) = \frac{S(t+\Delta t)}{S(t)} = \frac{e^{-(t+\Delta t)\lambda}}{e^{-\lambda t}} = e^{-\lambda \Delta t} = S(\Delta t) \;. \tag{5.14}$$

Therefore, the probability of survival during any interval of length of time Δt is independent of how long the component has been in operation. This is called the "memoryless" property of the exponential distribution, and is a direct consequence of the constant failure rate λ.

The mean time to failure according to equation (5.8) is

$$\mu = \int_0^\infty e^{-\lambda t}\,dt = \frac{1}{\lambda} \;, \tag{5.15}$$

and using this result combined with equation (5.10), the variance is computed as

$$\sigma^2 = \int_0^\infty 2te^{-\lambda t}\,dt - \left(\frac{1}{\lambda}\right)^2 = \frac{1}{\lambda^2} \;. \tag{5.16}$$

Hence, for a constant failure rate, the mean time to failure μ is equal to the inverse of the failure rate, and the standard deviation σ is equal to the mean.

5.2 Primary bond failure in crystalline PPTA

5.2.1 Observations of primary bond failure behavior in MD simulations

In Chapter 4, it was observed that primary bond failure played an important role in the failure of all of the PPTA crystal variants examined except for those involving high local concentrations of chain ends. Understanding how primary bonds fail is therefore critical to understanding the failure behavior of PPTA crystallites. As a first step in analyzing primary bond rupture, the molecular dynamics trajectory of the rupture of a hydrogen-bonded sheet is observed in detail. Recall that in Chapter 4 it was observed that the failure of the system was essentially governed by the failure of the individual hydrogen-bonded sheets comprising the system. Hence, observing how an individual sheet fails offers insight into how the crystal as a whole fails. Figure 5.1 presents a visualization of the progression of bond breaks that occur in a single sheet in a system consisting of 4×4×8 unit cells stretched at a strain rate of 1.0×10^9 s^{-1}. Observing this trajectory reveals that the rupture of a primary covalent bond along the chain backbone converts the potential energy stored in the bond into kinetic energy, causing the chain to snap, much like a stretched rubber band which suddenly breaks. This snapping action of the chain disrupts the hydrogen bonds between the broken chain and its neighboring chains within the sheet, and this disruption in crystal structure leads to additional primary bond ruptures in the neighboring chains. Hence, in the 4×4×8 system, it seems that a single bond rupture within a sheet triggers a cascade of bond rupture events, rendering the sheet failed shortly after the first bond rupture occurs. Note that Figure 4.1 presents the stress-strain curve and bond break history for the same simulation considered here, and indeed, it appears that the onset of first primary bond failure is commensurate with the failure strain (strain at peak stress) of the system.

In contrast, it is observed that in larger systems, the first primary bond failure is in general not commensurate with system failure. Figures 5.2 and 5.3 present the stress-strain curves and primary bond break history (at strain rates of of 1.0×10^9 $s^{-1}$and 2.0×10^8 s^{-1}, respectively) of a simulation cell of 8×8×64 unit cells of perfectly crystalline PPTA modeled using the ReaxFF force field. In each figure, it is clear that a number of primary bond ruptures occur before the failure strain of the system is reached. The difference between the behavior of this system and the smaller 4×4×8 system can be attributed to the impact that a single bond rupture has in each system. Due to the periodic boundary conditions used to model each system, a break in the smaller system represents a much larger concentration of bond breaks in the crystal than does a break in the larger system. Consider the zone of influence study presented in Chapter 4, where the effect of a single chain-end defect on local molecular behavior was studied. The introduction of a chain-end defect (structurally equivalent to a ruptured covalent bond) caused relaxation of the links within ±8 monomers of the broken chain, and also caused links to undergo additional stretching in the two adjacent chains to the broken chain. For a 4×4×8 unit cell system, a single bond break therefore influences the behavior of 3 of the 4 chains comprising the sheet in which the break occurs.

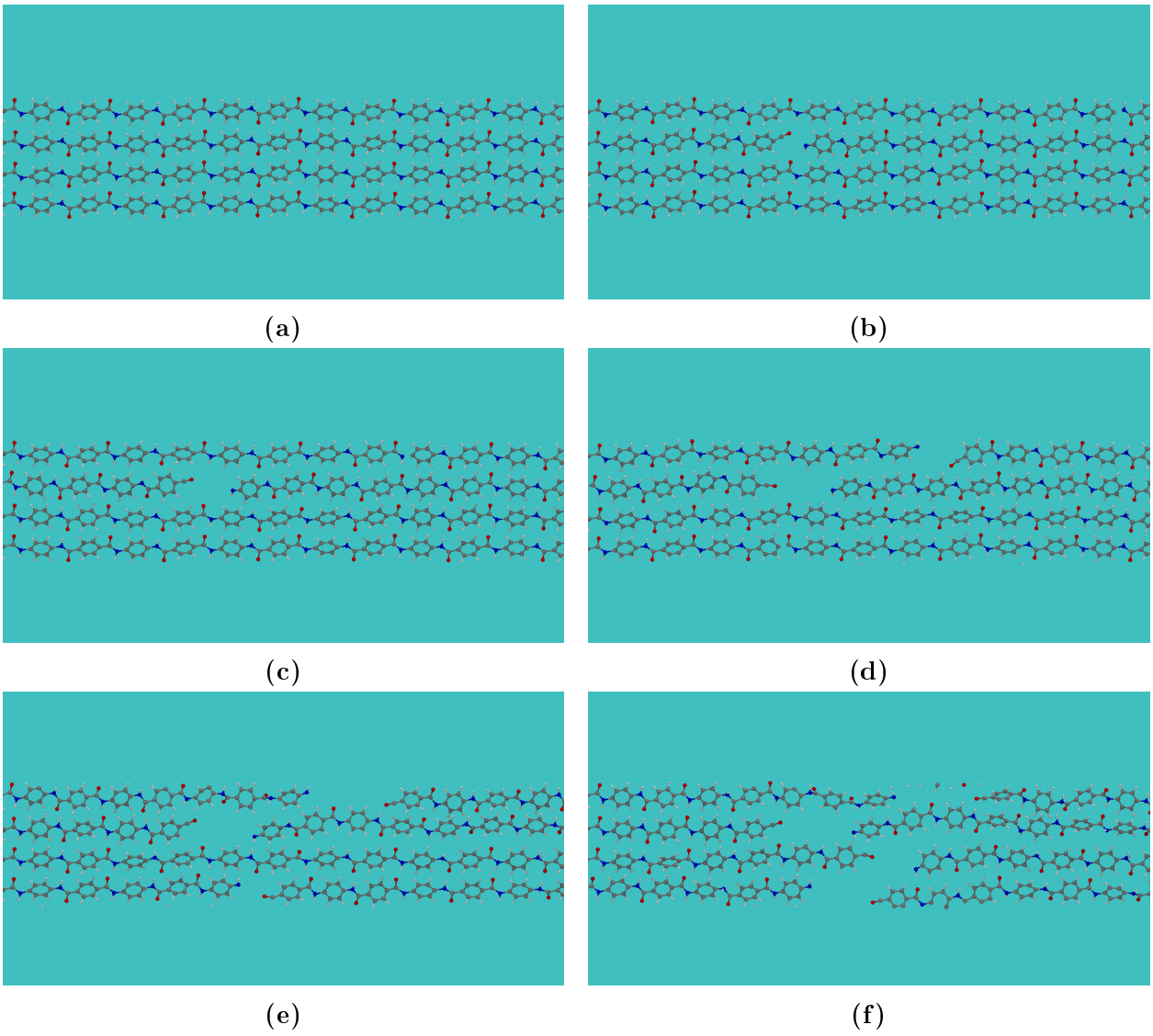

Figure 5.1: *Progression of bond ruptures in a crystalline sheet of PPTA. Figure (a) shows the sheet before bond failure. Figure (b) shows the initial bond failure site. In Figure (c), the broken chain "snaps" as the potential energy in the bond is released as kinetic energy; this results in broken hydrogen bonds between the broken chain and adjacent chains. In Figures (d)–(f), the remaining chains fail one by one in rapid succession.*

This relatively large zone of influence quickly disrupts the load-carrying capacity of the sheet, and subsequent primary bond ruptures quickly follow, causing sheet failure almost immediately following the initial primary bond rupture. In the 8×8×64 unit cell system, a single bond rupture disrupts a smaller overall volume fraction of the crystal structure in the simulation cell, allowing surrounding primary bonds to remain intact for a longer period of time. Hence, it is important to consider the influence of periodic boundary conditions

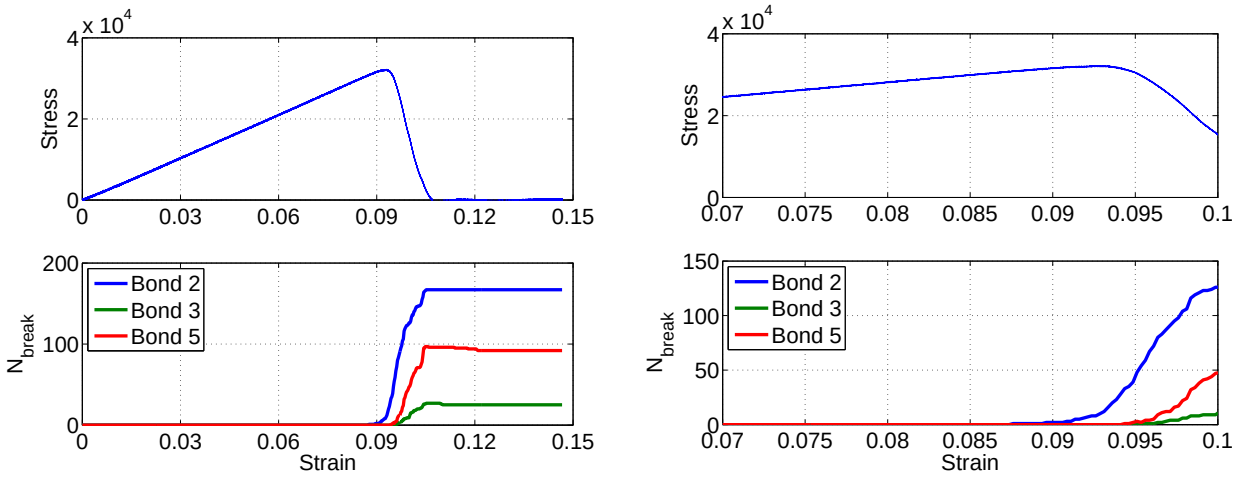

Figure 5.2: *An 8×8×64 perfect crystal system is strained at a rate of* $\dot{\epsilon} = 1.0 \times 10^9\ s^{-1}$. *The zoomed-in view in (b) highlights that multiple bonds break before the stress reaches its maximum value and begins to drop.*

and system size on the behavior of primary bond ruptures in crystalline PPTA – in general, models of larger systems will be less susceptible to failure induced by isolated primary bond ruptures.

5.2.2 Primary bond failure rate at constant strain and temperature conditions

So far, the behavior of bond ruptures during constant strain rate loading has been examined, but a more fundamental look at the bond rupture process entails examining what happens when the system is held at a fixed level of strain. Indeed, the kinetic theory of fracture (KTOF) [75, 82, 83] predicts that the rate of bond rupture in a solid at fixed stress and temperature is constant in time and given by

$$\lambda = \omega_0 \exp\left[\frac{-U_0 + \gamma\sigma}{k_b T}\right] , \tag{5.17}$$

where ω_0 represents the bond oscillation frequency, U_0 is the bond activation energy, T is the absolute temperature, k_b is the Boltzmann constant, σ is the stress (taken to be equal to $E\epsilon$ for linear elasticity, where E is the Young's modulus and ϵ the strain), and γ is a material constant. While this equation is intended to pertain to a system whose bond behavior is homogeneous, such that the continuum mechanical strain ϵ is indicative of a bond's level of stretch, the strain parameter should truly apply to bonds on an individual level. Consider, for example, a system of crystalline PPTA with chain-end defects. As demonstrated in the zone of influence study of Section 4.2.1, the stretch of the links near the defect site changes

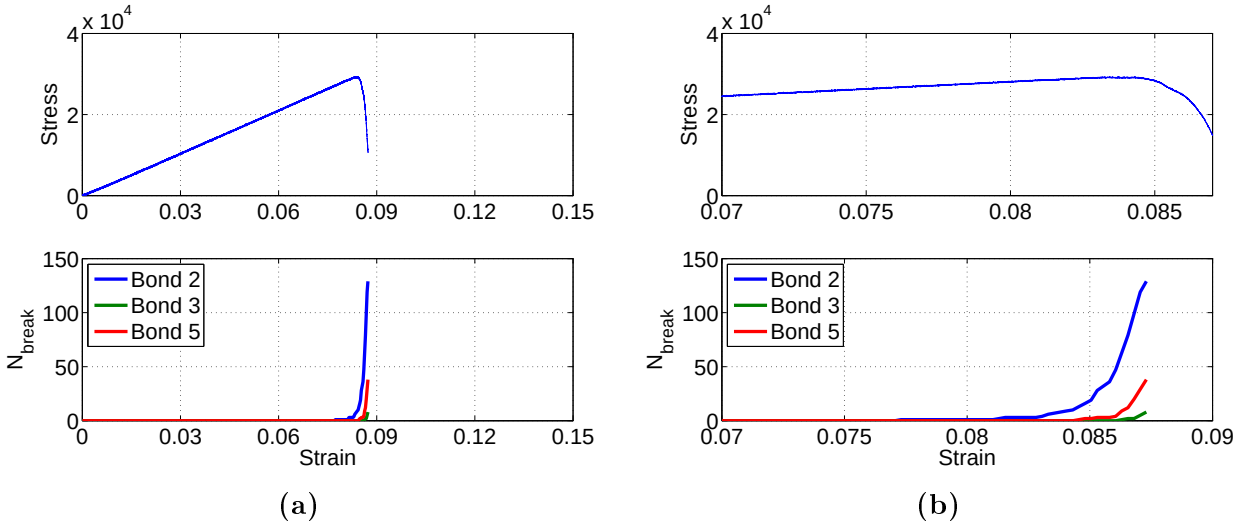

Figure 5.3: *An 8×8×64 perfect crystal system is strained at a rate of* $\dot{\epsilon} = 2.0 \times 10^8\ s^{-1}$. *The zoomed-in view in (b) highlights that multiple bonds break before the stress reaches its maximum value and begins to drop.*

relative to the stretch of the links in a perfect crystal at an equivalent crystal cell strain, and these local deviations in stretch reflect location-dependent failure rates of the bonds due to the presence of defects in the crystal – relaxed links contain bonds that are less likely to fail, and links that take on additional stretch contain bonds which are more likely to fail.

The simulations presented in this work offer strong evidence that the failure of primary bonds is stochastic in nature, which implies that covalent bonds have a probability of failure per oscillation, or equivalently, a failure rate that represents a probability of failure per unit time. The probability of bond rupture increases with increasing bond stretch and system temperature, since higher levels of stretch bring a bond closer to a bond's critical length, and higher temperatures lead to larger fluctuations in bond length. Therefore, it is reasonable to think of bonds as having a failure rate that is constant in time and which depends on the state of stretch of the bond and the temperature of the system in which the bond exists.

For the case where all bonds of the same type are expected to behave in a statistically identical manner, such as in a perfect defect-free crystal, the crystal strain can be used as a metric to indicate bond stretch. Therefore, the failure rate of individual bonds can be characterized by the crystal strain and system temperature, rather than by individual bond strain levels. Furthermore, in such a defect-free crystal, all bonds of the same type will exhibit statistically identical properties (e.g., average level of stretch and fluctuation amplitude), which means they will share the same failure rate as well. However, these identical statistical properties will only be maintained until the first bond rupture in the system. After this first rupture, bonds near the rupture site will take on higher or lower states of stretch, depending on their location relative to the rupture site, and from this point onward, individual bonds will exhibit a unique probability of failure relative to other bonds

in the system.

Working under the assumption that, at fixed strain and temperature, all bonds of a given type have the same failure rate until the onset of first bond failure, an analogy can be made between primary bonds undergoing thermal fluctuations in a perfect PPTA crystal and a population of components operating in time until their eventual failure. Consider a population of N components which are identical to one another and behave independently of one another. Suppose these components are all simultaneously put into operation at time $t = 0$ and that each component has a constant failure rate λ_0. Further assume this failure rate is currently unknown, and it is desired to compute it. To calculate λ_0, one would record the time to failure for each component t_i for $i = 1, ..., N$, and then compute the mean time to bond failure μ_0 as

$$\mu_0 = \frac{1}{N} \sum_{i=1}^{N} t_i \ . \tag{5.18}$$

Then, the bond failure rate λ_0 is calculated according to (5.15) as

$$\lambda_0 = \frac{1}{\mu_0} \ . \tag{5.19}$$

This calculation assumes that the failure rate λ_0 is constant in time. The property of constant failure rate can be verified by examining a histogram of the distribution of observed times to failure t_i. If the failure rate were indeed constant, then the distribution of failure times would follow the exponential distribution, as derived in equation (5.13). As long as the observed failure times were distributed according to the exponential distribution, equation (5.19) would represent a correct method for calculating failure rate of an individual component from the distribution of failure times. The accuracy of the calculation relative to the true failure rate would improve with larger sample size N, since the standard error in the estimate of the mean time to failure is $\frac{\sigma_0}{\sqrt{N}}$, where σ_0 is the standard deviation of the mean time to failure of the components in the sample.

This population of independently-behaving components with constant failure rates is analogous to primary bonds undergoing thermal fluctuations in a perfect crystal: bonds in the crystal can be assumed to be intact at some starting time ($t = 0$ without loss of generality), and bonds of the same type can be assumed to behave statistically identically to one another as they fluctuate in time, leading to equivalent failure behavior among bonds of the same type, as previously discussed. There is, however, one major difference between the primary bonds in the crystal and the hypothetical population of components, which is that after one bond in the system fails, the failure rate of bonds near the failure site will change, as they change their level of stretch in response to both the newly introduced chain break and the dynamic snapping of the PPTA chain as primary bond potential energy is converted into kinetic energy. Hence, the failure rate and probability of rupture depend on proximity to the initial failure site and are not constant from the moment the first bond in the system fails. This means that the failure rate of bonds after the first break change in

time and cannot be measured by computing the mean time to failure of the remaining bonds in the system as in equation (5.18).

There is, however, an alternative method to calculating the bond failure rate as follows: consider K samples of crystals each containing N bonds. Suppose each sample begins with all bonds intact and with different initial conditions at time $t = 0$, such that the initial conditions at time $t = 0$ are the only difference between each of the K samples. Each sample is allowed to undergo thermal vibration in time until the first bond failure occurs, and the time to first failure for each sample is recorded as t_{f_i} for $i = 1, ..., K$. Then, the mean time to first failure for the system of N bonds can be calculated as

$$\mu_N = \frac{1}{K} \sum_{i=1}^{K} t_{f_i} \ . \tag{5.20}$$

The failure rate for the system, which can be thought of the rate of occurrence of first bond failure for a collection of many identical systems of N bonds, is

$$\lambda_N = \frac{1}{\mu_N} \ . \tag{5.21}$$

The final step is to take the failure rate of the system λ_N and convert it to the failure rate of an individual bond λ_0. To do this, consider that a system of N bonds is considered failed as soon as the first bond fails. In addition, it is assumed that the behavior (and therefore failure) of each bond is independent of one another before this first failure occurs. Under these assumptions, the system can be thought of as a series-collection of independently-operating components, and the failure rate for such a system is the sum of the failure rates of each individual component [32]. Since each component is assumed to have the same failure rate λ_0, this leads to the relation

$$\lambda_N = \sum_{i=1}^{N} \lambda_i = N\lambda_0 \ . \tag{5.22}$$

With the preceding concepts in mind, a series of simulations is now run to explore the true nature of primary bond failure rate at fixed strain and temperature conditions. In all strain-to-failure simulations performed in this work, it is observed that Type 2 bonds (as labeled in Figure 3.2) always fail first, with bond failures of types 3 and 5 occurring only after a substantial number of Type 2 bond failures have occurred. Hence, the "component" of study in perfectly crystalline PPTA is identified as all Type 2 bonds in the system.

First, it is desired to verify the nature of the failure rate of Type 2 bonds in the crystal. If the failure rate at fixed strain and temperature is not constant in time (prior to first bond rupture), it implies that the failure of a bond depends on its history of operation. This is not physically representative of a bond whose failure criteria is determined by chemical bond order (which depends on interatomic distance and has no notion of history), so it is anticipated that the failure rate will indeed be constant. To verify this, two sets of

simulations are performed. The first begins with a simulation cell consisting of 3×4×2 perfectly crystalline unit cells modeled with the ReaxFF force field. This is the smallest simulation cell that can be modeled that ensures that the smallest rectangular simulation cell dimension is larger than twice the cutoff distance per the minimum image convention ($r_c = 10$ Å as discussed in Chapter 3). The simulation cell is brought to an axial strain of $\epsilon = 0.095$ and then subjected to an NPT thermostat which maintains an average temperature of 300 K and zero pressure on the lateral faces of the simulation cell. This is therefore representative of crystalline PPTA at fixed strain and temperature conditions. 400 variants of this configuration are created by randomly assigning 400 different initial velocity conditions to the initial configuration, ensuring that the velocity magnitudes are scaled to yield a temperature of 300 K. Each of the configurations with unique initial velocity conditions is ran for as long as is necessary to observe the first bond failure event in the system. The second set of simulations is identical to those just described, with the only difference being that a larger simulation cell consisting of 4×4×8 perfectly crystalline unit cells is used. In each set of simulations, the distribution of times to first failure for each configuration $i = 1, ..., K = 400$ is recorded. Each simulation is given a short period of time to equilibrate (10,000 fs is found to be sufficient), and the time to first bond failure is recorded as the time elapsed after this initial equilibration period. In cases where bonds rupture during the equilibration phase, a different set of initial velocity conditions are assigned until survival of all bonds past 10,000 fs is achieved.

The results of the two sets of times to first failure data gathered from the simulations are presented in Figures 5.4 and 5.5. The figures show that the distributions of times to first failure closely resemble the exponential distribution, which supports the hypothesis that the bond failure rate in each system is constant in time. The quantitative results of the simulations are also summarized in Table 5.1. The table highlights that the single bond failure rates in each system are different from one another, and that this difference is not likely accounted for by the 95% confidence interval for the estimate of the failure rate in each system. This result does not agree with the assumption made at the outset of this investigation, which is that bonds behave independently of one another, since this assumption implies that the individual bond failure rates are independent of system size, or equivalently, that the system failure rate λ_N is related to the single bond failure rate λ_0 through equation (5.22). This discrepancy in computed single bond failure rates may be due to the fact that in the relatively small systems considered here, the individual bonds in a given chain may not behave completely independently of one another. Consider for example that the overall length of the chain is fixed since the system is operating at fixed axial strain. Therefore, the sum of the bond lengths (projected onto the z-axis) along the chain is constrained to equal the length of the simulation cell, such that bonds may not take arbitrary lengths at any given moment in time. It is likely that if the times to first bond failure were recorded for increasingly large systems that the value of λ_0 would eventually converge to a fixed value. However, due to the prohibitive cost of performing these simulations on such large systems, this investigation is not pursued here. Regardless of the accuracy of the calculation of the failure rate for a single bond in these perfectly crystalline systems, the

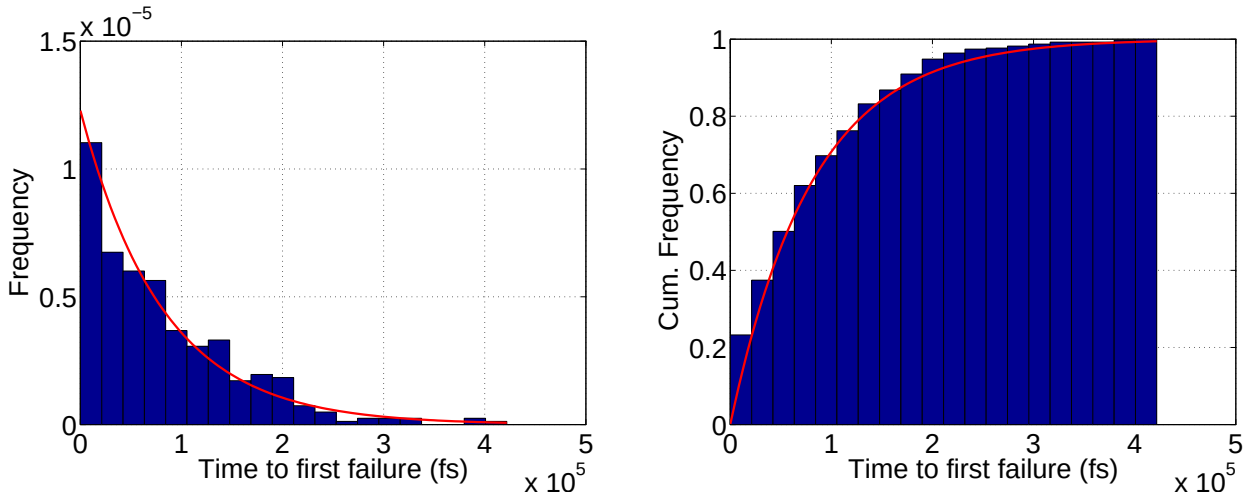

Figure 5.4: *The distribution of times to first failure for the 3×4×2 system. The red curve is the exponential distribution with* $\lambda_N = \frac{1}{\mu_N}$*, where* μ *is the average time to first failure among the 400 simulations.*

exponential distributions displayed in Figures 5.4 and 5.5 indicate that the bond failure rate in these systems is constant at fixed strain and temperature. It is interesting to note that this is the same prediction made by the kinetic theory of fracture through equation (5.17), and therefore, the MD simulations agree with theoretical considerations for the rate of bond failure in solids.

System	N	μ_0 ($\times 10^{-15}$ s)	λ_0 ($\times 10^{8}$ s^{-1})	95% CI ($\times 10^{8}$ s^{-1})
3×4×2	96	$81,300 \pm 3720$	1.28	1.17–1.41
4×4×8	512	$12,600 \pm 661$	1.55	1.40–1.73

Table 5.1: *The failure rate of a single bond* λ_0 *is calculated based on the mean time to first failure* μ_0 *for the simulation data presented in Figures 5.4 and 5.5. The 95% confidence interval for the estimated value of* λ_0 *is shown in the final column.*

It is also of interest to see how the MD simulations predict a change in bond failure rate with a change in strain or temperature. To explore this, a set of simulations of the variety which produced the results displayed in Figures 5.4 and 5.5 are performed for a set of strains and temperatures of interest. Strain and temperature combinations are chosen to encourage bond failures to occur relatively quickly, otherwise, the simulations take prohibitively long to run before the first bond failure is observed. Each set of simulations at fixed strain and temperature generates a set of times to first failure, from which the individual bond failure rate is computed. Here, each set of simulations uses a system of 3×4×2 unit cells of perfectly crystalline PPTA and 200 variants on initial velocity conditions to generate the data points

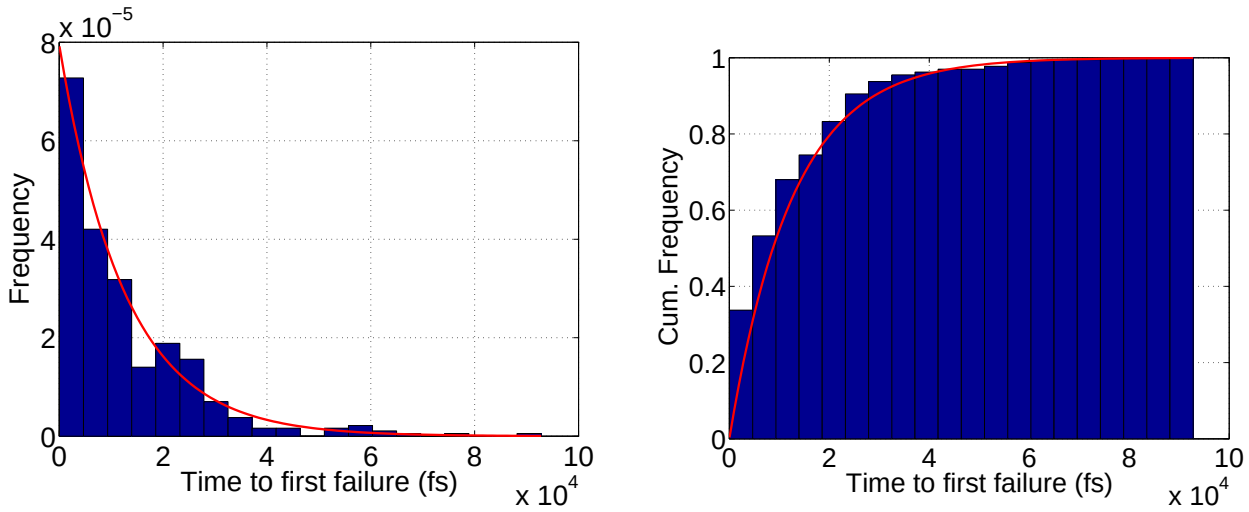

(a) **(b)**

Figure 5.5: *The distribution of times to first failure for the 4×4×8 system. The red curve is the exponential distribution with* $\lambda_N = \frac{1}{\mu_N}$*, where* μ *is the average time to first failure among the 400 simulations.*

(with the exception of $\epsilon = 0.095$ and $T = 300$ K, which has already been presented and uses 400 initial condition variants). Using more than 200 simulations per strain/temperature combination would increase the accuracy of the failure rate calculations, but is prohibitively expensive.

The results of the relationship between failure rate and strain, and failure rate and temperature, are displayed in Figures 5.6 and 5.7, respectively. As anticipated, the bond failure rate has a strong dependence on both crystal strain and temperature. The curves displayed along with the raw data in Figures 5.6 and 5.7 are computed by finding the parameters from the kinetic theory of fracture equation (5.17) which best fit the data – this is done in order to observe how well the kinetic theory of fracture describes the change in bond failure rate with strain and temperature computed in the MD simulations. Specifically, for the case of fixed temperature and varying strain, equation (5.17) predicts the following relationship between bond failure rate and strain:

$$\lambda = A \exp\left[a\epsilon\right] \ , \tag{5.23}$$

where $A = \omega_0 \exp\left[\dfrac{-U_0}{k_b T}\right]$ and $a = \dfrac{\gamma E}{k_b T}$ are taken as constants. Here, it has been assumed that the relation between stress and strain is linearly elastic in nature, such that $\sigma = E\epsilon$, which closely describes the stress-strain relationship for PPTA crystals, as discussed in Chapter 4. On the other hand, consider the case of fixed strain and varying temperature. Then,

equation (5.17) can be written as

$$\lambda = \omega_0 \exp\left[\frac{b}{T}\right] \ , \tag{5.24}$$

where $b = \dfrac{-U_0 + \gamma E \epsilon}{k_b}$ and is assumed to be negative (else the strain would be high enough to overcome the activation energy U_0 and bond rupture would immediately ensue). If b is negative, then an increase in temperature leads to a less negative exponent in equation (5.24), and the failure rate increases with increasing temperature.

From these curve fits, the parameters of equation (5.17) are calculated to be $U_0 = 80.6$ kJ/mol, $\gamma = 2.45$ Å^3, and $\omega_0 = 3.6 \times 10^{13}$ Hz. These values of the parameters are in line with typical ones observed in experimental data [83, 61]. The activation energy U_0 is somewhat low (covalent bond energies typically range from 100–300 kJ/mol), but the activation volume γ is of reasonable magnitude. In addition, the frequency ω_0 is close to the bond oscillation frequency of approximately 5×10^{13} Hz observed for Type 2 bonds in the MD simulations. These numbers are not meant to be interpreted as accurate estimates of the parameters in equation (5.17) in the sense that the measurements taken to obtain them are relatively few and somewhat inaccurate (due to the need for large numbers of simulations to get tight bounds on an estimate of the bond failure rate). However, the fact that (5.17) can be fit to the MD observations, and that this fit yields physically reasonable parameters for the activation energy, activation volume, and bond frequency is a good indication that primary bond failure in these systems is well-described by the kinetic theory of fracture.

5.2.3 A model for primary bond failure under constant strain rate loading

Using the insights and data gathered with respect to the failure behavior of primary bonds in crystalline PPTA, a model is now proposed for predicting the strain at which the onset of primary bond failure occurs in crystalline PPTA. The objective of the model is to predict the onset of bond rupture in PPTA without needing to run costly MD simulations to do so. The model allows for the exploration of failure behavior at slow strain rates and large crystal sizes that are too costly to practically simulate using molecular dynamics.

The concepts in reliability theory discussed in Section 5.1 are used as the basis of the model to predict primary bond failure. It is assumed that a primary bond in a perfect PPTA crystal has a failure rate $\lambda_0(\epsilon, T)$ that is a function of the crystal strain ϵ and temperature T. The crystal is assumed to begin at an initial strain level ϵ_0 and temperature T_0 with all bonds intact, and in the general case is taken through a time-dependent deformation history described by $\epsilon(t)$ and time-dependent temperature history given by $T(t)$. In this case, the failure rate of the bond may be written explicitly as a function of time:

$$\lambda_0(\epsilon(t), T(t)) = \hat{\lambda}_0(t) \ . \tag{5.25}$$

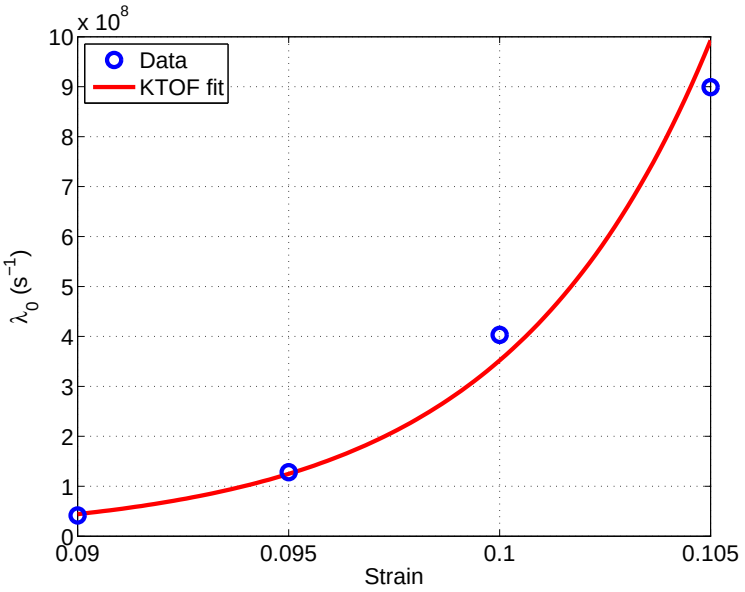

Figure 5.6: *Relation between failure rate λ_0 and strain obtained from ReaxFF MD simulations performed at a temperature of $T = 300$ K.*

Hence, bonds in a crystal subjected to time-dependent strain loading and temperature history can be thought of as having a time-dependent hazard rate function $\hat{\lambda}_0(t)$. If the function $\hat{\lambda}_0(t)$ is known, then the reliability theory concepts discussed in Section 5.1 can be used to compute useful quantities such as, for example, the mean time to bond failure through equation (5.8). The mean time to failure can be used to compute the expected strain at which bond failure occurs by evaluating $\epsilon(t = \mu)$, the strain at the anticipated mean failure time μ.

It is important to realize that the failure rate of a primary bond in crystalline PPTA is only easily predictable up to the moment of first bond failure. After initial bond rupture, the conversion of bond potential energy into kinetic energy and the subsequent distortion of crystal structure near the bond rupture site make it difficult to predict how the failure rates of the rest of the bonds in the system will change. This means that the model may only reliably predict the onset of initial bond failure in a perfect crystal. In Figure 5.8, the strain at first bond failure for runs performed at several strain rates and temperatures is displayed. The corresponding failure strain data (rather than first bond failure data) for each run has been previously presented in Figure 4.10.

In order to evaluate how well the model is capable of performing, a functional form for $\lambda_0(\epsilon, T)$ is postulated, and then calibrated to the strain at first failure data presented in Figure 5.8. Thus far, all observations gathered from MD simulations of primary bond failure in crystalline PPTA are consistent with the basic tenets of the kinetic theory of fracture, including the behavior of the bond failure rate as given by equation (5.17). Therefore, the functional form used for the bond failure rate function is adapted from equation (5.17) and

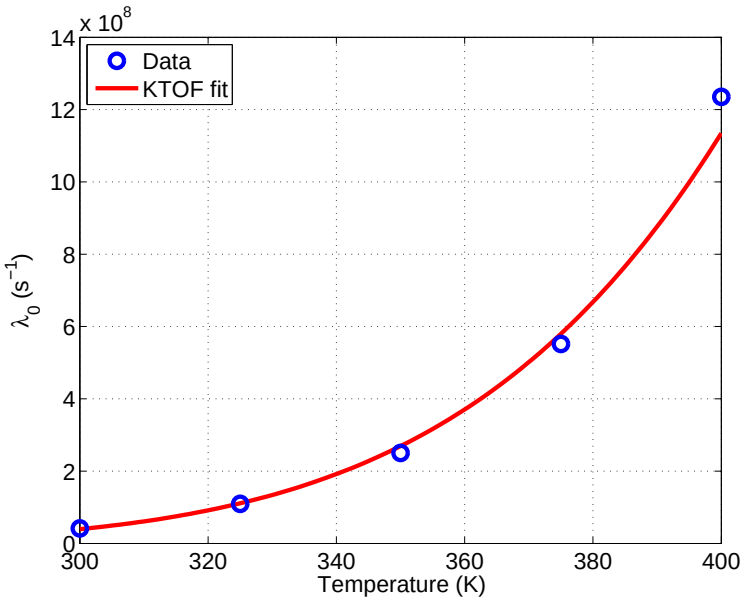

Figure 5.7: *Relation between failure rate λ_0 and temperature obtained from ReaxFF MD simulations performed at a strain $\epsilon = 0.090$.*

converted into a three-parameter form given by

$$\lambda_0(\epsilon, T) = \exp\left(a\frac{1}{T} + b\frac{\epsilon}{T} + c\right) \ , \tag{5.26}$$

where the parameters a, b, and c are constants. Given a strain rate loading history $\epsilon(t) = \dot{\epsilon}t$ at a fixed temperature T, this defines a time-dependent failure rate function

$$\hat{\lambda}_0(t, \dot{\epsilon}, T) = \exp\left(a\frac{1}{T} + b\frac{\dot{\epsilon}t}{T} + c\right) \tag{5.27}$$

which also depends on the strain rate of loading $\dot{\epsilon}$ and system temperature T, which are taken as constant during the loading. For a crystal of N bonds, the failure rate function used is $\hat{\lambda}_N(t, \dot{\epsilon}, T) = N\hat{\lambda}_0(t, \dot{\epsilon}, T)$, and following equation (5.5), this defines a survival function for the system as

$$S(t, \dot{\epsilon}, T) = \exp\left[-\int_0^t \hat{\lambda}_N(x, \dot{\epsilon}, T)dx\right] \ . \tag{5.28}$$

With the survival function defined, the mean time to first bond failure can be calculated according to equation (5.8) as

$$\mu_N(\dot{\epsilon}, T) = \int_0^\infty S(t, \epsilon, T)dt \ , \tag{5.29}$$

and the failure strain at first bond failure is then equal to

$$\epsilon^f = \epsilon(t = \mu_N) = \dot{\epsilon}\mu_N \ . \tag{5.30}$$

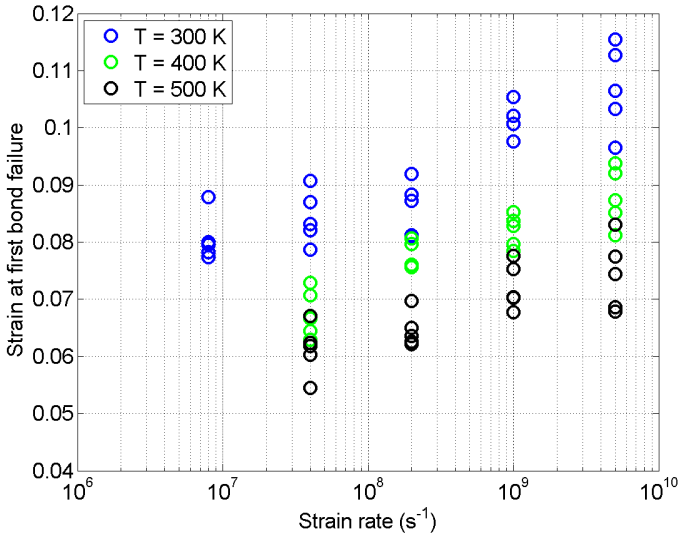

Figure 5.8: *Strain at first failure for runs at several strain rates and temperatures using a simulation cell consisting of 4×4×8 unit cells of perfectly crystalline PPTA.*

With the functional form set according to equation (5.26), it is now desired to find the vector of parameters $\mathbf{x} = (a, b, c)$ which best fit the data of strain at first bond failure shown in Figure 5.8. To determine a suitable vector of parameters $\mathbf{x}$, a numerical procedure is used to minimize an objective function which defines the error between the strain at first bond failure data points in Figure 5.8 and the model's predicted strain at first failure computed from equations (5.29) and (5.30). The objective function is defined as

$$\Phi = \left[\sum_{i}^{N_{data}} \epsilon_i^f - \dot{\epsilon}_i \mu_N(\dot{\epsilon}_i, T_i) \right]^2 , \tag{5.31}$$

where ϵ_i^f is observed strain at first bond failure for data point i in Figure 5.8 and $\mu_N(\dot{\epsilon}_i, T_i)$ is the mean time to first failure computed using equation (5.29) at strain rate $\dot{\epsilon}_i$ and temperature T_i.

The results of the fit are displayed in Figures 5.9–5.11. The strain at first failure data displayed in the figures are taken directly from Figure 5.8. The figures show that the fitted parameters are a reasonably good fit for the data, especially when the error bars are taken into account. Note that the error bars are computed as the square root of the variance as given in equation (5.10) – that is, the error bars come from reliability theory rather than the kinetic theory of fracture or standard error in the data, and the fact that they coincide reasonably well with the spread in observed times to first failure is indicative that the reliability theory model describes the failure process accurately. The parameters a, b, and c obtained from the fit to the kinetic theory of fracture parameters from equation (5.17) yield values of $U_0 = 114$kJ/mol, $\gamma = 4.40$ Å^3, and $\omega_0 = 4.0 \times 10^{13}$. These parameters are

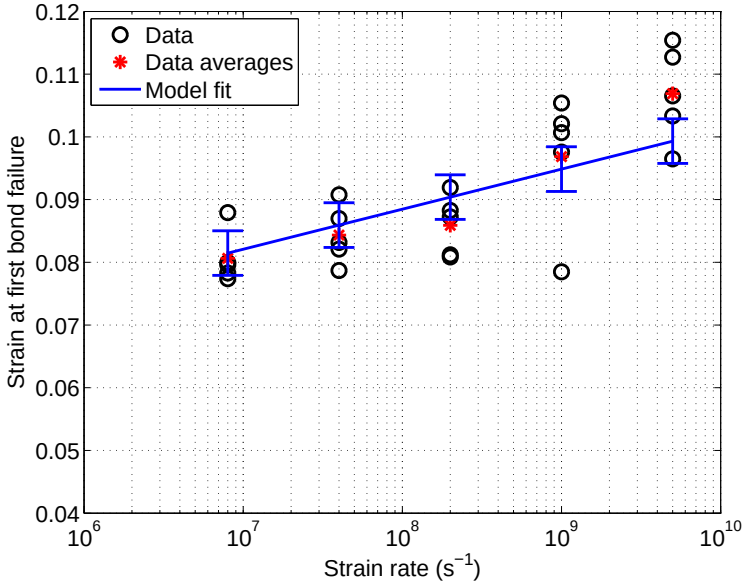

Figure 5.9: *Model fit to first failure data at 300 K.*

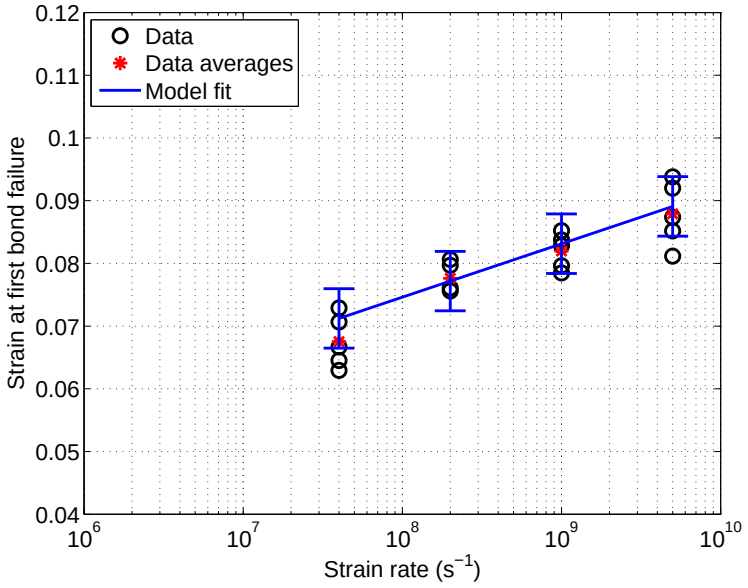

Figure 5.10: *Model fit to first failure data at 400 K.*

different than those obtained from fitting the data in Figures 5.6 and 5.7 to the kinetic theory of fracture equation (5.17), but they are reasonably close to one another, and once again represent physically reasonable values for those parameters, indicating that the modeling approach taken here yields reasonable results.

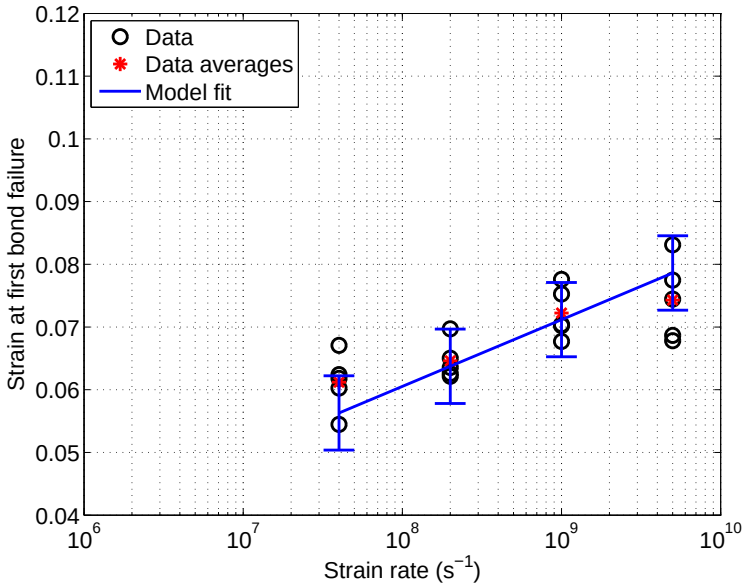

Figure 5.11: *Model fit to first failure data at 500 K.*

5.3 Secondary bond failure in crystalline PPTA

Secondary bond failure also plays an important role in the failure of crystalline PPTA. The nature of secondary bond failure is quite different from that of primary bond failure. The biggest difference is that secondary bonds fail via chain slippage, and therefore secondary bond failure cannot occur under axial loading unless there are chain-end defects or recently-broken primary bonds which allow chain sliding to occur. Here, the failure of secondary bonds in crystalline PPTA is examined in further detail.

5.3.1 Observations of secondary bond failure behavior in MD simulations

As with the case of primary bonds, a representative visualization of hydrogen bond failure within a single sheet is presented in Figure 5.12. The system under consideration is a 4×4×8 array of unit cells with one chain-end defect per chain (Variant IV from Chapter 4) stretched at a strain rate of 1.0×10^9 s^{-1}and modeled with the ReaxFF force field. As noted in Chapter 4, no primary bond failure occurs in this case, which makes it possible to observe how sheet failure occurs when only hydrogen bonds are involved. In Figure 5.12, it can be seen that not all hydrogen bonds in the system fail, but rather, a particular path is traversed through the system. In this particular case, the hydrogen bonds that break traverse a path through the sheet that leads to the fewest number of hydrogen bond ruptures, and this can be likened to a crack forming in the crystal and growing along the path of least resistance. It is important to note that when this simulation is repeated multiple times with different initial

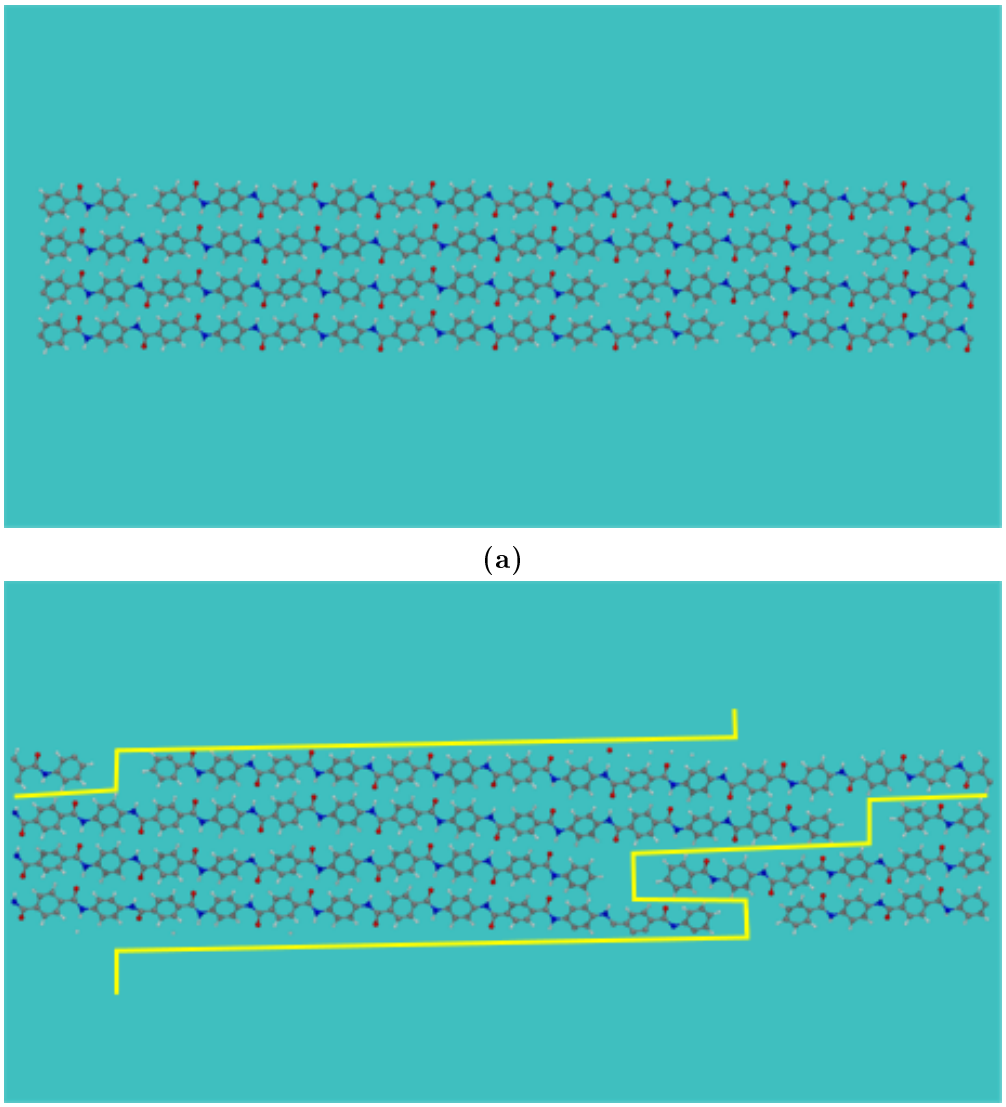

(a)

(b)

Figure 5.12: *Failure of a single sheet in a model consisting of 4×4×8 unit cells with one chain end per cell positioned randomly within the sheet. Figure (a) presents the sheet at zero strain, and Figure (b) shows the sheet in its failed state. The failure path is highlighted in yellow. Surrounding periodic cell replications (due to periodic boundary conditions) are not shown.*

conditions, not every simulation features sheets which fail via the path of least resistance. This may seem counterintuitive, but it is reflective of the stochastic nature of bond failure in the system – the path of fewest hydrogen bond breaks is the most likely path to be taken, but is not necessarily the path that is always taken.

In order to better understand how hydrogen bond failure occurs in PPTA crystals with defects, a set of simulations is performed where the chain ends in the crystal are distributed

in specific patterns, rather than randomized as they were in the studies performed with Variants I–IV in Section 4.2.2. Figure 5.13 displays the patterns under consideration. They consist of three specific patterns denoted Pattern A, Pattern B, and Pattern C, as well as set of patterns denoted Pattern D_N where N is an integer parameter whose meaning will be discussed shortly. Each pattern is implemented in a simulation cell of size 3×8×64 unit cells, with the 64-monomer unit cell length intended to ensure the portion of the chains outside the defect band are mostly uninfluenced by the presence of the defects. In each model, the pattern under consideration is applied to each sheet, such that each sheet in the simulation cell is identical to one another. Patterns A, B, and C each have a defect band which spans ±8 monomers relative to a plane bisecting the simulation cell. Pattern D_N is a regular zig-zag pattern of chain-end defects and is chosen in order to systematically explore the influence of the size of the defect band on the failure behavior. The subscript N refers to the size of the defect band, such that defects span a region $\pm N$ monomers about the bisecting plane of the simulation cell for a total separation distance of $2N$ monomers between chain-end defects in adjacent chains. Pattern D_N is simulated using defect band sizes of $N = 1, 2, ..., 8$.

For each pattern under consideration, a set of five strain-to-failure simulations was performed at a strain rate of 1.0×10^9 s^{-1}, and the average failure strain for each set of simulations was recorded. The PCFF force field is used to conduct these simulations in order to ensure that only hydrogen bond rupture occurs in the absence of primary bond rupture. Considering the result of the simulation visualized in Figure 5.12, it is postulated that the failure strain for each pattern depends on the smallest number of hydrogen bonds that must be ruptured for the sheet to fail completely. As such, Figure 5.14 presents the results of the simulations as a plot of the crystal failure strain versus the minimum number of hydrogen bonds that must rupture for failure of each sheet to occur. The figure shows a strong dependence of the failure strain on the number of hydrogen bonds in the most likely break path, up until about 80 bonds in the break path, which corresponds to Pattern D_5. It appears that the failure strain plateaus (or at least increases at a much slower rate) at a failure strain of just under 6% for more than 80 bonds in the break path.

The plateau in Figure 5.14 can be explained by examining the behavior of hydrogen bonds near a chain-end defect, as displayed in Figure 4.13. From the figure, it is observed that hydrogen bonds near the defect site undergo significant stretching within about ±4 monomers of the defect site, which weakens the strength of these bonds relative to that of the other hydrogen bonds in the crystal. For $N \leq 4$, all of the hydrogen bonds in the crystal are within this weakened zone, and the fewer bonds in this zone (lower values of N), the fewer bonds that must fail for failure via chain sliding to occur, which results in a lower failure strain for the sheet. However, for $N \geq 5$, the defect band contains (moving from left to right) a 4-monomer long region of weak hydrogen bonds, a $2(N-4)$-monomer long region of strong hydrogen bonds, and another 4-monomer long region of weak hydrogen bonds. Slippage must initiate at the weak hydrogen bond sites near the chain ends, and therefore, for $N \geq 5$, slippage (and therefore peak stress) occurs at roughly the same crystal strain. Indeed, the strong hydrogen bonds in between the chain-end locations do not improve the strength of the hydrogen bonds near the chain-end sites. In Figure 5.15, the stress-strain

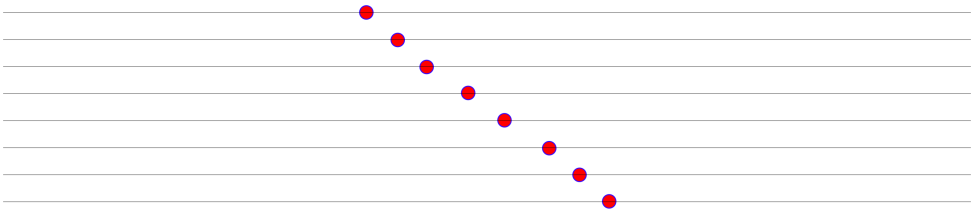

(a) *Pattern A*

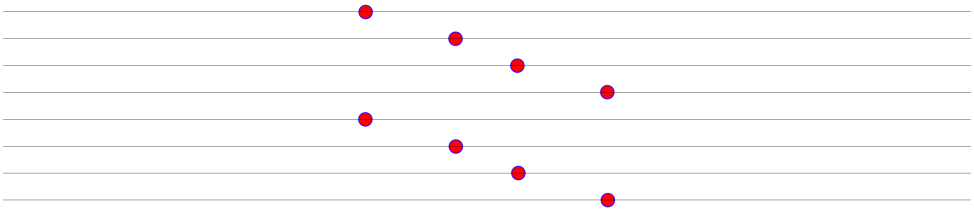

(b) *Pattern B*

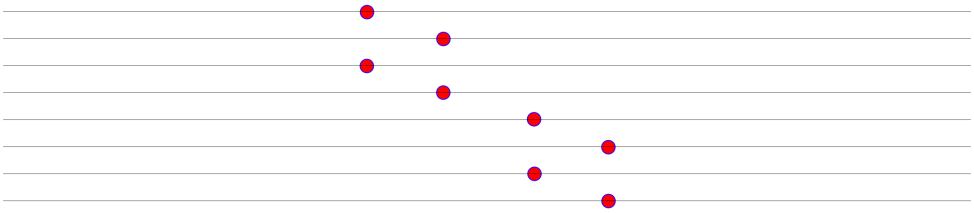

(c) *Pattern C*

(d) *Pattern D_N*

Figure 5.13: *Failure patterns tested in strain-to-failure simulations using the PCFF force field. The red dots represent chain-end locations.*

response for Patterns D_5 and D_8 are presented in order to gain further clarity on the crystal behavior. In both plots, it is seen that the peak stress (and corresponding failure strain) is about the same, with a failure strain of just under 6%. However, the rate of decrease of the stress after achieving peak stress is more rapid for Pattern D_5 than for Pattern D_8. Figures 5.16 and 5.17 visualize the failure of a single sheet for Patterns D_5 and D_8, and it can be seen that the hydrogen bonds in Pattern D_5 fail very quickly after initial hydrogen bond slippage occurs, while the defect-free region in the larger defect band of Pattern D_8 maintains some hydrogen bonds in the defect band up to about 7% strain, prolonging the complete

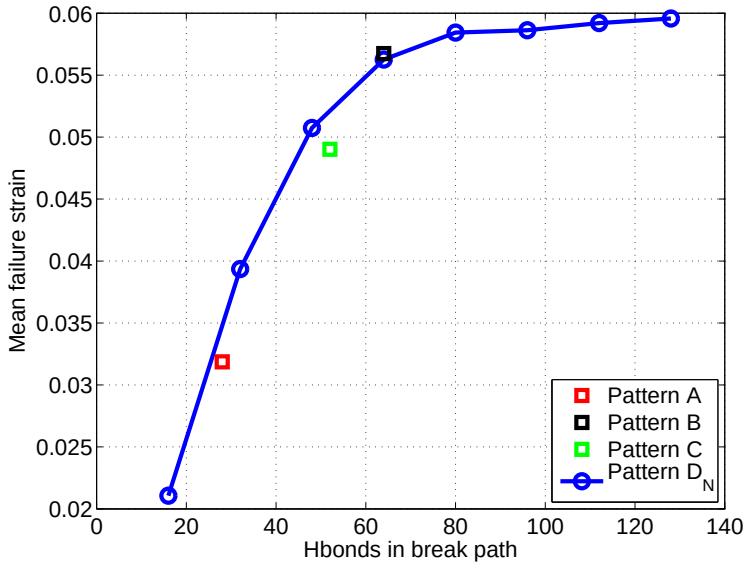

Figure 5.14: *Failure strain versus number of bonds along the shortest path to failure. Each failure strain value is an average over five PCFF simulations performed at a strain rate of* $1.0 \times 10^9\ s^{-1}$.

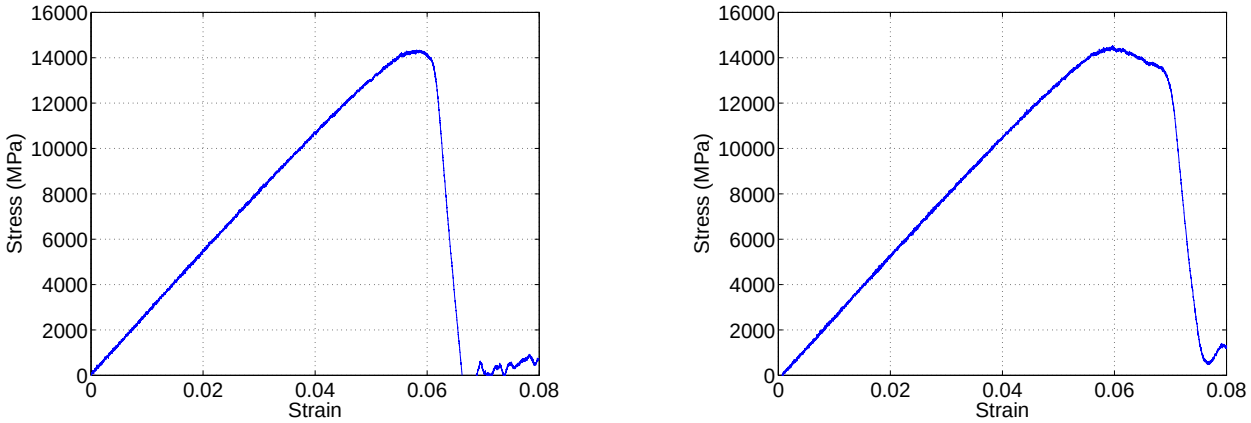

(a) *Pattern* D_5 **(b)** *Pattern* D_8

Figure 5.15: *Stress-strain curves for Patterns* D_5 *and* D_8 *for* $\dot{\epsilon} = 1.0 \times 10^9\ s^{-1}$ *using the PCFF force field.*

slippage of chains in the sheet. This prolonging of complete sheet failure coincides with the region of slow stress decrease in the 6% to 7% strain range for Pattern D_8 in Figure 5.15.

The PCFF simulations presented here do not allow primary bonds to rupture as they do in ReaxFF. So, while PCFF simulations are useful for exploring how hydrogen bond failure occurs and ultimately leads to PPTA sheet failure, they do not necessarily represent the true physical behavior of PPTA sheets with the chain-end location patterns considered here. To investigate this further, simulations of Pattern D_N for $N = 1, 2, ..., 8$ were performed with

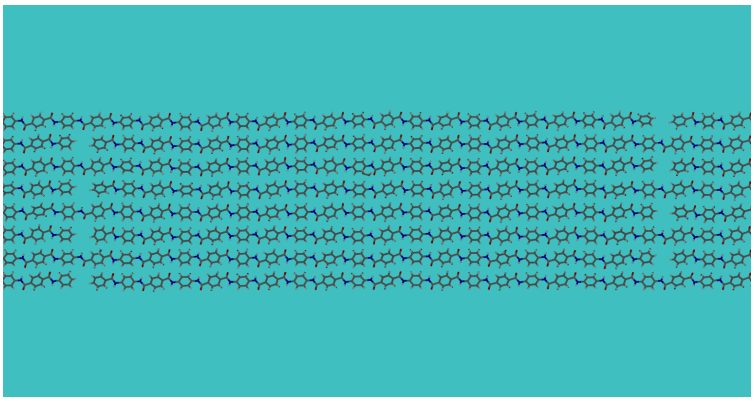

(a) $\epsilon_{zz} = 2.0\%$

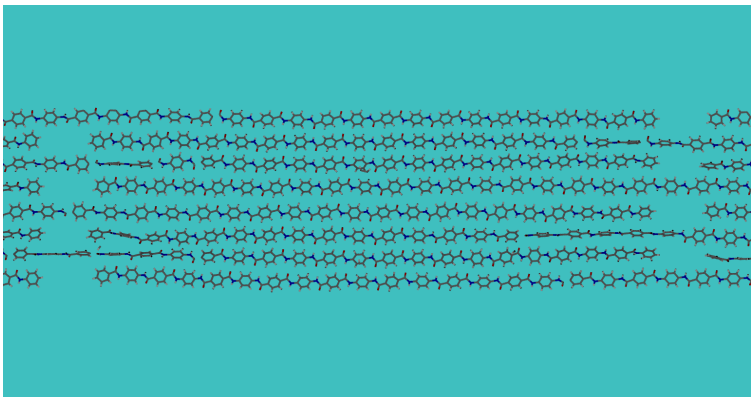

(b) $\epsilon_{zz} = 6.0\%$

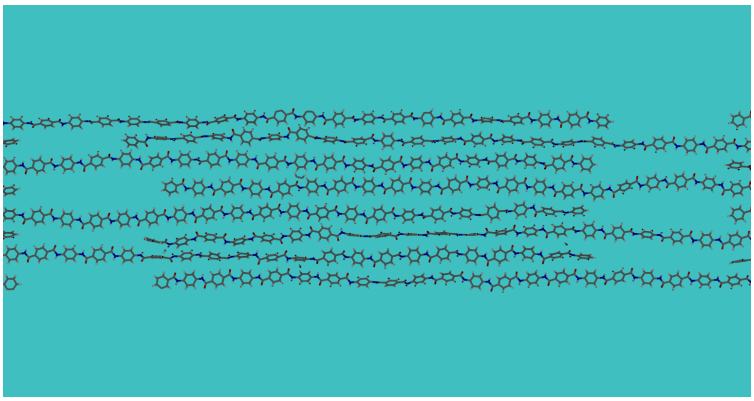

(c) $\epsilon_{zz} = 6.3\%$

Figure 5.16: *Failure of Pattern D_5 with PCFF.*

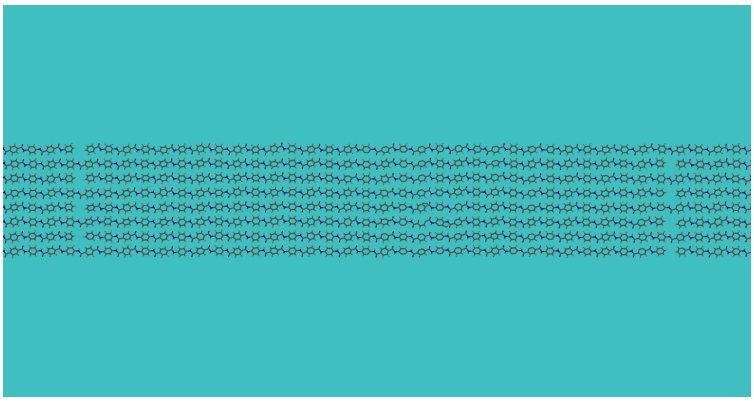

(a) $\epsilon_{zz} = 2.0\%$

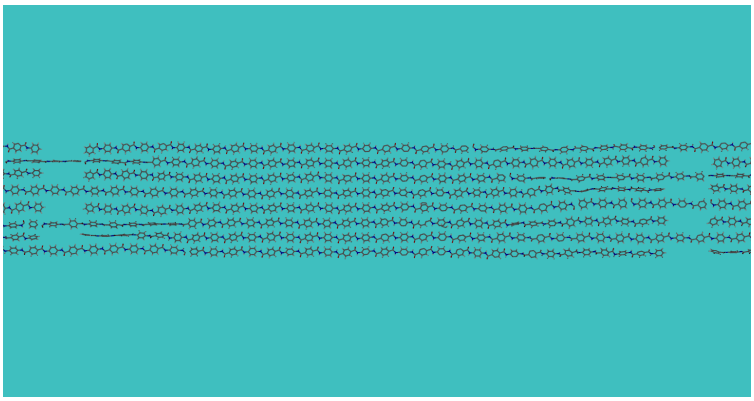

(b) $\epsilon_{zz} = 6.5\%$

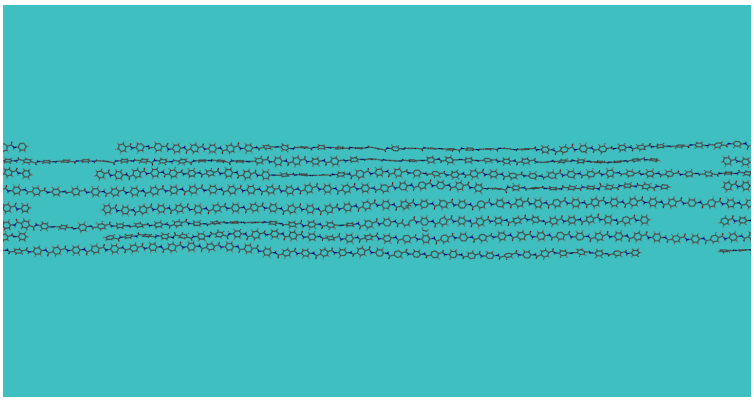

(c) $\epsilon_{zz} = 7.0\%$

Figure 5.17: *Failure of Pattern D_8 with PCFF.*

ReaxFF at a strain rate of 1.0×10^9 s^{-1}. The results showed that failure was initiated by primary bond breakage for $N \geq 4$ when ReaxFF was used. Visualizations of failure in a single sheet for Pattern D_5 and Pattern D_3 are shown in Figures 5.18 and 5.19, respectively. From Figure 5.18, it can be seen that Pattern D_5 fails due to primary bonds which rupture near the chain-end defects in the sheet, leading to bond failures occurring across the weak plane of the system. This failure mode was observed for each of the instances of Pattern D_N with $N \geq 4$. This is consistent with the zone of influence studies performed in Section 4.2.1, where it was observed that links (and therefore primary bonds) adjacent to chain-end defect sites took on additional stretch, therefore making them more likely to rupture. When $N \leq 3$, the hydrogen bonds become substantially weaker due to their proximity to the chain-end defects, and fail in preference to primary bonds as observed in the visualization in Figure 5.19. These results suggest that PPTA crystallite failure most likely occurs by accumulating primary bond breaks until the a large enough concentration of chain breaks congregates across a region of the sheet such that chain sliding becomes the preferred method of failure, at which point the sheet will promptly fail when sufficient strain to break the hydrogen bonds has been achieved.

The failure behavior studies of crystalline PPTA performed here are highly relevant to the failure of true PPTA crystallites. As discussed in Chapter 2, true PPTA fibers consist of crystallites stacked end-to-end with periodically repeating planes of concentrated chain ends. The simulation results obtained here show that unless the defect bands are extremely narrow, spanning about 6 monomers (about 8 nm) in width or less, the strength of the crystallite is not particularly adversely affected by the presence of these bands, with sheet failure occurring at strains no lower than 5% for $N \geq 4$ in Pattern D_N modeled with ReaxFF. Hence, these simulations explain why PPTA fibers retain impressive strength despite the presence of periodic defect bands within the crystallites composing the fibers.

5.3.2 Modeling secondary bond failure near isolated chain-end defects under strain rate loading

As with primary bonds, the failure of secondary hydrogen bonds under strain rate loading is a stochastic event, with the probability of bond failure governed by the temperature and level of stretch of the bond. In Section 5.2.3, it was shown that the failure of primary bonds could be modeled using concepts from reliability theory by treating the bonds as a collection of components with a time-dependent failure rate based on the loading conditions of the crystal. Given the similarities in failure behavior between primary and secondary bonds, it is reasonable to believe that such a model can be applied to secondary bond failure as well. However, hydrogen bonds in crystalline PPTA behave somewhat differently than primary bonds. Hydrogen bonds fail due to sliding between chains within a hydrogen-bonded sheet, which means that hydrogen bonds cannot fail under axial loading of the crystal unless there are chain-ends present to allow sliding between chains. Hydrogen bond failures cannot occur as isolated single bond failures, since for chain sliding to occur, multiple bond failures must

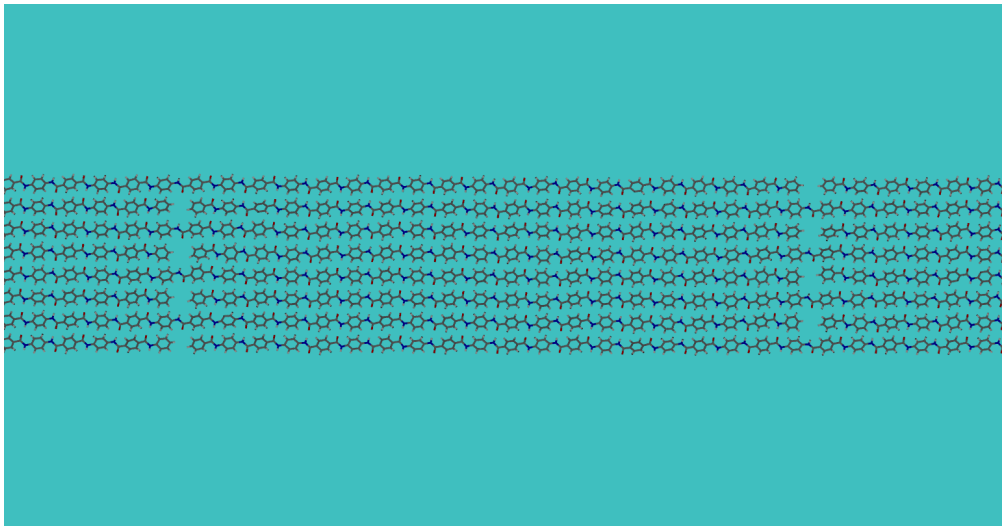

(a) $\epsilon_{zz} = 2.0\%$

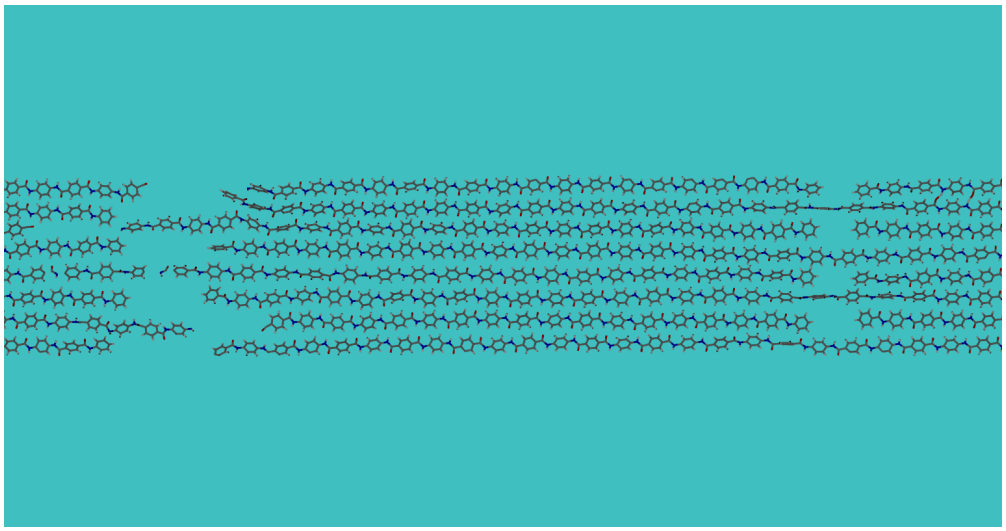

(b) $\epsilon_{zz} = 5.3\%$

Figure 5.18: *Failure of Pattern D_5 with ReaxFF. Primary bond breaks occur near the chain-end defects in the sheet.*

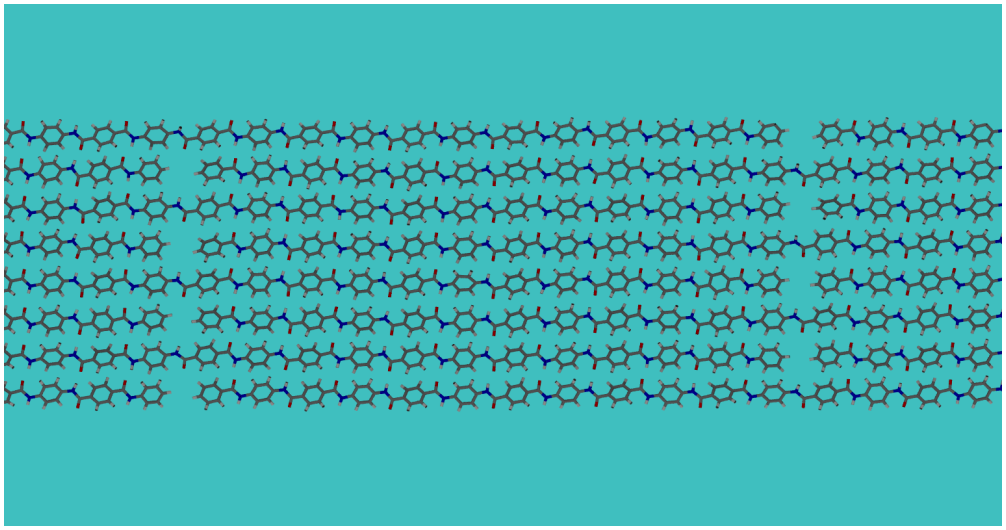

(a) $\epsilon_{zz} = 2.0\%$

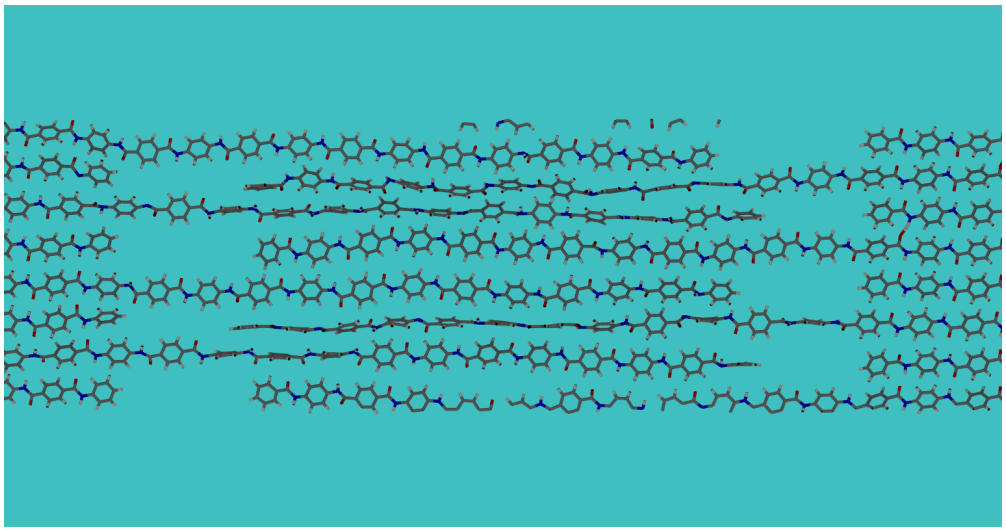

(b) $\epsilon_{zz} = 4.8\%$

Figure 5.19: *Failure of Pattern D_3 with ReaxFF. Primary bonds remain intact, and failure occurs through chain sliding and hydrogen bond failure.*

occur simultaneously. For these reasons, some of the basic assumptions regarding primary bond failure, such as conceptualizing individual primary bonds as independently-operating components with identical failure rates, do not apply to hydrogen bond failure.

Despite these complexities regarding the failure behavior of hydrogen bonds, it is possible to conceive of a chain-end defect distribution whereby the initiation of hydrogen bond failure at the chain-end defect sites can be treated in a very similar way as the failure of individual primary bonds in a perfect crystal. Consider a PPTA crystallite which has a relatively dilute concentration of chain-end defects. Suppose these defects are distributed throughout the crystal such that each defect is sufficiently far from all other defects so that the defects are non-interacting. That is, all the defects lie outside of each other's zone of influence, the region where both primary and secondary bonds alter their level of stretch in response to the presence of a defect, as discussed in Section 4.2.1. In this case, each chain-end defect can be treated as a failure site, and each failure site has a rate of failure, where failure is defined as the initiation of inter-chain slippage at the failure site. The initiation of inter-chain slippage is a somewhat complex event that involves the rupture of several hydrogen bonds near the defect. However, by treating defect sites as independently-operating components within the crystal, with a failure rate that depends on crystal strain and temperature, the initiation of chain slippage at these sites can be thought of in the same way as the rupture of a covalent bond in the perfect crystal.

To explore this further, a system of isolated chain-end defects is constructed following Pattern E in Figure 5.20, which consists of a 3×8×64 arrangement of crystalline PPTA unit cells. In Pattern E, defects are uniformly spaced 16 monomers apart along the z-axis of the crystallite, and placed closer than this only when at least three chains separate the defects within a hydrogen bonded sheet. This ensures that each defect lies well outside of the zone of influence of all other defects in the crystal (about ±8 monomers along the broken chain axis relative to the defect, and ±4 monomers along the axes of adjacent chains, as discussed in Section 4.2.1). The PCFF force field is then used to simulate the strain rate loading of this system at various strain rate and temperature combinations. PCFF is used here to ensure that only hydrogen bonds, and not primary covalent bonds, break in these simulations – based on the studies performed in Section 5.3.1, this crystal would fail by primary bond rupture in ReaxFF. While these simulations do not necessarily represent the behavior of a true PPTA crystal, they are still relevant for characterizing the failure behavior of hydrogen bonds near chain-end defects. Chain slippage by hydrogen bond failure is defined to initiate when a hydrogen bond at the site exceeds an O–H distance of 5.5 Å. In strain-to-failure simulations of similar systems using PCFF, this distance criterion was visually estimated to be a good indicator that inter-chain slippage had initiated near a defect site.

Figure 5.21 presents the results of these strain-to-first-failure simulations in terms of the strain observed at first hydrogen bond failure versus strain rate, where first hydrogen bond failure via exceedance of 5.5 Å is indicative of the initiation of chain slippage at the defect site. Note the similarity of these results when compared to the same plot generated for primary bond failure in Figure 5.8: in both cases, the strain at first failure decreases with decreasing strain rate and increasing temperature, and has an approximately linear dependence on log

Figure 5.20: *Pattern E*

strain rate. As with primary bonds in Section 5.2.3, a reliability modeling approach is taken where each chain-end defect site is treated as an independently-operating component with a time-dependent failure rate function $\lambda_0(\epsilon(t), T(t))$. The model assumes a functional form of the bond failure rate function $\lambda_0(\epsilon, T)$ according to equation (5.26), and the model is parameterized by fitting the failure data from Figure 5.21 to the objective function defined in equation (5.31). The results of the fits are displayed in Figures 5.22–5.24, which isolate the failure behavior for temperatures of 300 K, 400 K, and 500 K. In each figure, the error bars associated with the fit are the standard deviation of the predicted mean strain at first failure as computed from reliability theory using the square root of the variance from equation (5.10). From these figures, it is apparent that the model is capable of representing the failure behavior of hydrogen bonds at these chain-end defect sites.

The best-fit parameters of the model to the data yield kinetic theory of fracture parameters $U_0 = 90.6$ kJ/mol, $\gamma = 414$ Å^3, and $\omega_0 = 2.2 \times 10^{11}$ Hz. Unlike the parameters extracted from examining primary bond failure data in Section 5.2.3, these parameters are not all in the expected range of values for hydrogen bonds. For example, the activation energy for hydrogen bonds has been experimentally observed to be in the range of 1–6 kcal/mol (about 4–25 kJ/mol) [65], which is significantly lower than the value of 90.6 kJ/mol obtained here. It is also expected that the activation energy for a hydrogen bond would be substantially lower than for a primary bond, which would be consistent with the activation energies cited in [65], yet it is just under 80% of the activation energy obtained for a primary bond (114 kJ/mol) in Section 5.2.3. Also, bond frequencies in the MD simulations conducted here are all on the order of 10^{13} Hz, so the value of ω_0 obtained here is lower than expected. However, care must be taken in interpreting the physical meaning of these parameters for the simulations conducted here. The actual failure event in these simulations is the initiation of chain slippage near chain-end defect sites. The initiation of chain slippage requires the rupture of more than a single hydrogen bond, and as such, the activation energy parameter obtained here should actually be interpreted as the energy required to initiate chain-slippage, which requires multiple hydrogen bonds near the defect site to rupture. Similarly, the frequency parameter ω_0 does not represent the frequency of a single hydrogen bond, but rather some collective frequency measure of the group of bonds which fail, which may account for the lower-than-expected value obtained here. Considering these observations, the kinetic theory of fracture parameters obtained here for hydrogen bond rupture are reasonable, and as with

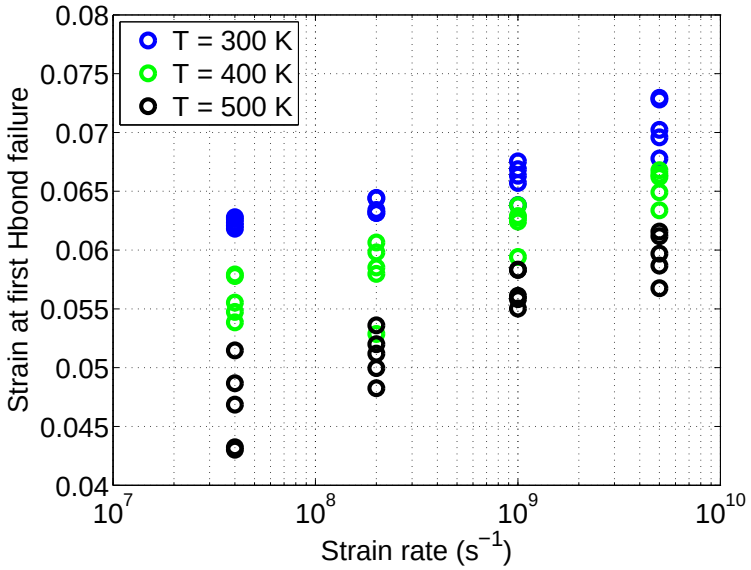

Figure 5.21: *Strain at first hydrogen bond failure at several strain rates and temperatures for Pattern E simulated using PCFF.*

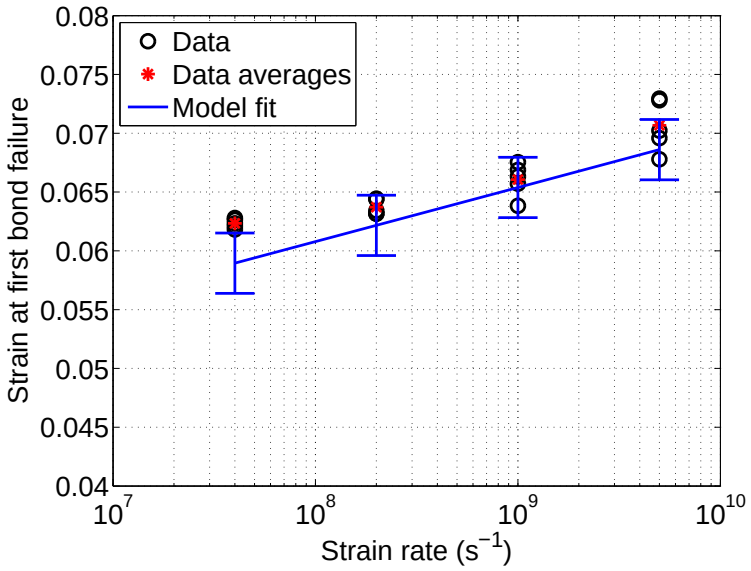

Figure 5.22: *Model fit to first hydrogen bond failure data at 300 K.*

the case of primary bonds, it can be concluded that the failure of hydrogen bonds near chain-end defects can be modeled via reliability theory, and that the assumption that failure rate can be determined by the proposed kinetic theory of fracture relation (5.17) is a good approximation to the actual bond behavior.

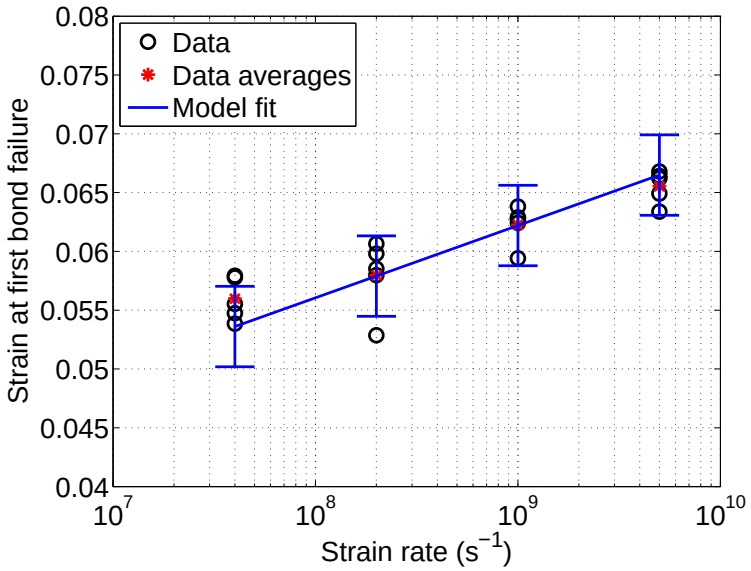

Figure 5.23: *Model fit to first hydrogen bond failure data at 400 K.*

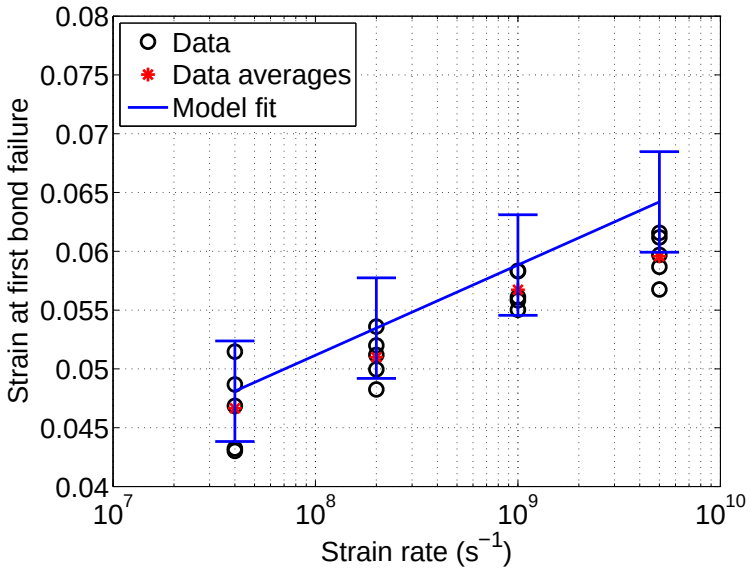

Figure 5.24: *Model fit to first hydrogen bond failure data at 500 K.*

Chapter 6

Conclusion

This work uses molecular dynamics simulations to explore in detail the mechanical response of crystalline PPTA to axial dynamic strain rate loading. While the mechanical properties of perfectly crystalline PPTA near equilibrium conditions have previously been studied using molecular dynamics, this work makes a novel contribution by studying the strain-to-failure response of crystalline PPTA under dynamic strain rate loading while using a reactive bond order force field (ReaxFF) to accommodate covalent bond rupture in the material response. These simulations show that crystallite failure strain increases with increasing strain rate, while both failure strain and modulus decrease with increasing temperature. These simulations also predict the Type 2 bond (see Figure 3.2) along the chain backbone to be the weakest link in the polymer chain, according to the ReaxFF force field parameterization used here. Finally, the influence of chain-end defects is studied, including their influence on molecular chain micromechanical behavior, crystallite failure mechanisms, and crystallite modulus.

A second contribution is made by studying the nature of primary and secondary bond failure in PPTA crystallites. The mechanisms involved in primary and secondary bond failure are studied in detail, and shown to strongly depend on the distribution of defects in the crystal. When defects are clustered in a narrow band, hydrogen bond failure and inter-chain slippage is the observed failure mechanism, whereas when defects are spread further apart, failure is initiated by primary covalent bond rupture along the polymer chain backbones. In addition to characterizing the nature of bond failure as influenced by the chain-end defect distribution, these simulations have demonstrated that PPTA crystallites retain a significant amount of their strength even in the presence of very narrow defect cluster bands (on the order of nanometers), which explains why true PPTA fibers are so strong despite the the underlying microstructure consisting of crystallites with chain-end defect planes spaced periodically along the fiber axis. Motivated by the stochastic nature of bond failure in PPTA crystals, a model for bond failure is proposed which leverages reliability theory to predict the onset of primary bond ruptures in a perfect crystal and secondary bond ruptures in a crystal containing non-interacting chain-end defects. It is shown that bonds can be reasonably represented as having a failure rate that depends on the strain and temperature within the

crystal, and that the failure rate can be accurately represented through the relationship postulated by the kinetic theory of fracture in equation (5.17). This model allows for the prediction of onset of bond failure at at slow strain rates and large crystals which cannot be practically simulated by standard MD methods.

Collectively, the work performed here provides detailed analysis of the behavior of the individual crystallites which make up a single PPTA fiber, with respect to performance under strain rate loading and the failure mechanisms involved in crystallite failure. The work in Chapter 4 lays a foundation for understanding the mechanical behavior of highly crystalline PPTA. It should be emphasized that true PPTA crystallites contain a more extensive array of defects than considered here, including imperfect chain alignment within the crystallite and deviation from a strictly linear chain configuration, impurities, and sheet-stacking faults. Relating the crystallite properties to properties of single PPTA fibers would require modeling these types of faults within the crystallite, combined with further levels of defects in the PPTA microstructural hierarchy such as the the pleated-sheet structure discussed in Chapter 2. It is likely the combined effect of all of these defects within the polymer fiber that leads to the discrepancy between fiber modulus of true PPTA fibers (order 100 GPa) and the crystallite modulus and failure strain observed in the simulations performed here (290–320 GPa). Future work on PPTA fiber modeling at the molecular scale might explore the incorporation of these types of defects into a PPTA crystallite model and/or a coarse grained model of interacting crystallites within a single fiber.

Another avenue of future work involves the modeling of fiber failure through bond rupture under strain rate loading. Chapter 5 showed that both primary and secondary bonds can be reasonably represented by concepts from reliability theory, where bonds under dynamic strain rate loading have time-dependent failure rates. Such stochastic processes may be amenable to modeling via Monte Carlo methods, where bond rupture is treated as a probabilistic event which depends on the loading rate and temperature of the crystal. The challenge with such an approach lies in accurately characterizing the failure rates of individual bonds in the crystal as a function of both their proximity to pre-existing chain-end defects and their response to the dynamic event of a nearby covalent bond rupture. If such a model could be accurately parameterized, it would allow for the simulation of failure of crystallites of the size observed in true PPTA fibers (around 200 nm long and 60–600 nm in diameter) at experimentally relevant strain rates. This would be a good foundation for addressing the failure behavior of a single PPTA fiber, whose microstructure consists of a number of such crystallites.

Bibliography

[1] Accelrys Software Inc. *Materials Studio*. San Diego, 2011.

[2] D. Ahmed, Z. Hongpeng, K. Haijuan, L. Jing, M. Yu, and Y. Muhuo. "Microstructural Developments of Poly (p-phenylene terephthalamide) Fibers During Heat Treatment Process: A Review". *Materials Researh* 17.5 (2014), pp. 1180–1200.

[3] H. M. Aktulga, S. A. Pandit, A. C. T. van Duin, and A. Y. Grama. "Reactive Molecular Dynamics: Numerical Methods and Algorithmic Techniques". *SIAM Journal on Scientific Computing* 34.1 (2012), pp. C1–C23.

[4] M. Allen and D. Tildesley. *Computer Simulation of Liquids*. New York: Oxford University Press, 1987.

[5] R. Barton. "Paracrystallinity-modulus relationships in Kevlar aramid fibers". *Journal of Macromolecular Science, Part B* B24 (1985), pp. 119–130.

[6] C. Buckley. "The Ultimate Strength and Stiffness of Polymers". *Annu. Rev. Mater. Sci.* 25 (1995), pp. 295–323.

[7] M. J. Buehler, A. C. T. van Duin, and W. A. Goddard. "Multiparadigm Modeling of Dynamical Crack Propagation in Silicon Using a Reactive Force Field". *Physical Review Letters* 96.9 (2006), p. 095505.

[8] A. Chandra. "Dynamical Behavior of Anion–Water and Water–Water Hydrogen Bonds in Aqueous Electrolyte Solutions: A Molecular Dynamics Study". *Journal of Physical Chemistry B* 107 (2003), pp. 3899–3906.

[9] M. Cheng, W. Chen, and T. Weerasooriya. "Mechanical Properties of Kevlar KM2 Single Fiber". *Journal of Engineering Materials and Technology* 127 (2005), pp. 197–203.

[10] K. Chenoweth, A. C. T. van Duin, and W. A. Goddard III. "ReaxFF reactive force field for molecular dynamics simulations of hydrocarbon oxidation." *The Journal of Physical Chemistry A* 112.5 (2008), pp. 1040–1053.

[11] S. W. Cranford, D. B. Brommer, and M. J. Buehler. "Extended graphynes: simple scaling laws for stiffness, strength and fracture". *Nanoscale* 4 (2012), pp. 7797–7809.

[12] S. W. Cranford and M. J. Buehler. "Mechanical properties of graphyne". *Carbon* 49.13 (2011), pp. 4111–4121.

[13] M. Depner and B. L. Schfirmann. "Computer simulation of aromatic polyesters including molecular dynamics". *Polymer* 33.2 (1990), pp. 398–404.

[14] M. G. Dobb, D. J. Johnson, and B. P. Saville. "Direct observation of structure in high-modulus aromatic fibers". *Journal of Polymer Science: Polymer Symposia* 58 (1977), pp. 237–251.

[15] M. G. Dobb, D. J. Johnson, and B. P. Saville. "Supramolecular structure of a high-modulus polyaromatic fiber (Kevlar 49)". *Journal of Polymer Science: Polymer Physics Edition* 15 (1977), pp. 2201–2211.

[16] M. Dobb, D. Johnson, and B. Saville. "Structural aspects of high modulus polyamide fibres". *Philosophical Transactions of the Royal Society of London. Series A, Mathemetical and Physical Sciences* 294.1411 (2013), pp. 483–485.

[17] A. C. T. van Duin, S. Dasgupta, F. Lorant, and W. A. Goddard III. "ReaxFF: A Reactive Force Field for Hydrocarbons". *The Journal of Physical Chemistry A* 105.41 (2001), pp. 9396–9409.

[18] A. C. T. van Duin, A. Strachan, S. Stewman, Q. Zhang, X. Xu, and W. A. Goddard III. "ReaxFF SiO Reactive Force Field for Silicon and Silicon Oxide Systems". *Journal of Physical Chemistry A* 107 (2003), pp. 3803–3811.

[19] R. J. Gaymans, J. Tijssen, S. Harkema, and A. Bantjes. "Elastic modulus in the crystalline region of poly (p-phenylene terephthalamide)". *Polymer* 17 (1976), pp. 517–518.

[20] M. Grujicic, W. C. Bell, P. S. Glomski, B. Pandurangan, C. F. Yen, and B. A. Cheeseman. "Filament-level modeling of aramid-based high-performance structural materials". *Journal of Materials Engineering and Performance* 20 (2011), pp. 1401–1413.

[21] M. Grujicic, P. S. Glomski, B. Pandurangan, W. C. Bell, C.-F. Yen, and B. A. Cheeseman. "Multi-length scale computational derivation of Kevlar yarn-level material model". *Journal of Materials Science* 46.14 (2011), pp. 4787–4802.

[22] M. Grujicic, B. Pandurangan, J. S. Snipes, C.-F. Yen, and B. A. Cheeseman. "Multi-Length Scale-Enriched Continuum-Level Material Model for Kevlar-Fiber-Reinforced Polymer-Matrix Composites". *Journal of Materials Engineering and Performance* 22.3 (2013), pp. 681–695.

[23] M. Grujicic, S. Ramaswami, J. S. Snipes, R. Yavari, C. Yen, and B. A. Cheeseman. "Formation and Propagation , of Single p -Phenylene Terephthalamide (PPTA) Fibers". *Advances in Materials Science and Engineering* 2013 (2013), pp. 1–15.

[24] M. Grujicic, R. Yavari, S. Ramaswami, J. S. Snipes, C.-F. Yen, and B. A. Cheeseman. "Molecular-Level Study of the Effect of Prior Axial Compression/Torsion on the Axial-Tensile Strength of PPTA Fibers". *Journal of Materials Engineering and Performance* 22.11 (2013), pp. 3269–3287.

[25] M. Grujicic, R. Yavari, J. S. Snipes, S. Ramaswami, C.-F. Yen, and B. A. Cheeseman. "The effect of plain-weaving on the mechanical properties of warp and weft p-phenylene terephthalamide (PPTA) fibers/yarns". *Journal of Materials Science* 49.24 (2014), pp. 8272–8293.

[26] B. Gu. "Ballistic Penetration of Conically Cylindrical Steel Projectile into Plain-woven Fabric Target - A Finite Element Simulation". *Journal of Composite Materials* 38.22 (2004), pp. 2049–2074.

[27] B. Gu. "Analytical modeling for the ballistic perforation of planar plain-woven fabric target by projectile". *Composites Part B* 34.4 (2003), pp. 361–371.

[28] A. Hansen and J. Baker-Jarvis. "A rate dependent kinetic theory of fracture for polymers". *International Journal of Fracture* 44 (1990), pp. 221–231.

[29] R. Hockney and J. Eastwood. *Computer Simulation Using Particles*. New York, NY: Taylor & Francis Group, 1988.

[30] W. G. Hoover. "Canonical dynamics: Equilibrium phase-space distributions". *Physical Review A* 31.3 (1985), pp. 1695–1697.

[31] D. Hossain, M. Tschopp, D. Ward, J. Bouvard, P. Wang, and M. Horstemeyer. "Molecular dynamics simulations of deformation mechanisms of amorphous polyethylene". *Polymer* 51.25 (2010), pp. 6071–6083.

[32] A. Høyland and M. Rausand. *System Reliability Theory: Models, Statistical Methods, and Applications*. 2nd. Hoboken, New Jersey: John Wiley & Sons, Inc., 1994, pp. 15–63.

[33] C. C. Hsiao. "Fracture". *Physics Today* 19.3 (1966), pp. 49–53.

[34] T. Ii, K. Tashiro, M. Kobayashi, and H. Tadokoro. "X-ray study of lattice tensile properties of fully extended aromatic polyamide fibers over a wide temperature range". *Macromolecules* 20.2 (1987), pp. 347–351.

[35] B. D. Jensen, K. E. Wise, and G. M. Odegard. "The effect of time step, thermostat, and strain rate on ReaxFF simulations of mechanical failure in diamond, graphene, and carbon nanotube". *Journal of Computational Chemistry* 36.21 (2015), pp. 1587–1596.

[36] K. Kim, V. I. Artyukhov, W. Regan, Y. Liu, M. F. Crommie, B. I. Yakobson, and a. Zettl. "Ripping graphene: Preferred directions". *Nano Letters* 12.1 (2012), pp. 293–297.

[37] D. J. Lacks. "Molecular simulation of compressive failure in poly(p-phenylene teraphthalamide) crystals". *Journal of Materials Science* 31.22 (1996), pp. 5885–5889.

[38] D. J. Lacks and G. C. Rutledge. "Thermal Expansion and Temperature Dependence of Elastic Moduli of Aromatic Polyamides". *Macromolecules* 27 (1994), pp. 7197–7204.

[39] D. Languerand, H. Zhang, N. Murthy, K. Ramesh, and F. Sansoz. "Inelastic behavior and fracture of high modulus polymeric fiber bundles at high strain-rates". *Materials Science and Engineering A* 500 (2009), pp. 216–224.

[40] L. S. Li, L. F. Allard, and W. C. Bigelow. "On the morphology of aromatic polyamide fibers (Kevlar, Kevlar-49, and PRD-49)". *Journal of Macromolecular Science, Part B* 22.May 2014 (1983), pp. 269–290.

[41] J. Lim, J. Q. Zheng, K. Masters, and W. W. Chen. "Effects of gage length, loading rates, and damage on the strength of PPTA fibers". *International Journal of Impact Engineering* 38.4 (2011), pp. 219–227.

[42] L. Liu, Y. Liu, S. V. Zybin, H. Sun, and W. A. Goddard III. "ReaxFF-lg: Correction of the ReaxFF reactive force field for London dispersion, with applications to the equations of state for energetic materials". *The Journal of Physical Chemistry A* 115 (2011), pp. 11016–11022.

[43] A. Luzar and D. Chandler. "Structure and hydrogen bond dynamics of water–dimethyl sulfoxide mixtures by computer simulations". *The Journal of Chemical Physics* 98.10 (1993), pp. 8160–8173.

[44] G. J. Martyna, M. L. Klein, and M. E. Tuckerman. "Nose-Hoover chains: The canonical ensemble via continuous dynamics". *The Journal of Physical Chemistry* 97.4 (1992), pp. 2635–2643.

[45] G. J. Martyna, D. J. Tobias, and M. L. Klein. "Constant pressure molecular dynamics algorithms". *The Journal of Chemical Physics* 101.5 (1994), pp. 4177–4189.

[46] M. Mezei and D. L. Beveridge. "Theoretical studies of hydrogen bonding in liquid water and dilute aqueous solutions". *The Journal of Chemical Physics* 74.1 (1981), pp. 622–632.

[47] R. J. Morgan and C. O. Pruneda. "The characterization of the chemical impurities in Kevlar 49 fibres". *Polymer* 28.2 (1987), pp. 340–346.

[48] R. J. Morgan, C. Pruneda, and W. J. Steele. "The Relationship between the Physical Structure and the Microscopic Deformation and Failiure Processes of Polye(p-Phenylene Terephthalamide) Fibers". *Journal of Polymer Science: Polymer Physics Edition* 21 (1983), pp. 1757–1783.

[49] A. Nakano. "Parallel multilevel preconditioned conjugate-gradient approach to variable-charge molecular dynamics". *Computer Physics Communications* 104 (1997), pp. 59–69.

[50] K. D. Nielson, A. C. T. Van Duin, J. Oxgaard, W. Q. Deng, and W. A. Goddard. "Development of the ReaxFF reactive force field for describing transition metal catalyzed reactions, with application to the initial stages of the catalytic formation of carbon nanotubes". *Journal of Physical Chemistry A* 109 (2005), pp. 493–499.

[51] M. Northolt. "Tensile deformation of poly(p-phenylene terephthalamide) fibres, an experimental and theoretical analysis". *Polymer* 21.10 (1980), pp. 1199–1204.

[52] M. Northolt. "X-ray diffraction study of poly(p-phenylene terephthalamide) fibres". *European Polymer Journal* 10.9 (1974), pp. 799–804.

[53] M. Northolt and J. van Aartsen. "CHAIN ORIENTATION DISTRIBUTION AND". *Journal of Polymer Science: Polymer Symposium* 58 (1977), pp. 283–296.

[54] M. Northolt and R. v. d. Hout. "Elastic extension of an oriented crystalline fibre". *Polymer* 26 (1985), pp. 310–316.

[55] S. Nosé. "A unified formulation of the constant temperature molecular dynamics methods". *The Journal of Chemical Physics* 81 (1984), pp. 511–519.

[56] M. Panar, P. Avakian, R. C. Blume, K. H. Gardner, T. D. Gierke, and H. H. Yang. "Morphology of Poly (p-Phenylene Terephthalamide) Fibers". *Journal of Polymer Science: Polymer Physics Edition* 21 (1983), pp. 1955–1969.

[57] S. Plimpton. "Fast Parallel Algorithms for Short-Range Molecular Dynamics". *Journal of Computational Physics* 117 (1995), pp. 1–19.

[58] S. Plimpton, R. Pollock, and M. J. Stevens. "Particle Mesh Ewald and rRESPA for Parallel Molecular Dynamics Simulations". *Proceedings of the Eighth Siam Conference on Parallel Processing for Scientific Computing*. 1997, pp. 1–13.

[59] Y. Rao, A. J. Waddon, and R. J. Farris. "Structure-property relation in poly (p-phenylene terephthalamide) (PPTA) fibers". *Polymer* 42 (2001), pp. 5937–5946.

[60] A. K. Rappé and W. A. Goddard III. "Charge Equilibration for Molecular Dynamics Simulations". *The Journal of Physical Chemistry* 95.8 (1991), pp. 3358–3363.

[61] D. Roylance. "Some consequences of a fracture criterion for oriented polymers based on electron spin resonance spectoscopy". *International Journal of Fracture* 21 (1981), pp. 107–114.

[62] G. C. Rutledge and U. Suter. "Detailed Atomistic Simulation of Oriented Pseudocrystalline Polymers and Application to a Stiff-Chain Aramid". *Macromolecules* 24 (1991), pp. 1921–1933.

[63] G. C. Rutledge and U. W. Sutert. "Calculation of mechanical properties of poly(p-phenylene terephthalamide) by atomistic modelling". *Polymer* 32.12 (1991), pp. 2179–2189.

[64] D. Sen, K. S. Novoselov, P. M. Reis, and M. J. Buehler. "Tearing Graphene Sheets From Adhesive Substrates Produces Tapered Nanoribbons". *Small* 6.10 (2010), pp. 1108–1116.

[65] S.-Y. Sheu, D.-Y. Yang, H. L. Selzle, and E. W. Schlag. "Energetics of hydrogen bonds in peptides". *Proceedings of the National Academy of Sciences of the United States of America* 100.22 (2003), pp. 12683–12687.

[66] V. Shim, C. Lim, and K. Foo. "Dynamic mechanical properties of fabric armour". *International Journal of Impact Engineering* 25.1 (2001), pp. 1–15.

[67] Y. K. Shin, H. Kwak, C. Zou, A. V. Vasenkov, and A. C. T. V. Duin. "Development and Validation of a ReaxFF Reactive Force Field for Fe/Al/Ni Alloys: Molecular Dynamics Study of Elastic Constants, Diffusion, and Segregation". *The Journal of Physical Chemistry A* 116 (2012), pp. 12163–12174.

[68] W. Shinoda, M. Shiga, and M. Mikami. "Rapid estimation of elastic constants by molecular dynamics simulation under constant stress". *Physical Review B - Condensed Matter and Materials Physics* 69.13 (2004), pp. 16–18.

[69] A. Strachan, A. C. T. van Duin, D. Chakraborty, S. Dasgupta, and W. A. Goddard III. "Shock waves in high-energy materials: the initial chemical events in nitramine RDX." *Physical Review Letters* 91.9 (2003), p. 098301.

[70] H. Sun. "COMPASS: An ab Initio Force-Field Optimized for Condensed-Phase ApplicationssOverview with Details on Alkane and Benzene Compounds". *Journal of Physical Chemistry B* 5647.98 (1998), pp. 7338–7364.

[71] H. Sun, S. J. Mumby, J. R. Maple, and A. T. Hagler. "An ab Initio CFF93 All-Atom Force Field for Polycarbonates". *Journal of the American Chemical Society* 116 (1994), pp. 2978–2987.

[72] H. Tadokoro. "Structure and properties of crystalline polymers". *Polymer* 25 (1984), pp. 147–164.

[73] V. Tan, X. Zeng, and V. Shim. "Characterization and constitutive modeling of aramid fibers at high strain rates". *International Journal of Impact Engineering* 35.11 (2008), pp. 1303–1313.

[74] K. Tashiro, M. Kobayashi, and H. Tadokoro. "Elastic Moduli and Molecular Structures of Several Crystalline Polymers, Including Aromatic Polyamides". *Macromolecules* 10.2 (1977), pp. 413–420.

[75] A. Tobolsky and H. Eyring. "Mechanical Properties of Polymeric Materials". *The Journal of Chemical Physics* 11.3 (1943), p. 125.

[76] M. E. Tuckerman, J. Alejandre, R. López-Rendón, A. L. Jochim, and G. J. Martyna. "A Liouville-operator derived measure-preserving integrator for molecular dynamics simulations in the isothermal-isobaric ensemble". *Journal of Physics A: Mathematical and General* 39.19 (2006), pp. 5629–5651.

[77] Y. Wang and Y. Xia. "The effects of strain rate on the mechanical behaviour of kevlar fibre bundles: an experimental and theoretical study". *Composites Part A: Applied Science and Manufacturing* 29.11 (1998), pp. 1411–1415.

[78] X. Yang and S. L. Hsu. "Application of Molecular Simulation Technique To Calculate Structure and Define Deformation Mechanisms of High-Performance Polymers". *Macromolecules* 24 (1991), pp. 6680–6685.

[79] D. E. Yilmaz. "Modeling failure mechanisms of poly (p-phenylene terephthalamide) fiber using reactive potentials". *Computational Materials Science* 109 (2015), pp. 183–193.

[80] R. Young, D. Lu, R. Day, W. Knoff, and H. Davis. "Relationship between structure and mechanical properties for aramid fibres". *Journal of Materials Science* 27 (1992), pp. 5431–5440.

[81] D. Zhu, B. Mobasher, and S. D. Rajan. "Dynamic Tensile Testing of Kevlar 49 Fabrics". *Journal of Materials in Civil Engineering* 23.3 (2011), pp. 1–11.

[82] S. Zhurkov. "Kinetic concept of the strength of solids". *International Journal of Fracture* 1.4 (1965), pp. 311–323.

[83] S. Zhurkov and V. E. Korsukov. "Atomic mechanism of fracture of solid polymers." *Journal of Polymer Science: Polymer Physics Edition* 12 (1974), pp. 385–398.

Appendix A

Data files and force field parameters

A.1 PCFF-parameterized data file for a single unit cell of crystalline PPTA

This file contains the atomic coordinates and bond, angle, dihedral and improper topology of a single unit cell of crystalline PPTA. The coefficients in the data file are for the PCFF force field. An equivalent ReaxFF data file can be created by removing the molecular topology and force field coefficient information.

```
LAMMPS 2005 data file for kevlar_unt_pcff

     56 atoms
     60 bonds
     96 angles
    144 dihedrals
     32 impropers

   6 atom types
   7 bond types
  10 angle types
  15 dihedral types
   5 improper types

     0.000000000     7.870000000 xlo xhi
     0.000000000     5.180000000 ylo yhi
     0.000000000    12.900000000 zlo zhi

Masses

   1  15.999400
   2  14.010000
   3  12.011150
   4  12.011150
   5   1.008000
   6   1.007970

Pair Coeffs

   1   0.2670000000   3.3000000000
   2   0.1060000000   3.6000000000
```

```
   3   0.1200000000   3.8100000000
   4   0.0640000000   4.0100000000
   5   0.0130000000   1.6500000000
   6   0.0200000000   2.9950000000

Bond Coeffs

  1     1.2020   851.1403 -1918.4882  2160.7659
  2     1.3660   390.6783  -768.3798   923.2418
  3     1.4390   344.0452  -652.1208  1022.2242
  4     0.9959   495.8294 -1092.7239  1441.1290
  5     1.4890   339.3574  -655.7236   670.2362
  6     1.4170   470.8361  -627.6179  1327.6345
  7     1.0982   372.8251  -803.4526   894.3173

Angle Coeffs

  1   116.6260    42.4711   -10.4269     0.0000
  2   122.9480    40.4820   -16.2028     0.0000
  3   116.3230    18.3123    -7.8325     5.3290
  4   125.5320   101.8765   -41.8094     0.0000
  5   108.4400    84.8377   -19.9640     2.7405
  6   125.5320    72.3167   -16.0650     2.0818
  7   118.9000    61.0226   -34.9931     0.0000
  8   116.0640    71.2598   -15.8273     2.0506
  9   117.9400    35.1558   -12.4682     0.0000
 10   120.7640    73.2738   -27.4033    13.3920

Dihedral Coeffs

  1     0.0000          0          2          0          0          0
  2    -1.1077          0          2          0          0          0
  3     0.0000          0          2          0          0          0
  4    -1.1077          0          2          0          0          0
  5     0.0000          0          1          0          0          0
  6     0.0000          0          1          0          0          0
  7     0.0000          0          1          0          0          0
  8     0.0000          0          1          0          0          0
  9     8.3667          0          1          0          0          0
 10     0.0000          0          4          0          0          0
 11     0.0000          0          5          0          0          0
 12     0.0000          0          2          0          0          0
 13     0.0000          0          2          0          0          0
 14     0.0000          0          3          0          0          0
 15     0.0000          0          3          0          0          0

Improper Coeffs

  1     4.4181     0.0000
  2    49.3740     0.0000
  3    17.0526     0.0000
  4     4.8912     0.0000
  5    17.0526     0.0000

BondBond Coeffs

  1    41.4233     1.3660     1.4390
  2     8.6253     1.3660     0.9959
  3     8.2930     1.4390     0.9959
  4   116.9445     1.2020     1.3660
  5    69.9445     1.3660     1.4890
  6   116.9445     1.2020     1.4890
  7    68.2856     1.4170     1.4170
```

```
  8    37.8749     1.4890     1.4170
  9     1.0795     1.4170     1.0982
 10    37.8749     1.4390     1.4170

BondAngle Coeffs

  1     0.0000     0.0000     1.3660     1.4390
  2     0.0000     0.0000     1.3660     0.9959
  3    10.4568    12.8217     1.4390     0.9959
  4    46.1093    32.8758     1.2020     1.3660
  5    76.1093    72.8758     1.3660     1.4890
  6    76.1093    72.8758     1.2020     1.4890
  7    28.8708    28.8708     1.4170     1.4170
  8    23.6977    45.8865     1.4890     1.4170
  9    20.0033    24.2183     1.4170     1.0982
 10    53.6977    35.8865     1.4390     1.4170

AngleAngle Coeffs

  1     0.0000     0.0000     0.0000   116.6260   116.3230   122.9480
  2     0.0000     0.0000     0.0000   125.5320   108.4400   125.5320
  3     0.0000     5.9863     0.0000   116.0640   118.9000   116.0640
  4     0.0000     0.0000     0.0000   118.9000   117.9400   117.9400
  5     0.0000     0.0000     0.0000   120.7640   118.9000   120.7640

AngleAngleTorsion Coeffs

  1     0.0000   116.6260   125.5320
  2     0.0000   116.6260   108.4400
  3     0.0000   122.9480   125.5320
  4     0.0000   122.9480   108.4400
  5     0.0000   116.6260   120.7640
  6     0.0000   116.3230   120.7640
  7     0.0000   108.4400   116.0640
  8     0.0000   125.5320   116.0640
  9     0.0000   118.9000   118.9000
 10    -4.8141   118.9000   117.9400
 11     0.0000   116.0640   118.9000
 12     0.0000   116.0640   117.9400
 13     0.3598   117.9400   117.9400
 14     0.0000   120.7640   118.9000
 15     0.0000   120.7640   117.9400

EndBondTorsion Coeffs

1     0.0000     0.0000     0.0000     0.0000     0.0000     0.0000     1.4390     1.2020
2     0.0000     0.0000     0.0000     0.0000     0.0000     0.0000     1.4390     1.4890
3     0.0000     0.0000     0.0000     0.0000     0.0000     0.0000     0.9959     1.2020
4     0.0000     0.0000     0.0000     0.0000     0.0000     0.0000     0.9959     1.4890
5     0.0000     0.0000     0.0000     0.0000     0.0000     0.0000     1.3660     1.4170
6     0.0000     0.0000     0.0000     0.0000     0.0000     0.0000     0.9959     1.4170
7     0.0000     0.0000     0.0000     0.0000     0.0000     0.0000     1.3660     1.4170
8     0.0000     0.0000     0.0000     0.0000     0.0000     0.0000     1.2020     1.4170
9    -0.1185     6.3204     0.0000    -0.1185     6.3204     0.0000     1.4170     1.4170
10    0.0000    -6.8958     0.0000     0.0000    -0.4669     0.0000     1.4170     1.0982
11    0.0000     0.0000     0.0000     0.0000     0.0000     0.0000     1.4890     1.4170
12    0.0000     0.0000     0.0000     0.0000     0.0000     0.0000     1.4890     1.0982
13    0.0000    -0.6890     0.0000     0.0000    -0.6890     0.0000     1.0982     1.0982
14    0.0000     0.0000     0.0000     0.0000     0.0000     0.0000     1.4390     1.4170
15    0.0000     0.0000     0.0000     0.0000     0.0000     0.0000     1.4390     1.0982

MiddleBondTorsion Coeffs
```

```
  1     0.0000     0.0000     0.0000     1.3660
  2     0.0000     0.0000     0.0000     1.3660
  3     0.0000     0.0000     0.0000     1.3660
  4     0.0000     0.0000     0.0000     1.3660
  5     0.0000     0.0000     0.0000     1.4390
  6     0.0000     2.4730     0.0000     1.4390
  7     0.0000     2.4002     0.0000     1.4890
  8     0.0000     2.4002     0.0000     1.4890
  9    27.5989    -2.3120     0.0000     1.4170
 10     0.0000    -1.1521     0.0000     1.4170
 11     0.0000     3.8762     0.0000     1.4170
 12     0.0000     0.0000     0.0000     1.4170
 13     0.0000     4.8228     0.0000     1.4170
 14     0.0000     5.2012     0.0000     1.4170
 15     0.0000     5.2012     0.0000     1.4170

BondBond13 Coeffs

  1     0.0000     1.4390     1.2020
  2     0.0000     1.4390     1.4890
  3     0.0000     0.9959     1.2020
  4     0.0000     0.9959     1.4890
  5     0.0000     1.3660     1.4170
  6     0.0000     0.9959     1.4170
  7     0.0000     1.3660     1.4170
  8     0.0000     1.2020     1.4170
  9    53.0000     1.4170     1.4170
 10    -6.2741     1.4170     1.0982
 11     0.0000     1.4890     1.4170
 12     0.0000     1.4890     1.0982
 13    -1.7077     1.0982     1.0982
 14     0.0000     1.4390     1.4170
 15     0.0000     1.4390     1.0982

AngleTorsion Coeffs

  1     0.0000     0.0000     0.0000     0.0000     0.0000     0.0000   116.6260   125.5320
  2     0.0000     0.0000     0.0000     0.0000     0.0000     0.0000   116.6260   108.4400
  3     0.0000     0.0000     0.0000     0.0000     0.0000     0.0000   122.9480   125.5320
  4     0.0000     0.0000     0.0000     0.0000     0.0000     0.0000   122.9480   108.4400
  5     0.0000     0.0000     0.0000     0.0000     0.0000     0.0000   116.6260   120.7640
  6     0.0000     0.0000     0.0000     0.0000     0.0000     0.0000   116.3230   120.7640
  7     0.0000     0.0000     0.0000     0.0000     0.0000     0.0000   108.4400   116.0640
  8     0.0000     0.0000     0.0000     0.0000     0.0000     0.0000   125.5320   116.0640
  9     1.9767     1.0239     0.0000     1.9767     1.0239     0.0000   118.9000   118.9000
 10     0.0000     2.5014     0.0000     0.0000     2.7147     0.0000   118.9000   117.9400
 11     0.0000     0.0000     0.0000     0.0000     0.0000     0.0000   116.0640   118.9000
 12     0.0000     0.0000     0.0000     0.0000     0.0000     0.0000   116.0640   117.9400
 13     0.0000     2.4501     0.0000     0.0000     2.4501     0.0000   117.9400   117.9400
 14     0.0000     0.0000     0.0000     0.0000     0.0000     0.0000   120.7640   118.9000
 15     0.0000     0.0000     0.0000     0.0000     0.0000     0.0000   120.7640   117.9400

Atoms

      1      1   1 -0.531000    -0.165302868    -1.901093178     0.193460926
      2      1   1 -0.531000     0.165270001     1.901060104     6.901500225
      3      1   2 -0.726000     0.023610000     0.290080011     0.748199999
      4      1   3  0.660000    -0.062973137    -0.714852982    12.770974159
      5      1   2 -0.726000    -0.023610000    -0.290080242     6.346800327
      6      1   4 -0.018000    -0.031480003    -0.347060375    11.339098930
      7      1   4 -0.126800     0.668950021     0.777000010    10.926300049
      8      1   4 -0.126800     0.700430036     1.124059916     9.584699631
      9      1   4 -0.018000     0.031480003     0.347059995     8.655899048
```

```
     10      1   4 -0.126800    -0.668976421    -0.777026348     9.068600655
     11      1   4 -0.126800    -0.700455780    -1.124085598    10.410202026
     12      1   4  0.237000     0.015740002     0.145040005     2.167200089
     13      1   4 -0.126800     0.661080003    -0.927220039     2.760587692
     14      1   4 -0.126800     0.645340025    -1.072260075     4.140900135
     15      1   4  0.237000    -0.015740002    -0.145040207     4.927800179
     16      1   4 -0.126800    -0.661103363     0.927202523     4.334376812
     17      1   4 -0.126800    -0.645362968     1.072242856     2.954088688
     18      1   3  0.660000     0.062960006     0.714839995     7.223999977
     19      1   5  0.378000     0.102310002     1.201759934     0.348300010
     20      1   5  0.378000    -0.102331753    -1.201781445     6.746678352
     21      1   6  0.126800     1.164759994     1.346799970    11.609999657
     22      1   6  0.126800     1.211979985     1.947679877     9.288000107
     23      1   6  0.126800    -1.164778347    -1.346818142     8.384932518
     24      1   6  0.126800    -1.211997623    -1.947697811    10.706933975
     25      1   6  0.126800     1.141149998    -1.610980206     2.180091381
     26      1   6  0.126800     1.125410080    -1.859620266     4.566599846
     27      1   6  0.126800    -1.141166325     1.610967755     4.914884090
     28      1   6  0.126800    -1.125425930     1.859608173     2.528392076
     29      1   1 -0.531000     3.769697132     0.688906822    12.706539074
     30      1   1 -0.531000     4.100270001     4.491060104     5.998499775
     31      1   2 -0.726000     3.958610000     2.880080011    12.151800001
     32      1   3  0.660000     3.872026863     1.875147018     0.129025841
     33      1   2 -0.726000     3.911390000     2.299919758     6.553199673
     34      1   4 -0.018000     3.903519997     2.242939625     1.560901070
     35      1   4 -0.126800     4.603950021     3.367000010     1.973699951
     36      1   4 -0.126800     4.635430036     3.714059916     3.315300369
     37      1   4 -0.018000     3.966480003     2.937059995     4.244100952
     38      1   4 -0.126800     3.266023579     1.812973652     3.831399345
     39      1   4 -0.126800     3.234544220     1.465914402     2.489797974
     40      1   4  0.237000     3.950740002     2.735040005    10.732799911
     41      1   4 -0.126800     4.596080003     1.662779961    10.139412308
     42      1   4 -0.126800     4.580340025     1.517739925     8.759099865
     43      1   4  0.237000     3.919259998     2.444959793     7.972199821
     44      1   4 -0.126800     3.273896637     3.517202523     8.565623188
     45      1   4 -0.126800     3.289637032     3.662242856     9.945911312
     46      1   3  0.660000     3.997960006     3.304839995     5.676000023
     47      1   5  0.378000     4.037310002     3.791759934    12.551699990
     48      1   5  0.378000     3.832668247     1.388218555     6.153321648
     49      1   6  0.126800     5.099759994     3.936799970     1.290000343
     50      1   6  0.126800     5.146979985     4.537679877     3.611999893
     51      1   6  0.126800     2.770221653     1.243181858     4.515067482
     52      1   6  0.126800     2.723002377     0.642302189     2.193066025
     53      1   6  0.126800     5.076149998     0.979019794    10.719908619
     54      1   6  0.126800     5.060410080     0.730379734     8.333400154
     55      1   6  0.126800     2.793833675     4.200967755     7.985115910
     56      1   6  0.126800     2.809574070     4.449608173    10.371607924

Bonds

     1   1       1       4
     2   1       2      18
     3   2       3       4
     4   3       3      12
     5   4       3      19
     6   5       4       6
     7   3       5      15
     8   2       5      18
     9   4       5      20
    10   6       6       7
    11   6       6      11
    12   6       7       8
    13   7       7      21
```

```
    14   6       8       9
    15   7       8      22
    16   6       9      10
    17   5      18       9
    18   6      10      11
    19   7      10      23
    20   7      11      24
    21   6      12      13
    22   6      12      17
    23   6      13      14
    24   7      13      25
    25   6      14      15
    26   7      14      26
    27   6      15      16
    28   6      16      17
    29   7      16      27
    30   7      17      28
    31   1      29      32
    32   1      30      46
    33   2      31      32
    34   3      31      40
    35   4      31      47
    36   5      32      34
    37   3      33      43
    38   2      33      46
    39   4      33      48
    40   6      34      35
    41   6      34      39
    42   6      35      36
    43   7      35      49
    44   6      36      37
    45   7      36      50
    46   6      37      38
    47   5      46      37
    48   6      38      39
    49   7      38      51
    50   7      39      52
    51   6      40      41
    52   6      40      45
    53   6      41      42
    54   7      41      53
    55   6      42      43
    56   7      42      54
    57   6      43      44
    58   6      44      45
    59   7      44      55
    60   7      45      56

Angles

     1   1       4       3      12
     2   2       4       3      19
     3   3      12       3      19
     4   4       1       4       3
     5   5       3       4       6
     6   6       1       4       6
     7   1      18       5      15
     8   3      15       5      20
     9   2      18       5      20
    10   7       7       6      11
    11   8       4       6       7
    12   8       4       6      11
    13   7       6       7       8
```

```
14   9      6      7     21
15   9      8      7     21
16   7      7      8      9
17   9      7      8     22
18   9      9      8     22
19   7      8      9     10
20   8     18      9      8
21   8     18      9     10
22   7      9     10     11
23   9      9     10     23
24   9     11     10     23
25   7     10     11      6
26   9     10     11     24
27   9      6     11     24
28  10      3     12     13
29  10      3     12     17
30   7     13     12     17
31   7     12     13     14
32   9     12     13     25
33   9     14     13     25
34   7     13     14     15
35   9     13     14     26
36   9     15     14     26
37  10      5     15     14
38   7     14     15     16
39  10      5     15     16
40   7     15     16     17
41   9     15     16     27
42   9     17     16     27
43   7     16     17     12
44   9     16     17     28
45   9     12     17     28
46   5      5     18      9
47   6      2     18      9
48   4      2     18      5
49   1     32     31     40
50   2     32     31     47
51   3     40     31     47
52   4     29     32     31
53   5     31     32     34
54   6     29     32     34
55   1     46     33     43
56   3     43     33     48
57   2     46     33     48
58   7     35     34     39
59   8     32     34     35
60   8     32     34     39
61   7     34     35     36
62   9     34     35     49
63   9     36     35     49
64   7     35     36     37
65   9     35     36     50
66   9     37     36     50
67   7     36     37     38
68   8     46     37     36
69   8     46     37     38
70   7     37     38     39
71   9     37     38     51
72   9     39     38     51
73   7     38     39     34
74   9     38     39     52
75   9     34     39     52
76  10     31     40     41
```

```
    77  10     31     40     45
    78   7     41     40     45
    79   7     40     41     42
    80   9     40     41     53
    81   9     42     41     53
    82   7     41     42     43
    83   9     41     42     54
    84   9     43     42     54
    85  10     33     43     42
    86   7     42     43     44
    87  10     33     43     44
    88   7     43     44     45
    89   9     43     44     55
    90   9     45     44     55
    91   7     44     45     40
    92   9     44     45     56
    93   9     40     45     56
    94   5     33     46     37
    95   6     30     46     37
    96   4     30     46     33

Dihedrals

     1   1     12      3      4      1
     2   2     12      3      4      6
     3   3     19      3      4      1
     4   4     19      3      4      6
     5   5      4      3     12     13
     6   5      4      3     12     17
     7   6     19      3     12     13
     8   6     19      3     12     17
     9   7      3      4      6      7
    10   7      3      4      6     11
    11   8      1      4      6      7
    12   8      1      4      6     11
    13   5     18      5     15     14
    14   5     18      5     15     16
    15   6     20      5     15     14
    16   6     20      5     15     16
    17   2     15      5     18      9
    18   1     15      5     18      2
    19   4     20      5     18      9
    20   3     20      5     18      2
    21   9     11      6      7      8
    22  10     11      6      7     21
    23  11      4      6      7      8
    24  12      4      6      7     21
    25   9      7      6     11     10
    26  10      7      6     11     24
    27  11      4      6     11     10
    28  12      4      6     11     24
    29   9      6      7      8      9
    30  10      6      7      8     22
    31  10      9      8      7     21
    32  13     21      7      8     22
    33   9      7      8      9     10
    34  11     18      9      8      7
    35  10     10      9      8     22
    36  12     18      9      8     22
    37   9      8      9     10     11
    38  10      8      9     10     23
    39  11     18      9     10     11
    40  12     18      9     10     23
```

```
 41   7      5     18      9      8
 42   8      2     18      9      8
 43   7      5     18      9     10
 44   8      2     18      9     10
 45   9      9     10     11      6
 46  10      9     10     11     24
 47  10      6     11     10     23
 48  13     23     10     11     24
 49  14      3     12     13     14
 50  15      3     12     13     25
 51   9     17     12     13     14
 52  10     17     12     13     25
 53  14      3     12     17     16
 54  15      3     12     17     28
 55   9     13     12     17     16
 56  10     13     12     17     28
 57   9     12     13     14     15
 58  10     12     13     14     26
 59  10     15     14     13     25
 60  13     25     13     14     26
 61  14      5     15     14     13
 62   9     13     14     15     16
 63  15      5     15     14     26
 64  10     16     15     14     26
 65   9     14     15     16     17
 66  10     14     15     16     27
 67  14      5     15     16     17
 68  15      5     15     16     27
 69   9     15     16     17     12
 70  10     15     16     17     28
 71  10     12     17     16     27
 72  13     27     16     17     28
 73   1     40     31     32     29
 74   2     40     31     32     34
 75   3     47     31     32     29
 76   4     47     31     32     34
 77   5     32     31     40     41
 78   5     32     31     40     45
 79   6     47     31     40     41
 80   6     47     31     40     45
 81   7     31     32     34     35
 82   7     31     32     34     39
 83   8     29     32     34     35
 84   8     29     32     34     39
 85   5     46     33     43     42
 86   5     46     33     43     44
 87   6     48     33     43     42
 88   6     48     33     43     44
 89   2     43     33     46     37
 90   1     43     33     46     30
 91   4     48     33     46     37
 92   3     48     33     46     30
 93   9     39     34     35     36
 94  10     39     34     35     49
 95  11     32     34     35     36
 96  12     32     34     35     49
 97   9     35     34     39     38
 98  10     35     34     39     52
 99  11     32     34     39     38
100  12     32     34     39     52
101   9     34     35     36     37
102  10     34     35     36     50
103  10     37     36     35     49
```

```
   104  13     49     35     36     50
   105   9     35     36     37     38
   106  11     46     37     36     35
   107  10     38     37     36     50
   108  12     46     37     36     50
   109   9     36     37     38     39
   110  10     36     37     38     51
   111  11     46     37     38     39
   112  12     46     37     38     51
   113   7     33     46     37     36
   114   8     30     46     37     36
   115   7     33     46     37     38
   116   8     30     46     37     38
   117   9     37     38     39     34
   118  10     37     38     39     52
   119  10     34     39     38     51
   120  13     51     38     39     52
   121  14     31     40     41     42
   122  15     31     40     41     53
   123   9     45     40     41     42
   124  10     45     40     41     53
   125  14     31     40     45     44
   126  15     31     40     45     56
   127   9     41     40     45     44
   128  10     41     40     45     56
   129   9     40     41     42     43
   130  10     40     41     42     54
   131  10     43     42     41     53
   132  13     53     41     42     54
   133  14     33     43     42     41
   134   9     41     42     43     44
   135  15     33     43     42     54
   136  10     44     43     42     54
   137   9     42     43     44     45
   138  10     42     43     44     55
   139  14     33     43     44     45
   140  15     33     43     44     55
   141   9     43     44     45     40
   142  10     43     44     45     56
   143  10     40     45     44     55
   144  13     55     44     45     56

Impropers

     1   1      4      3     12     19
     2   2      1      4      3      6
     3   1     18      5     15     20
     4   3      4      6     11      7
     5   4      6      7      8     21
     6   4      7      8      9     22
     7   3     18      9     10      8
     8   4      9     10     11     23
     9   4     10     11      6     24
    10   5      3     12     13     17
    11   4     12     13     14     25
    12   4     13     14     15     26
    13   5      5     15     14     16
    14   4     15     16     17     27
    15   4     16     17     12     28
    16   2      2     18      5      9
    17   1     32     31     40     47
    18   2     29     32     31     34
    19   1     46     33     43     48
```

```
   20   3     32     34     39     35
   21   4     34     35     36     49
   22   4     35     36     37     50
   23   3     46     37     38     36
   24   4     37     38     39     51
   25   4     38     39     34     52
   26   5     31     40     41     45
   27   4     40     41     42     53
   28   4     41     42     43     54
   29   5     33     43     42     44
   30   4     43     44     45     55
   31   4     44     45     40     56
   32   2     30     46     33     37
```

A.2 ReaxFF parameter file

The following is the ReaxFF parameter file for the ReaxFF simulations used in this thesis. The file is also available as part of the supplemental information in [42].

```
Reactive MD-force field: nitramines (RDX/HMX/TATB/PETN))+innervdWaa+lg
 39       ! Number of general parameters
   50.0000 !Overcoordination parameter
    9.4514 !Overcoordination parameter
   29.8953 !Valency angle conjugation parameter
  216.5421 !Triple bond stabilisation parameter
   12.2245 !Triple bond stabilisation parameter
    0.0000 !C2-correction
    1.0701 !Undercoordination parameter
    7.5000 !Triple bond stabilisation parameter
   11.9083 !Undercoordination parameter
   13.3822 !Undercoordination parameter
  -10.9834 !Triple bond stabilization energy
    0.0000 !Lower Taper-radius
   10.0000 !Upper Taper-radius
    2.8793 !Not used
   33.8667 !Valency undercoordination
    3.3976 !Valency angle/lone pair parameter
    1.0563 !Valency angle
    2.0384 !Valency angle parameter
    6.1431 !Not used
    6.9290 !Double bond/angle parameter
    0.0283 !Double bond/angle parameter: overcoord
    0.0570 !Double bond/angle parameter: overcoord
   -2.4837 !Not used
    5.8374 !Torsion/BO parameter
   10.0000 !Torsion overcoordination
    1.8820 !Torsion overcoordination
   -1.2327 !Conjugation 0 (not used)
    2.1861 !Conjugation
    1.5591 !vdWaals shielding
    0.0100 !Cutoff for bond order (*100)
    4.8414 !Valency angle conjugation parameter
    3.5857 !Overcoordination parameter
   38.6472 !Overcoordination parameter
    2.1533 !Valency/lone pair parameter
    0.5000 !Not used
    1.0000 !Scale factor (d) in dispersion
    5.0000 !Molecular energy (not used)
    0.0000 !Molecular energy (not used)
```

```
   6.9784 !Valency angle conjugation parameter
 7    ! Nr of atoms; cov.r; valency;a.m;Rvdw;Evdw;gammaEEM;cov.r2;#
          alfa;gammavdW;valency;Eunder;Eover;chiEEM;etaEEM;n.u.
          cov r3;Elp;Heat inc.;n.u.;n.u.;n.u.;n.u.
          ov/un;val1;n.u.;val3,vval4
C    1.3742   4.0000  12.0000   1.9684   0.1723   0.8712   1.2385   4.0000
     8.7696 100.0000   4.0000  31.0823  79.5548   5.7254   6.9235   0.0000
     1.2104   0.0000 183.8108   5.7419  33.3951  11.9957   0.8563   0.0000
    -2.8983   4.7820   1.0564   4.0000   2.9663   1.6737   0.1421  14.0707
     0.0001   1.9255
H    0.6867   1.0000   1.0080   1.3525   0.0616   0.8910  -0.1000   1.0000
     9.1506 100.0000   1.0000   0.0000 121.1250   3.8446  10.0839   1.0000
    -0.1000   0.0000  58.4369   3.8461   3.2540   1.0000   1.0698   0.0000
   -15.7683   2.1504   1.0338   1.0000   2.8793   1.2669   0.0139  12.4538
     0.0001   1.4430
O    1.3142   2.0000  15.9990   1.9741   0.0880   0.8712   1.1139   6.0000
     9.9926 100.0000   4.0000  29.5271 116.0768   8.5000   7.1412   2.0000
     0.9909  14.7235  69.2921   9.1371   1.6258   0.1863   0.9745   0.0000
    -3.5965   2.5000   1.0493   4.0000   2.9225   1.7221   0.1670  13.9991
   624.0000   1.7500
N    1.2456   3.0000  14.0000   2.0437   0.1035   0.8712   1.1911   5.0000
     9.8823 100.0000   4.0000  32.4758 100.0000   6.8453   6.8349   2.0000
     1.0636   0.0276 127.9672   2.2169   2.8632   2.4419   0.9745   0.0000
    -4.0959   2.0047   1.0183   4.0000   2.8793   1.5967   0.1649  13.9888
   1239.000   1.8300
S    1.9647   2.0000  32.0600   2.0783   0.2176   1.0336   1.5386   6.0000
     9.9676   5.0812   4.0000  35.1648 112.1416   6.5000   8.2545   2.0000
     1.4703   9.4922  70.0338   8.5146  28.0801   8.5010   0.9745   0.0000
   -10.0773   2.7466   1.0338   6.2998   2.8793   1.8000   0.0000  14.0000
   180.0000   2.0783
Si   2.0276   4.0000  28.0600   2.2042   0.1322   0.8218   1.5758   4.0000
    11.9413   2.0618   4.0000  11.8211 136.4845   1.8038   7.3852   0.0000
    -1.0000   0.0000 126.5331   6.4918   8.5961   0.2368   0.8563   0.0000
    -3.8112   3.1873   1.0338   4.0000   2.5791   0.0000   0.0000   0.0000
   180.0000   2.2042
X   -0.1000   2.0000   1.0080   2.0000   0.0000   1.0000  -0.1000   6.0000
    10.0000   2.5000   4.0000   0.0000   0.0000   8.5000   1.5000   0.0000
    -0.1000   0.0000  -2.3700   8.7410  13.3640   0.6690   0.9745   0.0000
   -11.0000   2.7466   1.0338   4.0000   2.8793   0.0000   0.0000   0.0000
   180.0000   2.0000
18      ! Nr of bonds; Edis1;LPpen;n.u.;pbe1;pbo5;13corr;pbo6
                       pbe2;pbo3;pbo4;Etrip;pbo1;pbo2;ovcorr
 1  1 141.9346 113.4487  67.6027   0.1554  -0.3045   1.0000  30.4515   0.4283
       0.0801  -0.2113   8.5395   1.0000  -0.0933   6.6967   1.0000   0.0000
 1  2 163.6889   0.0000   0.0000  -0.4525   0.0000   1.0000   6.0000   0.5921
      12.1053   1.0000   0.0000   1.0000  -0.0097   8.6351   0.0000   0.0000
 2  2 169.8421   0.0000   0.0000  -0.3591   0.0000   1.0000   6.0000   0.7503
       9.3119   1.0000   0.0000   1.0000  -0.0169   5.9406   0.0000   0.0000
 1  3 159.7219 116.8921  77.9315  -0.4324  -0.1742   1.0000  15.0019   0.5160
       1.2934  -0.3079   7.0252   1.0000  -0.1543   4.5116   0.0000   0.0000
 3  3 108.9631 158.3501  42.0558   0.1226  -0.1324   1.0000  28.5716   0.2545
       1.0000  -0.2656   8.6489   1.0000  -0.1000   6.8482   1.0000   0.0000
 1  4 128.9104 171.2945 100.5836  -0.1306  -0.4948   1.0000  26.7458   0.4489
       0.3746  -0.3549   7.0000   1.0000  -0.1248   4.9232   1.0000   0.0000
 3  4  85.0402 118.8680  75.7263   0.7080  -0.1062   1.0000  16.6913   0.2407
       0.3535  -0.1906   8.4054   1.0000  -0.1154   5.6575   1.0000   0.0000
 4  4 160.6599  73.3721 154.2849  -0.7107  -0.1462   1.0000  12.0000   0.6826
       0.9330  -0.1434  10.6712   1.0000  -0.0890   4.6486   1.0000   0.0000
 2  3 219.7016   0.0000   0.0000  -0.6643   0.0000   1.0000   6.0000   0.9854
       5.1146   1.0000   0.0000   1.0000  -0.0532   5.1189   0.0000   0.0000
 2  4 208.0443   0.0000   0.0000  -0.3923   0.0000   1.0000   6.0000   0.3221
      10.5505   1.0000   0.0000   1.0000  -0.0690   6.2949   0.0000   0.0000
 1  5 128.7959  56.4134  39.0716   0.0688  -0.4463   1.0000  31.1766   0.4530
```

```
        0.1955  -0.3587   6.2148   1.0000  -0.0770   6.6386   1.0000   0.0000
 2  5 128.6090   0.0000   0.0000  -0.5555   0.0000   1.0000   6.0000   0.4721
       10.8735   1.0000   0.0000   1.0000  -0.0242   9.1937   1.0000   0.0000
 3  5   0.0000   0.0000   0.0000   0.5563  -0.4038   1.0000  49.5611   0.6000
        0.4259  -0.4577  12.7569   1.0000  -0.1100   7.1145   1.0000   0.0000
 4  5   0.0000   0.0000   0.0000   0.4438  -0.2034   1.0000  40.3399   0.6000
        0.3296  -0.3153   9.1227   1.0000  -0.1805   5.6864   1.0000   0.0000
 5  5  96.1871  93.7006  68.6860   0.0955  -0.4781   1.0000  17.8574   0.6000
        0.2723  -0.2373   9.7875   1.0000  -0.0950   6.4757   1.0000   0.0000
 6  6 109.1904  70.8314  30.0000   0.2765  -0.3000   1.0000  16.0000   0.1583
        0.2804  -0.1994   8.1117   1.0000  -0.0675   8.2993   0.0000   0.0000
 2  6 137.1002   0.0000   0.0000  -0.1902   0.0000   1.0000   6.0000   0.4256
       17.7186   1.0000   0.0000   1.0000  -0.0377   6.4281   0.0000   0.0000
 3  6 191.1743  52.0733  43.3991  -0.2584  -0.3000   1.0000  36.0000   0.8764
        1.0248  -0.3658   4.2151   1.0000  -0.5004   4.2605   1.0000   0.0000
10    ! Nr of off-diagonal terms; Ediss;Ro;gamma;rsigma;rpi;rpi2
 1  2   0.0464   1.8296   9.9214   1.0029  -1.0000  -1.0000   0.0000
 2  3   0.0403   1.6913  10.4801   0.8774  -1.0000  -1.0000   0.0000
 2  4   0.0524   1.7325  10.1306   0.9982  -1.0000  -1.0000 295.0000
 1  3   0.1028   1.9277   9.1521   1.3399   1.1104   1.1609 632.0000
 1  4   0.2070   1.7366   9.5916   1.2960   1.2008   1.1262 650.0000
 3  4   0.0491   1.7025  10.6101   1.3036   1.1276   1.0173 880.0000
 2  6   0.0470   1.6738  11.6877   1.1931  -1.0000  -1.0000   0.0000
 3  6   0.1263   1.8163  10.6833   1.6266   1.2052  -1.0000   0.0000
 1  5   0.1408   1.8161   9.9393   1.7986   1.3021   1.4031   0.0000
 2  5   0.0895   1.6239  10.0104   1.4640  -1.0000  -1.0000   0.0000
62    ! Nr of angles;at1;at2;at3;Thetao,o;ka;kb;pv1;pv2
 1  1  1  74.0317  32.2712   0.9501   0.0000   0.1780  10.5736   1.0400
 1  1  2  70.6558  14.3658   5.3224   0.0000   0.0058   0.0000   1.0400
 2  1  2  76.7339  14.4217   3.3631   0.0000   0.0127   0.0000   1.0400
 1  2  2   0.0000   0.0000   6.0000   0.0000   0.0000   0.0000   1.0400
 1  2  1   0.0000   3.4110   7.7350   0.0000   0.0000   0.0000   1.0400
 2  2  2   0.0000  27.9213   5.8635   0.0000   0.0000   0.0000   1.0400
 1  1  3  65.1700   8.0170   7.5000   0.0000   0.2028  10.0000   1.0400
 3  1  3  71.7582  26.7070   6.0466   0.0000   0.2000   0.0000   1.8525
 1  1  4  65.4228  43.9870   1.5602   0.0000   0.2000  10.0000   1.8525
 3  1  4  73.7046  23.8131   3.9811   0.0000   0.2000   0.0000   1.8525
 4  1  4  65.6602  40.5852   1.8122   0.0000   0.2000   0.0000   1.8525
 2  1  3  56.4426  17.6020   5.3044   0.0000   0.9699   0.0000   1.1272
 2  1  4  71.0777   9.1462   3.4142   0.0000   0.9110   0.0000   1.0400
 1  2  4   0.0000   0.0019   6.3000   0.0000   0.0000   0.0000   1.0400
 1  3  1  72.1018  38.4720   1.3926   0.0000   0.4785   0.0000   1.2984
 1  3  3  89.9987  44.9806   0.5818   0.0000   0.7472   0.0000   1.2639
 1  3  4  70.3281  12.9371   7.5000   0.0000   0.7472   0.0000   1.2639
 3  3  3  84.2807  24.1938   2.1695 -10.0000   0.7472   0.0000   1.2639
 3  3  4  84.2585  44.1039   0.9185   0.0000   0.7472   0.0000   1.2639
 4  3  4  74.2312  25.7005   4.3943   0.0000   0.7472   0.0000   1.2639
 1  3  2  89.0416  36.9460   0.4569   0.0000   2.7636   0.0000   2.0494
 2  3  3  81.1709   4.2886   6.5904   0.0000   3.0000   0.0000   1.2618
 2  3  4  75.9203  44.9675   0.8889   0.0000   3.0000   0.0000   1.2618
 2  3  2  82.2020  12.7165   3.9296   0.0000   0.2765   0.0000   1.0470
 1  4  1  68.3788  18.3716   1.8893   0.0000   2.4132   0.0000   1.3993
 1  4  3  86.5585  37.6814   1.1611   0.0000   1.7325   0.0000   1.0440
 1  4  4  74.4818  12.0954   7.5000   0.0000   1.7325   0.0000   1.0440
 3  4  3  78.5850  44.3389   1.3239 -26.2246   1.7325  40.0000   1.0440
 3  4  4  77.6245  32.0866   1.8889  -0.9193   1.7325   0.0000   1.0440
 4  4  4  66.4718  15.9087   7.5000   0.0000   1.7325   0.0000   1.0440
 1  4  2  90.0000  33.6636   1.1051   0.0000   0.2638   0.0000   1.1376
 2  4  3  83.8493  44.9000   1.3580   0.0000   0.5355   0.0000   2.5279
 2  4  4  78.7452  24.2010   3.7481   0.0000   0.5355   0.0000   2.5279
 2  4  2  55.8679  14.2331   2.9225   0.0000   0.2000   0.0000   2.9932
 1  2  3   0.0000   0.0019   6.0000   0.0000   0.0000   0.0000   1.0400
 1  2  4   0.0000   0.0019   6.0000   0.0000   0.0000   0.0000   1.0400
```

```
 1  2  5   0.0000   0.0019   6.0000   0.0000   0.0000   0.0000   1.0400
 3  2  3   0.0000   0.0019   6.0000   0.0000   0.0000   0.0000   1.0400
 3  2  4   0.0000   0.0019   6.0000   0.0000   0.0000   0.0000   1.0400
 4  2  4   0.0000   0.0019   6.0000   0.0000   0.0000   0.0000   1.0400
 2  2  3   0.0000   0.0019   6.0000   0.0000   0.0000   0.0000   1.0400
 2  2  4   0.0000   0.0019   6.0000   0.0000   0.0000   0.0000   1.0400
 1  1  5  74.4180  33.4273   1.7018   0.1463   0.5000   0.0000   1.6178
 1  5  1  79.7037  28.2036   1.7073   0.1463   0.5000   0.0000   1.6453
 2  1  5  63.3289  29.4225   2.1326   0.0000   0.5000   0.0000   3.0000
 1  5  2  85.9449  38.3109   1.2492   0.0000   0.5000   0.0000   1.1000
 1  5  5  85.6645  40.0000   2.9274   0.1463   0.5000   0.0000   1.3830
 2  5  2  83.8555   5.1317   0.4377   0.0000   0.5000   0.0000   3.0000
 2  5  5  97.0064  32.1121   2.0242   0.0000   0.5000   0.0000   2.8568
 6  6  6  69.3456  21.7361   1.4283   0.0000  -0.2101   0.0000   1.3241
 2  6  6  75.6168  21.5317   1.0435   0.0000   2.5179   0.0000   1.0400
 2  6  2  78.3939  20.9772   0.8630   0.0000   2.8421   0.0000   1.0400
 3  6  6  70.3016  15.4081   1.3267   0.0000   2.1459   0.0000   1.0400
 2  6  3  73.8232  16.6592   3.7425   0.0000   0.8613   0.0000   1.0400
 3  6  3  90.0344   7.7656   1.7264   0.0000   0.7689   0.0000   1.0400
 6  3  6  22.1715   3.6615   0.3160   0.0000   4.1125   0.0000   1.0400
 2  3  6  83.7634   5.6693   2.7780   0.0000   1.6982   0.0000   1.0400
 3  3  6  73.4663  25.0761   0.9143   0.0000   2.2466   0.0000   1.0400
 2  2  6   0.0000  47.1300   6.0000   0.0000   1.6371   0.0000   1.0400
 6  2  6   0.0000  31.5209   6.0000   0.0000   1.6371   0.0000   1.0400
 3  2  6   0.0000  31.0427   4.5625   0.0000   1.6371   0.0000   1.0400
 2  2  5   0.0000   0.0019   6.0000   0.0000   0.0000   0.0000   1.0400
31    ! Nr of torsions;at1;at2;at3;at4;;V1;V2;V3;V2(BO);vconj;n.u;n
 1  1  1  1   0.0000  48.4194   0.3163  -8.6506  -1.7255   0.0000   0.0000
 1  1  1  2   0.0000  63.3484   0.2210  -8.8401  -1.8081   0.0000   0.0000
 2  1  1  2   0.0000  45.2741   0.4171  -6.9800  -1.2359   0.0000   0.0000
 0  1  2  0   0.0000   0.0000   0.0000   0.0000   0.0000   0.0000   0.0000
 0  2  2  0   0.0000   0.0000   0.0000   0.0000   0.0000   0.0000   0.0000
 0  1  3  0   1.7254  86.0769   0.3440  -4.2330  -2.0000   0.0000   0.0000
 0  2  3  0   0.0000   0.1000   0.0200  -2.5415   0.0000   0.0000   0.0000
 0  3  3  0   1.2314 116.5137   0.5599  -4.1412   0.0000   0.0000   0.0000
 0  1  4  0  -1.3258 149.8644   0.4790  -7.1541  -2.0000   0.0000   0.0000
 0  2  4  0   0.0000   0.1000   0.0200  -2.5415   0.0000   0.0000   0.0000
 0  3  4  0   1.3168  57.0732   0.2679  -4.1516  -2.0000   0.0000   0.0000
 0  4  4  0   2.0000  75.3685  -0.7852  -9.0000  -2.0000   0.0000   0.0000
 0  1  1  0   0.0930  18.6070  -1.3191  -9.0000  -1.0000   0.0000   0.0000
 4  1  4  4  -2.0000  20.6655  -1.5000  -9.0000  -2.0000   0.0000   0.0000
 0  1  5  0   4.0885  78.7058   0.1174  -2.1639   0.0000   0.0000   0.0000
 0  5  5  0  -0.0170 -56.0786   0.6132  -2.2092   0.0000   0.0000   0.0000
 0  2  5  0   0.0000   0.0000   0.0000   0.0000   0.0000   0.0000   0.0000
 0  6  6  0   0.0000   0.0000   0.1200  -2.4426   0.0000   0.0000   0.0000
 0  2  6  0   0.0000   0.0000   0.1200  -2.4847   0.0000   0.0000   0.0000
 0  3  6  0   0.0000   0.0000   0.1200  -2.4703   0.0000   0.0000   0.0000
 1  1  3  3   1.2707  21.6200   1.5000  -9.0000  -2.0000   0.0000   0.0000
 1  3  3  1  -1.8804  79.9255  -1.5000  -4.1940  -2.0000   0.0000   0.0000
 3  1  3  3  -2.0000  22.5092   1.5000  -8.9500  -2.0000   0.0000   0.0000
 1  4  4  3   0.1040  70.1152   0.5284  -3.5026  -2.0000   0.0000   0.0000
 1  1  3  4   1.2181 119.6186  -1.5000  -7.0635  -2.0000   0.0000   0.0000
 2  1  3  4  -2.0000 156.6604   1.1004  -7.3729  -2.0000   0.0000   0.0000
 1  3  4  3   2.0000  96.6281  -1.5000  -3.8076  -2.0000   0.0000   0.0000
 1  1  4  2  -2.0000 147.2445  -1.5000  -7.0142  -2.0000   0.0000   0.0000
 1  1  4  3  -2.0000  47.8326  -1.5000  -9.0000  -2.0000   0.0000   0.0000
 2  3  4  3  -0.2997 152.9040  -1.5000  -4.4564  -2.0000   0.0000   0.0000
 2  4  4  3   0.1040  70.1152   0.5284  -3.5026  -2.0000   0.0000   0.0000
 9    ! Nr of hydrogen bonds;at1;at2;at3;Rhb;Dehb;vhb1
 3  2  3   2.1845  -2.3549   3.0582  19.1627
 3  2  4   1.6658  -3.8907   3.0582  19.1627
 4  2  3   1.8738  -3.5421   3.0582  19.1627
 4  2  4   1.8075  -4.1846   3.0582  19.1627
```

```
3  2  5   2.6644  -3.0000   3.0000   3.0000
4  2  5   4.0476  -3.0000   3.0000   3.0000
5  2  3   2.1126  -4.5790   3.0000   3.0000
5  2  4   2.2066  -5.7038   3.0000   3.0000
5  2  5   1.9461  -4.0000   3.0000   3.0000
```

Appendix B

LAMMPS input files

B.1 LAMMPS input file for constant strain rate molecular dynamics

The following is a representative LAMMPS input script for running a strain to failure simulation using ReaxFF.

```
# Strain rate simulation for PPTA - ReaxFF

# Strain rate
variable        erate equal 1.0e9*1.0e-15

# Units and atom style (must be 'charge')
units           real
atom_style      charge

# Read equilibrated restart file
read_restart    equil.rst

#------ ReaxFF force field setup with reax/c ------------------
pair_style reax/c reaxcontrol.txt lgvdw yes
pair_coeff * * ffield.reax O N C C H H
fix QEQ all qeq/reax 1 0 10 1e-6 reax/c
#-------------------------------------------------------------

# Temperature and pressure settings
variable        Tstart equal 300.0
variable        Tend   equal 300.0
variable        Tdamp  equal 100.0
variable        pdamp  equal 1000.0

# Pressure conversion between atm/MPa
variable        atm2MPa equal 101325/1.0e6
variable        MPa2atm equal 1/v_atm2MPa

# ************************************************************
# ************** STRAIN CONTROLLED DEFORMATION ***************

# Ending strain and strain rate setup
variable        eps    equal 0.15
```

```
variable        lz0    equal 106.64        # Equilibrium simulation cell length
variable        v0     equal v_erate*v_lz0 # Unit cell stretch velocity

fix             STRETCH all deform 1 z vel ${v0} units box
fix             NPT     all npt temp ${Tstart} ${Tend} ${Tdamp} x 0 0 ${pdamp} y 0 0 ${pdamp}

# Timestep setup
variable        dt     equal 0.25
variable        tf     equal round(v_eps/v_erate)
variable        nt     equal round(v_tf/v_dt)
variable        tsim   equal step*v_dt
timestep        ${dt}
reset_timestep  0

# ************************************************************
# ************************************************************



# *************** Set up simulation calculations **************
# ************************************************************

# Set up computes for virial and total stress
compute VIRIAL all pressure thermo_temp virial
compute STRESS all pressure thermo_temp

# Compute bond, angle, dihedral, and improper data
#compute BTYPE  all property/local batom1 batom2 btype
#compute BDIST  all bond/local dist eng

# Save box dimensions at every step
variable        lenx equal "lx"
variable        leny equal "ly"
variable        lenz equal "lz"

# Energy
variable        E     equal etotal
variable        KE    equal ke
variable        PE    equal pe

# Save stresses at every step
variable        sxx equal  -c_STRESS[1]*v_atm2MPa
variable        syy equal  -c_STRESS[2]*v_atm2MPa
variable        szz equal  -c_STRESS[3]*v_atm2MPa
variable        sxy equal  -c_STRESS[4]*v_atm2MPa
variable        sxz equal  -c_STRESS[5]*v_atm2MPa
variable        syz equal  -c_STRESS[6]*v_atm2MPa

# Axial strain
variable        ezz equal lz/${lz0}-1.0

# ************************************************************
# ************************************************************



# ******************** Set up Data output *********************
# ************************************************************

# Setup data output frequency
```

```
variable        neverydata  equal ceil(0.00001/v_erate) # dt = deps/epsdot
variable        neveryBdata equal ceil(0.001/v_erate)   # dt = deps/epsdot

# Thermo output and calculations
thermo_style    custom v_tsim v_ezz temp press etotal pe ke
thermo          ${neverydata}
thermo_modify        flush yes

# Track bond breaking and forming - use REAXC version
fix printbonds all reax/c/bonds ${neveryBdata} reaxbonds.txt

# Axial stress-strain
fix 1 all print ${neverydata} "${tsim} ${ezz} ${szz}" file sigeps.txt screen no

# Keep track of strain-time relation for plotting out bond behavior
fix 2 all print ${neveryBdata} "${tsim} ${ezz}" file straintime.txt screen no

# XYZ file
dump             xyzfile all xyz ${neveryBdata} dump.xyz
dump_modify      xyzfile flush yes element O N C C H H

# Dump for rerun
dump mydump all atom ${neverydata} dump.atom

#********************** Run simulation ************************

restart         ${neverydata} rst1 rst2

run             ${nt} upto

write_restart   sigeps.rst
```